USING VESICLES TO STUDY THE EFFECT OF STEROLS ON THE MECHANICAL STRENGTH OF LIPID MEMBRANES AND THE PROTEIN-LIPID MEMBRANE INTERACTION

by

Philipus Josepus Patty

B.Sc., Institute of Teacher Training and Education of Ujung Pandang Indonesia, 1991.
MSc., Simon Fraser University, 2000.

A THESIS SUBMITTED IN PARTIAL FULFILLMENT
OF THE REQUIREMENTS FOR THE DEGREE OF
DOCTOR OF PHILOSOPHY
in the Department
of
Physics

SIMON FRASER UNIVERSITY
Fall 2006

APPROVAL

Name: Philipus Josepus Patty

Degree: Doctor of Philosophy

Title of thesis: Using Vesicles to Study the Effect of Sterols on the Mechanical Strength of Lipid Membranes and the Protein-Lipid Membrane Interaction

Examining Committee:

Dr. Patricia Mooney, Professor
Chair

Dr. Barbara Frisken, Professor (Senior Supervisor)
Department of Physics

Dr. Michael Wortis, Professor Emeritus
Department of Physics

Dr. Jenifer Thewalt, Associate Professor
Department of Physics
Department of Molecular Biology and Biochemistry

Dr. Martin Zuckermann, Adjunct Professor
Department of Physics
Internal Examiner

Dr. Bela Joos, Professor
Department of Physics, University of Ottawa
Ottawa-Carleton Institute for Physics
External Examiner

Date Approved: August 2, 2006

Abstract

In this thesis, studies of two biophysical topics will be discussed: the effect of sterols on the mechanical strength of lipid membranes, and the interaction between Cytidine 5'-triphosphate(CTP):phosphocholine cytidylyltransferase (CCT) and lipid membranes.

The mechanical strength of lipid membranes was probed by measuring the lysis tension of vesicles, as determined from the minimum pressure required to extrude vesicles through small pores. The vesicles used in these experiments were made from mixtures of 1-palmitoyl-2-oleoyl-sn-glycero-3-phosphatidylcholine (POPC) and various sterols, including cholesterol, lanosterol and ergosterol. The effect of the sterol concentration on the lysis tension was determined. The results show that all sterols increase the lysis tension of POPC membranes, where cholesterol shows the largest effect followed by lanosterol and ergosterol. The increase in the lysis tension of POPC membranes by sterols is correlated to the increase in the chain order of the lipids by sterols. The increase in the strength of lipid membranes by sterols indicates their contribution to cell viability, which depends on maintaining an intact plasma membrane.

The interaction between CCT and lipid membranes was studied by observing vesicle

aggregation induced by CCT. This was conducted by measuring the size and polydispersity of vesicles before and after the introduction of CCT using dynamic light scattering. Vesicles for these studies were made both from lipids that activate CCT (activating lipids) and lipids that do not activate CCT (non-activating lipids). The activating lipids investigated include anionic lipids (class I lipids) and lipids that produce negative curvature in membrane (class II lipids). Aggregation occurs when CCT is introduced to samples of class I lipid vesicles. In contrast, there is no indication of aggregation when CCT is introduced to samples of vesicles made from both non-activating and class II lipids. The occurrence of aggregation depends on the binding strength of CCT to the membrane. The results suggest that CCT cross-bridges two vesicles, which is a new aspect of CCT interaction with lipid membranes.

Keywords : Vesicles, Vesicle Aggregation, Dynamic Light Scattering, Sterols.

To : my wife, Cynthia, and our precious daughter, Willingda

Acknowledgments

I would like to thank Dr. Barbara Frisken for her support and guidance and for giving me opportunities to pursue this degree. I would like to thank Dr. Michael Wortis and Dr. Jenifer Thewalt as my committee members for their input and time. I would like to thank Dr. Martin Zuckermann and Dr. Bela Joos for helpful suggestions for the writing of this thesis. I would also like to thank Dr. Rosemary Cornell and Dr. Svetla Taneva for the collaboration in CCT-membrane interaction studies as well as Dr. Martin Zuckermann, Dr. Ya-Wei Hsueh and Dr. Jenifer Thewalt for the collaboration in the sterol-membrane studies. I am grateful for Dr. Li Yang for helpful discussions in SEM measurements. I really appreciate the help I received from all my friends who share the lab with me : Dr. Art Bailey, Dr. Jun Gao, Dr. Laurent Rubatat, Dave Lee, Yong Sun, Antony Orth, and other friends in the Physics Department for their help and friendship. I would also like to thank my family, the Patty's and the Wattimena's for their support. Finally I am really grateful to my wife, Cynthia and our daughter, Willingda, for their love, support and prayers.

Contents

List of Tables

List of Figures

Chapter 1

Introduction

Every cell is surrounded by a membrane, the plasma membrane, which encapsulates its internal materials and separates them from the external chemical environment. The plasma membrane is made up of lipids, including sterols, and proteins, with a composition that varies between species and between different membranes of the same species. The lipid-protein ratio in the membrane varies from 1:5 to 5:1 [1].

The lipid membrane is relatively permeable to water but impermeable to large molecules and ions. Transport of ions and large molecules from the outside into the cell requires a special channel or transporter system, which is provided by membrane-bound proteins. One of the essential functions of the plasma membrane, therefore, is as a physical barrier that regulates transport of materials into and out of the cell. One of the important properties of the membrane which relates to its function as a physical barrier is the mechanical strength which maintains membrane integrity.

In addition, many cellular enzymes, protein molecules which function as biochemical catalysts, attach or bind to the membrane, and many biological/biochemical processes occur only with the aid of these enzymes. The plasma membrane, hence, also functions as a substrate for enzyme-assisted functional processes in cells.

Two of the four studies described in this thesis relate to the functions of the plasma membrane mentioned above. The first one focuses on the mechanical strength of the membrane, an important factor in cell integrity, which relates to the function of the plasma membrane as a physical barrier. The effect of various sterols on the strength of lipid membranes was studied. The second one focuses on the interaction between a particular enzyme and various lipid membranes, which relates to the function of the membrane as a substrate for enzyme-assisted functional processes. The interaction between Cytidine 5'-triphosphate(CTP):phosphocholine cytidylyltransferase (CCT), a key regulatory enzyme in the synthesis of phosphatidylcholine (PC), and lipid membranes was studied.

Studies show that the lysis tension of vesicles, which is a measure of the mechanical strength of the membranes, is lipid-composition dependent and increases with the presence of cholesterol [2, 3]. Cholesterol is the major sterol in the plasma membranes of mammalian cells [4]. In some prokaryotic membranes, lanosterol is the major sterol, while in plasma membranes of lower eukaryotes, such as certain protozoa, yeast, fungi and insects such as Drosophila, ergosterol is the major sterol [5]. Most knowledge of the effect of sterols on the mechanical strength and other properties of lipid membranes comes from studies using cholesterol. Studies of the mechanical strength of lipid membranes as a function

of lanosterol and ergosterol content, however, are lacking. The experiments described in this thesis were designed to compare the effect of cholesterol, lanosterol and ergosterol on the mechanical strength of lipid membranes. The membrane strength was probed by measuring the lysis tension of vesicles made from mixtures of 1-palmitoyl-2-oleoyl-*sn*-glycero-3-phosphatidylcholine (POPC) and various sterols.

CCT catalyzes the formation of cytidine 5'-diphosphate choline, the head-group donor in the synthesis of PC. This enzyme is amphitropic: it interconverts between a soluble form where it is inactive and a membrane-bound form where it is active. It has a dimeric structure [6], where each monomer is made up of four domains, as shown in Fig. 1.1.a. When the inactive form of CCT senses a decrease in the amount of PC in a membrane, it will bind to the deficient PC membranes and become active [7]. Studies show that CCT binds to and becomes activated by membranes containing anionic lipids [8, 9, 10], dioleylglycerols (DOG) and phosphatidylethanolamines (PE) [11, 12, 13]. These activating lipids can be categorized into two classes. For membranes made up of anionic lipids, the binding of CCT to the membrane occurs by electrostatic interaction between the positively charged binding domain of CCT and the negatively charged surface of the membrane [9, 10, 14]. These lipids are known as class I lipids. For membranes composed of DOG and PE, the binding of CCT is postulated to occur because CCT relieves the negative curvature strain which exists in these membranes [12, 13]. These lipids are known as class II lipids.

The binding of CCT to the membrane of a single vesicle is thought to occur by binding of both binding domains of the CCT dimer as shown in Fig. 1.1.b. However, it is also possible

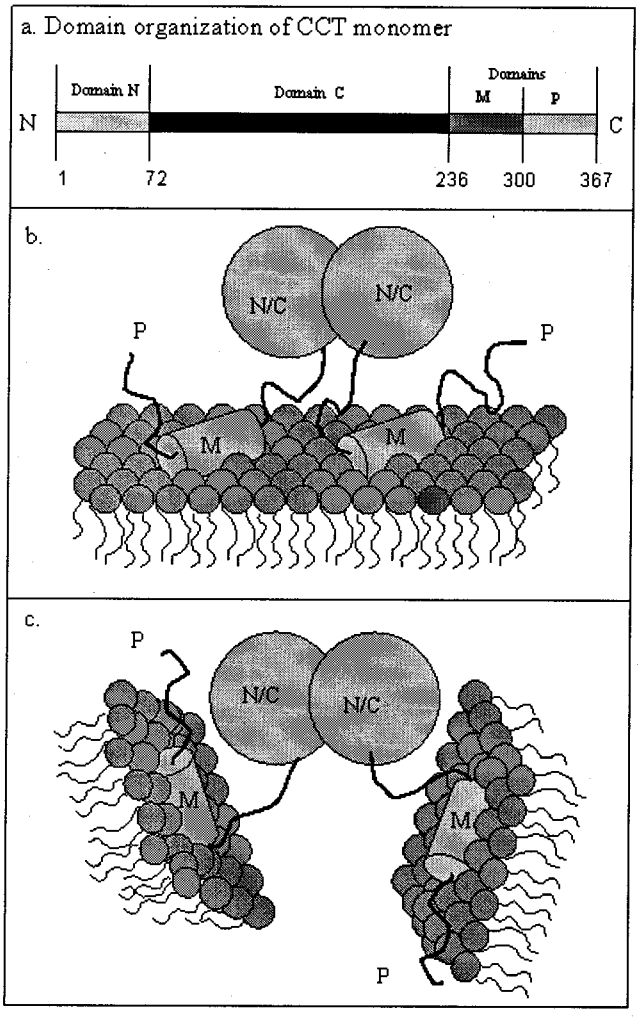

Figure 1.1: a. Domain organization of CCT monomer, b. Domain M of each monomer binds to the membrane of a single vesicle, c. CCT cross-bridges two vesicles through binding of domain M of each monomer to the membrane of two different vesicles.

for each binding domain to bind to the surface of different vesicles, cross-bridging the two vesicles as shown in Fig. 1.1.c. The cross-bridging mode will result in the aggregation of vesicles. It has been observed that addition of CCT to small unilamellar anionic vesicles increases the turbidity of the samples, suggesting the occurrence of aggregation [15]. In this thesis, I will describe experiments designed to study the interaction between CCT and lipid membranes by observing vesicle aggregation induced by CCT. Vesicles for these studies were made both from lipids that activate CCT and lipids that do not activate CCT.

Both studies mentioned above use extruded vesicles as a cell model. In extrusion, large multilamellar vesicles formed when the lipid is dispersed in an aqueous medium are pushed repeatedly through the pores in polycarbonate track-etched (PCTE) membranes [16]. In this thesis, I also discuss the properties of the extruded vesicles, including the size distribution and the number of lamellae (lamellarity), as affected by the size distribution of the pores.

I used dynamic light scattering (DLS) to characterize the size and vesicle aggregation in the studies described above. In this thesis, I explain different data analyzes used to characterize the size distributions of the vesicles in details.

This thesis consists of six chapters, where the four main chapters discuss four different experiments. In Chapter 2, I describe in detail different methods of DLS data analyzes and compare the results for different methods. In Chapter 3, I discuss the effect of the size distribution of the pores in PCTE membranes on the size distribution of vesicles produced by extrusion. I also discuss the effect of the pore size on the lamellarity of the vesicles. In Chapter 4, experiments investigating the effect of sterols, including cholesterol, lanosterol

and ergosterol on the mechanical strength of lipid membranes are discussed. In Chapter 5, I describe the interaction between CCT and lipid membranes, which is studied by observing vesicle aggregation induced by CCT. Chapter 6 contains general conclusions and suggestions for future experiments.

Chapter 2

Using Dynamic Light Scattering to Determine Particle Size Distributions

2.1 Introduction

In dynamic light scattering (DLS), the time dependence of scattered light intensity is analyzed in terms of intensity-intensity autocorrelation function $< I(t)I(t+\tau) >$, the time average of the product of $I(t)$, intensity at time t, with $I(t+\tau)$, intensity at time $t+\tau$, where τ is delay time [17]. Under certain conditions, the intensity-intensity autocorrelation function can be related to the field-field autocorrelation function [18], $\langle E(t)E^*(t+\tau)\rangle$, where $E(t)$ and $E(t+\tau)$ are the electric field of light scattered by a sample at time t and

$t + \tau$, respectively.

If the particles are monodisperse, the field-field autocorrelation function decays exponentially in time with a decay rate proportional to the diffusion coefficient. The diffusion coefficient of the particles can be calculated from the decay rate and the particle radius can be determined from the diffusion coefficient.

If the particles are polydisperse, the field-field autocorrelation function decays exponentially in time with a distribution of decay rates, instead of a single decay rate. The main goal in analyzing the light scattered from polydisperse particles is to determine the particle size distribution or the number of particles of a given size in the dispersion.

There are two factors which are related to the intensity of light scattered by particles of different sizes which complicate the determination of the particle size distributions. First, scattered intensity is proportional to the mass square of the particles as shown in the next section. Therefore, for polydisperse particles, large particles scatter more light than small particles at a particular scattering angle. Second, if the size of the particles is large, in practice, larger than $\lambda/20$, but still smaller than λ [19], there is an effect of destructive interference which is proportional to the scattering angle. This effect is contained in a form factor, which is dependent on the scattering angle, size and shape of the particles. Consequently, for the polydisperse samples, large particles scatter more light at the small scattering angles and small particles scatter more light at the large scattering angles. This effect causes an apparent dependence of the size distribution of the particles on scattering angle, if proper care is not taken in the analysis of scattering data. Because of these effects,

care is needed to properly extract the number-weighted size distribution of the particles.

There are only a few groups that directly determine number-weighted distributions of particles using DLS. A number-weighted distribution of arbitrary functionality can be obtained using discrete Laplace inversion algorithms [20]. Alternatively, number-weighted distributions have been determined by multiangle DLS measurements [21]. This requires long measurement times, especially when large particles and small angles are involved.

The DLS data is usually analyzed using cumulants or a moment-based analysis [22, 23]. In these methods, the intensity-intensity autocorrelation function data is described in terms the distribution of decay rates and the analysis provides information about the cumulants and the moments of this distribution. The decay rate distribution is an intensity-weighted distribution. Results from cumulants analysis have been converted to number distributions that have the form of a log-normal distribution [24, 25], a Gaussian or normal distribution [26], a Schulz distribution [24, 27, 28] or even an arbitrary distribution function [29]. These methods are based on the assumption that particles are sufficiently small so that the effect of destructive interference is insignificant. In fact, this assumption is not valid in many measurements involving extruded vesicles with typical size larger than 50 nm radius. The data also can be described using a radius distribution instead of decay-rate distribution and the intensity-weighted radius distribution can be extracted. Results from an intensity-weighted radius distribution have been converted to number-weighted radius distributions that have the form of Gaussian and log-normal distribution [30].

In this chapter, I discuss determination of the average vesicle size from a number-weighted distribution of extruded vesicles as a prototypical example of polydisperse spherical particles. This is done by fitting an expression for the intensity-intensity autocorrelation function to the data, where the square of the particle mass M^2 and the form factor of the vesicles are included in the analysis. A non-linear least squares (nllsq) fitting routine is used for the fitting analysis. The results are compared to the analysis from the intensity-weighted distribution, where the particle mass M^2 and the form factor of the vesicles are not included in the analysis. I also show the comparison between the results for the average size from the number-weighted distribution determined from direct fitting to the data and from converting from the intensity-weighted distribution.

2.2 Dynamic Light Scattering

2.2.1 Light Scattering Theory

In light scattering experiments, a monochromatic polarized beam of laser light is incident on a sample, for example, a transparent liquid dispersion of vesicles, and is scattered into a detector placed at an angle θ with respect to the incident beam. Figure. 2.1 shows a schematic diagram of light scattering experiments. Directions of propagation of the incident and the scattered light are characterized by the wavevectors $\overrightarrow{k_i}$ and $\overrightarrow{k_f}$, respectively. The plane formed by these two vectors is defined as the plane of observation. The direction of polarization for incident and scattered fields is characterized by $\hat{n}_i$ and $\hat{n}_f$, respectively, and is perpendicular to the plane of observation. The scattering volume, the sample volume

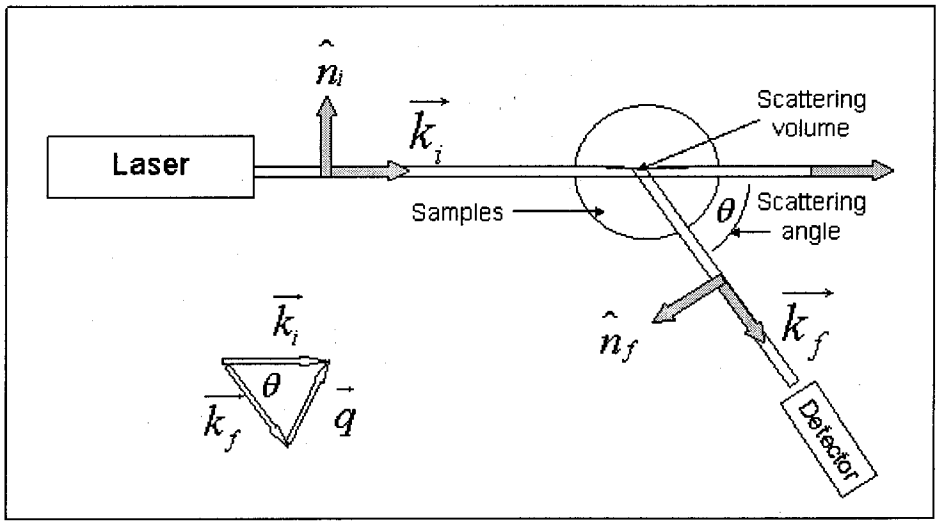

Figure 2.1: Schematic diagram of the light scattering experiments. a monochromatic plane polarized beam of laser light is directed to the samples and is scattered into the detector. Scattering volume, the effective volume that scatters the light, is defined by the overlap of the scattered beam and incident beam. Directions of propagation of incident and scattered light is characterized by the wavevectors $\vec{k_i}$ and $\vec{k_f}$, respectively. Scattering angle is defined as the angle between $\vec{k_i}$ and $\vec{k_f}$. Direction of polarization for incident and scattered fields is characterized by $\hat{n}_i$ and $\hat{n}_f$, respectively and is perpendicular to the plane of the diagram. The scattering wavevector $\vec{q}$ is defined as the difference between incident and scattered light wavevectors, $\vec{q} = \vec{k_i} - \vec{k_f}$.

from which light is scattered, is defined by the overlap of the scattered beam and the incident beam. The change in the wavelength after interaction of light with matter is very small. Based on this fact, the magnitude of the incident wavevector $k_i = \frac{2\pi n}{\lambda_i}$ is assumed to be equal to the magnitude of the scattered wavevector $k_f = \frac{2\pi n}{\lambda_f}$. The magnitude of the scattering wavevector q, which is defined as the difference between incident and scattered light wavevectors, $\overrightarrow{q} = \overrightarrow{k_i} - \overrightarrow{k_f}$, can then be calculated as,

$$q = \frac{4\pi n}{\lambda} \sin\frac{\theta}{2} \quad , \tag{2.1}$$

where n is index refraction of the medium.

Since the strength of the electric field interaction with matter is much greater than that of the magnetic field interaction, only the electric field is considered. The incident electric field can be written as,

$$\overrightarrow{E}_i(\overrightarrow{r}, t) = \hat{n}_i E_o \exp i(\overrightarrow{k_i} \cdot \overrightarrow{r} - \omega_i t) \quad , \tag{2.2}$$

where, $\hat{n}_i$, ω_i and E_o are the unit vector indicating the direction of the polarization, the angular frequency, and the amplitude of the field, respectively, while $\overrightarrow{k_i}$ is the incident wavevector. The electric field exerts a force on the charges of atoms in the scattering volume which induces electric dipoles. These dipoles oscillate with the frequency of the incident light and, consequently, radiate light in all directions. The induced dipole can be written as

$$\overrightarrow{P}(r, t) = \underline{\alpha}(r, t)\overrightarrow{E}_i(r, t) \quad , \tag{2.3}$$

where $\underline{\alpha}(r, t)$ is the polarizability tensor. For isotropic scatterers, the direction of $\overrightarrow{P}$ and $\overrightarrow{E}_i$ are the same but, in general, the direction of $\overrightarrow{P}$ and $\overrightarrow{E}_i$ are not necessarily the same.

For the case that the scattering is elastic and the light scattered from the particles goes to the detector directly (single scattering), the scattered electric field $\overrightarrow{E}_s(\overrightarrow{\Re}, t)$ measured at a distance $\Re$ from the scatterers can be written as [17],

$$\overrightarrow{E}_s(\overrightarrow{\Re}, t) = \frac{E_0}{4\pi\epsilon_o \Re} \exp(i(k_f \Re) \int_v d^3r \exp[i(\overrightarrow{q} \cdot \overrightarrow{r} - \omega_i t)][\hat{n}_f \cdot [\overrightarrow{k_f} \times (\overrightarrow{k_f} \times (\underline{\delta\epsilon}(\overrightarrow{r}, t) \cdot \hat{n}_f))]], \quad (2.4)$$

where $\hat{n}_f$ is the unit vector indicating the direction of polarization, the subscript v indicates that the integral is over the scattering volume, and $\underline{\delta\epsilon}(\overrightarrow{r}, t)$ is the dielectric constant fluctuation tensor at position $\overrightarrow{r}$ and time t. The dielectric constant of a medium fluctuates in space and in time and can be written as,

$$\epsilon(\overrightarrow{r}, t) = \epsilon_o \underline{I} + \underline{\delta\epsilon}(\overrightarrow{r}, t) \quad , \quad (2.5)$$

where ϵ_o is the average dielectric constant of the medium, $\underline{I}$ is the second-rank unit tensor and $\underline{\delta\epsilon}(\overrightarrow{r}, t)$ is the dielectric constant fluctuation tensor at position $\overrightarrow{r}$ and time t.

Detectors in light scattering experiments measure scattered light intensity. Intensity I is related to electric field E through

$$I = c\epsilon_0 |E|^2 \quad , \quad (2.6)$$

where c and ϵ_0 are the speed of light in vacuo and the permittivity constant, respectively. For small particles, much smaller than the wavelength of light, in a medium with index of refraction n, the ratio of the scattered intensity I_s to the incident intensity I_i can be written as [31],

$$\frac{I_s}{I_i} = \left(\frac{2\pi n}{\lambda}\right)^4 \frac{\sin^2 \phi}{\Re^2} \alpha_0^2, \quad (2.7)$$

where ϕ is the angle between the polarization of the incident field $\widehat{n}_i$ and the propagation direction of the scattered field $\overrightarrow{k_f}$, $\Re$ is the distance between scattering particles and the detector and α_0 is the mean polarizability of the particles.

For large particles comparable in size to λ, light scattered from various subregions inside the particle interferes destructively to some extent. The effect of destructive interference increases when the scattering angle increases and depends on the size and shape of the particles. It is contained in the form factor $P(q)$ defined as,

$$P(q) = \frac{\textit{scattered intensity at angle } \theta}{\textit{scattered intensity at angle } \theta = 0^\circ} \quad . \tag{2.8}$$

Equation 2.8 is valid when particles are non-interacting, which is the case in the limit where density of particles is low. The general equation for the form factor can be written as,

$$P(q) = \left\langle \left| \frac{1}{l} \sum_{i=1}^{l} e^{iq \cdot r_i} \right|^2 \right\rangle \quad , \tag{2.9}$$

where, l is the number of scattering segments in the particle, r_i is the position of the ith segment and the closed brackets denote the average over all orientations. Considering the effect of interference of scattered field from large particles, Eq. 2.7 can be written as,

$$\frac{I_s}{I_i} = \left(\frac{2\pi n}{\lambda}\right)^4 \frac{\sin^2 \phi}{\Re^2} \alpha_0^2 P(q) \quad , \tag{2.10}$$

where $P(q)$ is the form factor of the particles.

The form factor for a vesicle can be calculated by applying Eq. 2.9 to a hollow sphere with a finite thickness as,

$$P(q) = \left[\frac{3}{q^3 \left(R_o^3 - R_i^3\right)} \left(\sin qR_o - qR_o \cos qR_o - \sin qR_i + qR_i \cos qR_i\right) \right]^2 \quad , \tag{2.11}$$

where R_o, R_i and t are vesicle inner radius, vesicle outer radius and thickness of the bilayer, respectively. When the thickness of the bilayer is much smaller than the wavelength of light, and $R_o, R_i >> t$, Eq. 2.11 reduces to [32],

$$P(q) = \left[\frac{\sin qR}{qR}\right]^2 \quad . \tag{2.12}$$

These expressions for the vesicle form factor are valid when the system satisfies the Rayleigh-Debye condition,

$$\frac{4\pi R_o}{\lambda}\left(\frac{n_p}{n} - 1\right) << 1 \quad , \tag{2.13}$$

where n and n_p are the index of refraction of solvent and vesicles, respectively.

For particles dispersed in a medium, the mean polarizability α_0 is related to index of refraction of particles n_p by,

$$4\pi N_v \alpha_0 = \frac{3(n_p^2 - n^2)}{n_p^2 + 2n^2} \quad , \tag{2.14}$$

where N_v is the number of particles per cubic centimeter [33]. For a dilute solution, the refractive index of particles n_p is close to refractive index of the surrounding medium n and Eq. 2.14 can be written as,

$$4\pi N_v \alpha_0 \approx n_p^2 - n^2 \quad . \tag{2.15}$$

The index of refraction of the particles n_p can be expanded in a Taylor series in terms of mass concentration c of the particles in the dispersion,

$$n_p = n + \left.\frac{dn_p}{dc}\right|_{c=0} c \quad , \tag{2.16}$$

and

$$n_p^2 = n^2 + 2n\left.\frac{dn_p}{dc}\right|_{c=0} c \quad , \tag{2.17}$$

where only first two terms are considered. Combining Eqs. 2.14 and 2.17, the mean polarizability α_0 can be written as,

$$\alpha_0 = \frac{nc(dn_p/dc)\mid_{c=0}}{2\pi N_v} = \frac{nM(dn_p/dc)\mid_{c=0}}{2\pi N_a} \quad , \tag{2.18}$$

where M, N_v, and N_a are the molecular mass of the particles, their number per cubic centimeter, and Avogadro number, respectively. The ratio of scattered to incident intensity of Eq. 2.10 can then be written in terms of the mass of particle M as,

$$\frac{I_s}{I_0} = \frac{4\pi^2 n^2 M^2 (dn_p/dc)^2}{N_a^2 \lambda^4 \Re^2} P(q) \quad . \tag{2.19}$$

Equation 2.19 shows that the scattered intensity is proportional to the square of the mass of the particle and is weighted by the form factor of the particle.

2.2.2 Dynamic Light Scattering Technique and Particle Size Determination

When laser light impinges on a sample such as a vesicle dispersion, the scattered intensity fluctuates with time due to the Brownian motion of the particles. In DLS, the time dependence of scattered light intensity is analyzed in terms of intensity-intensity autocorrelation function $< I(t)I(t+\tau) >$, the time average of the product of $I(t)$, intensity at time t, with $I(t+\tau)$, intensity at time $t+\tau$, where τ is delay time [17]. This function can be written in terms of the scattered electric field as [18, 31],

$$\begin{aligned} \langle I(t)I(t+\tau)\rangle &= \left\langle |E(t)|^2 |E(t+\tau)|^2 \right\rangle = \left\langle |E(t)|^2 \right\rangle \left\langle |E(t+\tau)|^2 \right\rangle + \\ &\quad \langle E(t)E^*(t+\tau)\rangle \langle E^*(t)E(t+\tau)\rangle \quad , \end{aligned} \tag{2.20}$$

where $E(t)$ and $E(t+\tau)$ are the scattered field at time t and $t+\tau$, respectively. Using the relations,

$$\left\langle |E(t)|^2 \right\rangle = \left\langle |E(t+\tau)|^2 \right\rangle \quad , \tag{2.21}$$

and

$$\langle E(t)E^*(t+\tau)\rangle = \langle E^*(t)E(t+\tau)\rangle \quad , \tag{2.22}$$

Eq. 2.20 becomes

$$\langle I(t)I(t+\tau)\rangle = \left\langle |E(t)|^2 \right\rangle^2 + \langle E(t)E^*(t+\tau)\rangle^2 \quad . \tag{2.23}$$

The normalized intensity-intensity autocorrelation function $g^{(2)}(\tau)$ is defined as,

$$g^{(2)}(\tau) = \frac{\langle I(t)I(t+\tau)\rangle}{\langle I(t)I(t)\rangle} \quad . \tag{2.24}$$

Using Eq. 2.23, $g^{(2)}(\tau)$ can be written in terms of the normalized field-field autocorrelation function $g^{(1)}(\tau)$ as,

$$g^{(2)}(\tau) = 1 + \beta[g^{(1)}(\tau)]^2 \quad , \tag{2.25}$$

where

$$g^{(1)}(\tau) = \frac{\langle E(t)E^*(t+\tau)\rangle}{\langle E(t)E^*(t)\rangle} \quad , \tag{2.26}$$

and β is a factor which depends on the experimental geometry. Equation 2.25 is known as the Siegert relation and it holds when the scattered field is Gaussian random variable, i.e., the scattered field varies about the mean field in a Gaussian distribution.

For monodisperse particles undergoing Brownian motion, the field-field autocorrelation function decays exponentially in time [18],

$$g^{(1)}(\tau) = \exp[-\Gamma\tau] \quad , \tag{2.27}$$

where the decay rate $\Gamma = Dq^2$ depends on the diffusion coefficient of the particles D and the magnitude of the scattering wavevector q defined in Eq. 2.1. The radius R can then be determined using the Stokes-Einstein relation:

$$R = \frac{k_B T}{6\pi\eta D} = \frac{k_B T q^2}{6\pi\eta\Gamma} \quad , \tag{2.28}$$

where η and T are the viscosity and temperature of the solvent and k_B is the Boltzmann's constant. The size of the particles determined in this case is called the hydrodynamic radius, which is defined as the radius of a hard sphere with the same diffusion coefficient as the diffusion coefficient of the particle.

For polydisperse particles, there will be a distribution of decay rates instead of a single decay rate. In this case, $g^{(1)}(\tau)$ is given by

$$g^{(1)}(\tau) = \int_0^\infty G(\Gamma)\exp[-\Gamma\tau]d\Gamma \quad , \tag{2.29}$$

where $G(\Gamma)$ describes the distribution of decay rates and,

$$\int_0^\infty G(\Gamma)d\Gamma = 1 \quad ., \tag{2.30}$$

since $g^{(1)}(\tau) = 0$. $G(\Gamma)$, which is q-dependent is characterized by a mean decay rate,

$$\overline{\Gamma} = \int_0^\infty \Gamma\, G(\Gamma)d\Gamma \quad , \tag{2.31}$$

and a relative variance,

$$\sigma_\Gamma^2 = \frac{{s_\Gamma}^2}{\overline{\Gamma}^2} = \int_0^\infty \frac{\left(\Gamma - \overline{\Gamma}\right)^2}{\overline{\Gamma}^2}\, G(\Gamma)d\Gamma \quad . \tag{2.32}$$

Both $\overline{\Gamma}$ and σ_Γ are q-dependent. Determining the precise functional form of $G(\Gamma)$ is problematic, since the correlation function is measured discretely only over an incomplete range

of τ. However, If a functional form for $G(\Gamma)$ is assumed, for example, a Gaussian distribution, the mean decay rate $\overline{\Gamma}$ and associated polydispersity σ_Γ can be determined by fitting Eq. 2.25 to the intensity-intensity autocorrelation function data using Eq. 2.29 for the field-field autocorrelation function.

Alternatively, in a moment-based analysis, the field-field autocorrelation function may be expressed in terms of the moments of the decay rate distribution about the mean decay rate [23]. The moments about the mean are defined as

$$\mu_m = \int_0^\infty G(\Gamma)(\Gamma - \overline{\Gamma})^m d\Gamma, \tag{2.33}$$

where $m = 1$ describes the mean decay rate of the distribution and $m = 2$, the second moment and $m = 3$, the third moment, correspond to the variance and the skewness of the distributions, respectively. In this method, $\exp[-\Gamma\tau]$ is expanded about the mean decay rate $\overline{\Gamma}$ as,

$$\exp[-\Gamma\tau] = \exp[-\overline{\Gamma}\tau]\exp[-(\Gamma - \overline{\Gamma})\tau]. \tag{2.34}$$

The second exponential in Eq. 2.34 can be expressed as a series expansion

$$\exp[-(\Gamma - \overline{\Gamma})\tau] = \left(1 - (\Gamma - \overline{\Gamma})\tau + \frac{(\Gamma - \overline{\Gamma}\tau)^2\tau^2}{2!} - \frac{(\Gamma - \overline{\Gamma}\tau)^3\tau^3}{3!} + ...\right). \tag{2.35}$$

Using Eqs. 2.34 and 2.35, the field-field autocorelation function of Eq. 2.29 can be written as,

$$g^{(1)}(\tau) = \exp[-\overline{\Gamma}\tau]\int_0^\infty G(\Gamma)\left[1 - (\Gamma - \overline{\Gamma})\tau + \frac{(\Gamma - \overline{\Gamma})^2\tau^2}{2!} - \frac{(\Gamma - \overline{\Gamma})^3\tau^3}{3!} + ...\right]d\Gamma \quad , \tag{2.36}$$

which reduces by means of Eq. 2.33 to,

$$g^{(1)}(\tau) = \exp[-\overline{\Gamma}\tau]\left(1 + \frac{\mu_2}{2!}\tau^2 - \frac{\mu_3}{3!}\tau^3 + ...\right), \tag{2.37}$$

where the relative variance $\sigma_\Gamma^2 = \frac{\mu_2}{\overline{\Gamma}^2}$. The mean decay rate $\overline{\Gamma}$ and associated polydispersity σ_Γ can be determined directly by fitting Eq. 2.25 (up to second order) to the intensity-intensity autocorrelation function data using Eq. 2.37 for the field-field autocorrelation function.

Once the decay rate distribution $G(\Gamma)$ has been determined, e.g., by one of the above fitting methods, an effective mean particle size can be determined by the Stokes-Einstein relation of Eq. 2.28,

$$\overline{R_h} = \frac{k_B T q^2}{6\pi\eta\overline{\Gamma}} \quad , \tag{2.38}$$

and the relative variance can be calculated from,

$$\sigma_{R_h}^2 = \frac{(\Gamma - \overline{\Gamma})^2}{\overline{\Gamma}^2} \quad . \tag{2.39}$$

Both $\overline{R_h}$ and σ_{R_h} are q-dependent.

Instead of working with the decay rate distribution $G(\Gamma)$, the analysis can be reformulated in terms of a radius distribution. For example, Eq. 2.29 can be written in terms of an intensity-weighted radius distribution $G_i(R)$ using Eq. 2.28 as,

$$g^{(1)}(\tau) = \int_0^\infty G_i(R) \exp\left[\frac{-k_B T q^2}{6\pi\eta R}\tau\right] dR \quad , \tag{2.40}$$

where,

$$\int_0^\infty G_i(R)\, dR = 1 \quad , \tag{2.41}$$

since $g^{(1)}(0) = 1$, so that

$$\int_0^\infty G(\Gamma) d\Gamma = \int_0^\infty G_i(R)\, dR. \tag{2.42}$$

If a functional form for $G_i(R)$ is assumed, the intensity-weighted radius distribution can be determined by fitting Eq. 2.25 to the intensity-intensity autocorrelation function data

using Eq. 2.40 for the field-field autocorrelation function. The mean radius $\overline{R_i}$ and the associated polydispersity σ_{R_i} of the intensity-weighted radius distributions defined as,

$$\overline{R_i} = \int_0^\infty R\, G_i(R)\, dR \quad , \tag{2.43}$$

and,

$$\sigma_{R_i}^2 = \int_0^\infty \frac{(R-\overline{R_i})^2}{\overline{R_i}^2} G_i(R)\, dR \quad , \tag{2.44}$$

respectively, can then be determined. Both $\overline{R_i}$ and σ_{R_i} are q-dependent.

To overcome this q-dependence of the mean radius, $g^{(1)}(\tau)$ of Eq. 2.40 must be modified. The field-field autocorrelation function can be written in terms of the dynamic form factor $P(q,\tau)$ as,

$$\langle E(t)E^*(t+\tau)\rangle = \hat{n}_i \cdot \hat{n}_f\ \alpha_0^2\ N\ P(q,\tau) \quad , \tag{2.45}$$

where $\hat{n}_i$ and $\hat{n}_f$ are the directions of the polarization of incident and scattered field, respectively, N is the number of particles, α_0 is the mean polarizability which is proportional to the mass of the particle M, and $P(q,t) = \exp(-Dq^2\tau)P(q)$ [17]. Then, polydisperse particles described by a particular shape of distribution $G_n(R)$,

$$\langle E(t)E^*(t+\tau)\rangle \propto \int_0^\infty M^2\ P(q)\ \exp(-Dq^2\tau)\ G_n(R)\, dR \quad . \tag{2.46}$$

Using Eq. 2.46, the normalized field-field autocorrelation function can be written as,

$$g^{(1)}(\tau) = \frac{\int_0^\infty G_n(R)\ M^2\ P(q) \exp\left[\frac{-k_B T q^2}{6\pi\eta R}\tau\right]\ dR}{\int_0^\infty G_n(R)\ R^4\ P(q)\ dR} \quad , \tag{2.47}$$

where $G_n(R)$, the number distribution, represents the actual size distribution of the particles and is q-independent. For these studies, extruded vesicles were chosen as prototypical

polydisperse particles. Since particle mass is proportional to its volume and for vesicles volume is proportional to R^2, the M^2 of the vesicle is proportional to R^4.

Finding the precise functional form of $G_n(R)$ using information of $g^{(1)}(\tau)$ from the measurements is a complicated task. However, if a functional form for $G_n(R)$ is assumed, the distribution can be determined by fitting Eq. 2.25 to the intensity-intensity autocorrelation function data using Eq. 2.47 for the field-field autocorrelation function. The mean radius $\overline{R_n}$ and the associated polydispersity σ_{R_n} of the number-weighted radius distributions defined as

$$\overline{R_n} = \int_0^\infty R\, G_n(R)\, dR \quad , \tag{2.48}$$

and,

$$\sigma_{R_n}^2 = \int_0^\infty \frac{(R-\overline{R_n})^2}{\overline{R_n}^2} G_n(R)\, dR \quad , \tag{2.49}$$

respectively, can then be determined. Both $\overline{R_n}$ and σ_{R_n} are q-independent.

2.2.3 Relation between $G_i(R)$ and $G_n(R)$

The number-weighted distribution $G_n(R)$ can be written in terms of intensity-weighted distribution $G_i(R)$ as [20]:

$$G_n(R) = A\frac{G_i(R)}{R^4 F(R)} \quad , \tag{2.50}$$

where

$$A = \left[\int_0^\infty \frac{G_i(R)}{R^4 F(R)}\, dR\right]^{-1} \tag{2.51}$$

has been introduced to ensure that $G_n(R)$ is normalized. Thus, for example, if $G_i(R)$ is known, the mean radius $\overline{R_n}$ and polydispersity σ_{R_n} of the number-weighted distribution can

then be calculated from the intensity-weighted distributions using Eq. 2.50.

2.2.4 Model Distributions

The actual shape of the size distributions of vesicles is not known and it is complicated to determine them directly from DLS data. Alternatively, one can assume that the size distributions of vesicles can be described by a particular type of distribution. The distribution commonly used to represent the size distribution of vesicles is the Schulz distribution [20, 34]. It is asymmetric and skews to the large size of the distribution. This is appropriate for vesicles, as there is a lower limit at which vesicles can be formed and the possible aggregation between vesicles results in larger structures. The Schulz distribution is written as

$$G_S(R) = \left(\frac{m+1}{\overline{R}}\right)^{m+1} \frac{R^m}{m!} \exp\left[\frac{-R(m+1)}{\overline{R_S}}\right] , \tag{2.52}$$

where $m \geq 1$ is an integer and is related to the relative variance σ^2 by $\sigma^2 = 1/(m+1)$. The Schulz distribution is characterized by two parameters: a mean radius $\overline{R_S}$ and m which relates to relative variance.

For comparison, the Gaussian distribution is also used in this analysis. The Gaussian distribution, on the other hand, is written as

$$G_G(R) = \left(\frac{1}{\sqrt{2\pi}s}\right) \exp\left[\frac{-(\overline{R_G} - R)^2}{2s^2}\right] , \tag{2.53}$$

where $\overline{R_G}$ and s are the mean radius and standard deviation, respectively. The Gaussian distribution is characterized by two parameters: a mean radius $\overline{R_G}$ and a standard deviation s.

Figures 2.2.4.a, b and c show Gaussian and Schulz probability distribution function for particles with a mean radius of 60 nm and polydispersities of 0.14, 0.33 and 0.45, respectively. These distributions coincide when the polydispersity is small but deviate from each other when polydispersity is large.

2.3 Materials and Methods

2.3.1 Materials

The lipid used to prepare vesicles was 1-stearoyl-2-oleoyl-*sn*-glycero-3-phosphatidylcholine (SOPC). It was purchased from Avanti Polar Lipids Inc. (Alabaster, AL). Polycarbonate track-etched (PCTE) membranes used in extrusion were purchased from Osmonics Inc. (Livermore, CA).

2.3.2 Extruded Vesicle Preparation

The vesicles were prepared by hydrating SOPC in purified water from a Milli-Q plus water purification system (Millipore, Bedford MA). The use of purified water ensures the production of spherical vesicles [35] and negligible contaminant in the samples. The hydrated sample was taken through a freeze-thaw-vortex (FTV) process and extruded through two PCTE membranes with nominal pore radius of 200 nm (pre-extrusion). The pre-extruded samples were then extruded through PCTE membranes with nominal pore radii of 50 and 100 nm at least 10 times. Vesicles produced using PCTE membranes with nominal pore radii of 50 and 100 nm will be described as 50 nm and 100 nm vesicles, respectively, in the

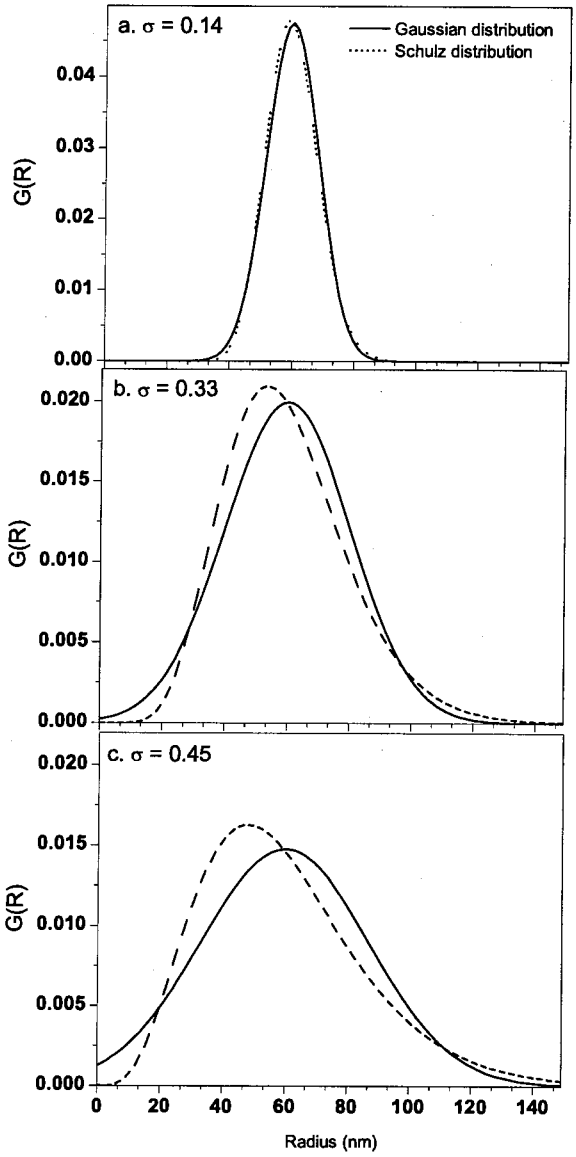

Figure 2.2: Gaussian and Schulz probability distribution function for a mean radius of 60 nm and polydispersities of a. 0.14, b. 0.33, and c. 0.45.

rest of this chapter.

2.3.3 DLS Measurements

The apparatus used for light scattering measurements was an ALV DLS/SLS-5000 spectrometer/gonio-meter manufactured by ALV-Laser GmbH of Langen, Germany. A schematic diagram of the apparatus is shown in Fig. 2.3. It consists of a 23 mW HeNe laser of wavelength 632.8 nm, beam steering optics, attenuator, temperature-controlled scattering chamber, detection optics and photodiodes. Two mirrors are used to steer the incident beam through the sample and two lenses are used: one to focus the beam onto the the center of the scattering cell, and the other to image the sample volume onto the photomultiplier tube. The half-wave plate between the mirrors is used to rotate the polarization of the laser beam from horizontal to vertical. The beamsplitter directs a part of the beam to a photodiode that reads the incident beam intensity; the other photodiode reads transmitted beam intensity. The attenuator is used to adjust the light intensity. The glass ampoule containing the sample is placed in the scattering chamber consisting of a quartz vat filled with toluene. Toluene was chosen because it has a refractive index close to that of the ampoule as well as to that of the quartz vat. Two pinholes are used to adjust the range of scattering angle detected and the size of the phototube's viewable beam. Light scattered from the sample is detected by a photomultiplier tube mounted on a computer-controlled motorized goniometer that makes measurements possible at a variety of scattering angles. The scattering intensity is recorded by a correlator. This apparatus uses an ALV-5000/E Multiple Tau digital Correlator which is a real-time computation correlator of photon correlation functions with a fixed range of

simultaneous lag times between 200 ns and several hours. All parts of the apparatus were mounted on a Melles-Griot optical table to avoid external vibration.

Prior to the size measurement, a 10-ml ampoule containing a sample of lipid vesicle suspension in Milli-Q water was placed in the scattering chamber. Measurements were performed on samples consisting of a ratio of 0.1 mg lipid to 1 ml water; this was good enough to stay in the single scattering regime due to the low number density of the vesicles. In a multiple scattering regime, where the light has been scattered more than once in the sample, distortion of the time dependence of the measured correlation function can occur [18]. Five measurements were taken for each sample at scattering angles ranging from 20° to 150°.

2.3.4 Data Analysis

Data taken at the DLS measurements is the intensity-intensity autocorrelation $g^{(2)}(\tau)$. The decay rate distribution $G(\Gamma)$, the intensity-weighted distribution $G_i(R)$ and the number-weighted distribution $G_n(R)$ are determined by fitting an expression for $g^{(2)}(\tau)$,

$$g^{(2)}(\tau) = B + \beta[g^{(1)}(\tau)]^2 \quad , \tag{2.54}$$

to the data, where different expressions for $g^{(1)}(\tau)$ are used. The decay rate distribution $G(\Gamma)$ is determined by using both Eqs. 2.29 and 2.33 for $g^{(1)}(\tau)$ and the mean radius $\overline{R_h}$ and associated polydispersity σ_{R_h} are calculated from $G(\Gamma)$. The intensity-weighted distribution $G_i(R)$ is determined by using Eq. 2.40 for $g^{(1)}(\tau)$ and the number-weighted distribution $G_n(R)$ is determined by using Eq. 2.47 for $g^{(1)}(\tau)$. The baseline B is an adjustable parameter

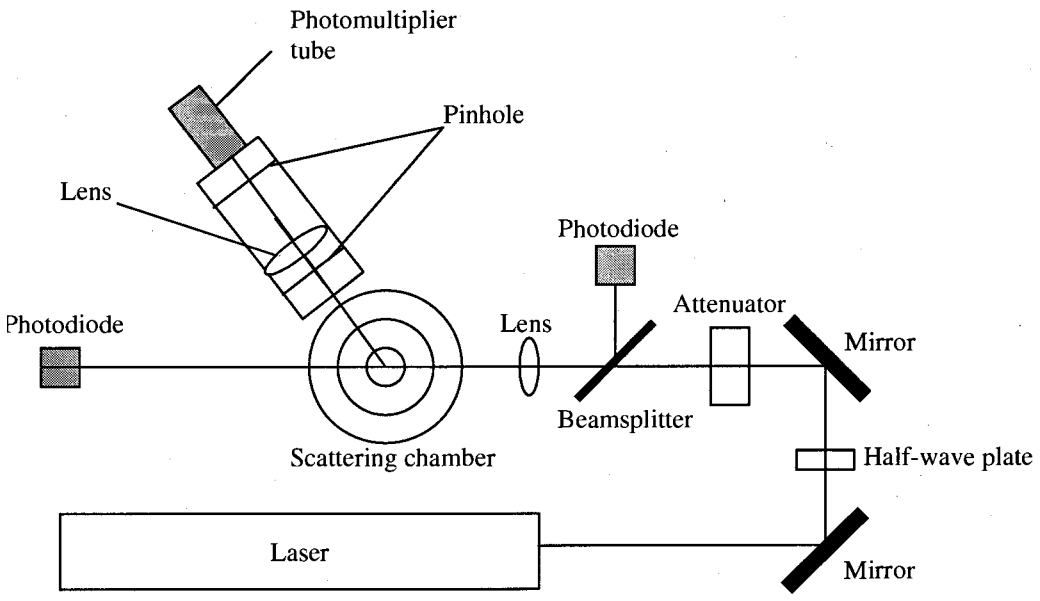

Figure 2.3: The schematic diagram of DLS apparatus. The light source is a 23 mW HeNe laser of wavelength 632.8 nm. Two mirrors are used to steer the incident beam through the sample and two lenses are used to focus the beam onto the center of the scattering cell and the photomultiplier tube, respectively. The half-wave plate is used to rotate the polarization of the laser beam from horizontal to vertical. The beamsplitter directs a part of the beam to a photodiode that reads the incident beam intensity; the other photodiode reads transmited beam intensity. The attenuator is used to adjust the light intensity. Two pinholes are used to adjust the range of scattering angle detected and the size of the phototube's viewable beam. Light scattered from the sample is detected by a photomultiplier tube mounted at a computer-controlled motorized goniometer, that makes measurements possible at a variety of scattering angles.

which will be determined from the fitting procedure and should be close to 1. In addition, $G_n(R)$ is also calculated from $G_i(R)$ using Eq. 2.50, where $G_i(R)$ is determined from the fitting procedure.

Fits to the data were made using a C-language fitting program which calls a non-linear least squares (nllsq) fitting function and various integration functions. The nllsq routine takes a set of N data points and fits a given model function with m adjustable parameters to the data. There are four adjustable parameters : two are the baseline B and the geometric factor β and the other two are the parameters which describe the distributions, the mean value and either m or the standard deviation for Schulz or Gaussian distributions, respectively.

The goodness-of-fit χ^2 is defined as,

$$\chi^2 = \frac{1}{N-m} \sum \frac{(y_i - f_i)^2}{s_i^2}, \tag{2.55}$$

where y_i, f_i, and s_i are the data, the fit and the uncertainty in the data, respectively, at the given delay time τ. The best fit is assumed to be the one which minimizes the χ^2.

2.4 Results and Discussion

An example of the intensity-intensity autocorrelation function data is shown in Fig. 2.4.a together with the fits of Eqs. 2.33 and 2.40 using Gaussian and Schulz distributions to the data. The data shown is for samples of 100 nm vesicles measured at scattering angle of 50°. The residuals, the difference between the fits and the data, for the data and the fits in Figs. 2.4.a, are shown in Fig. 2.4.b. The value of χ^2 is approximately the same for different

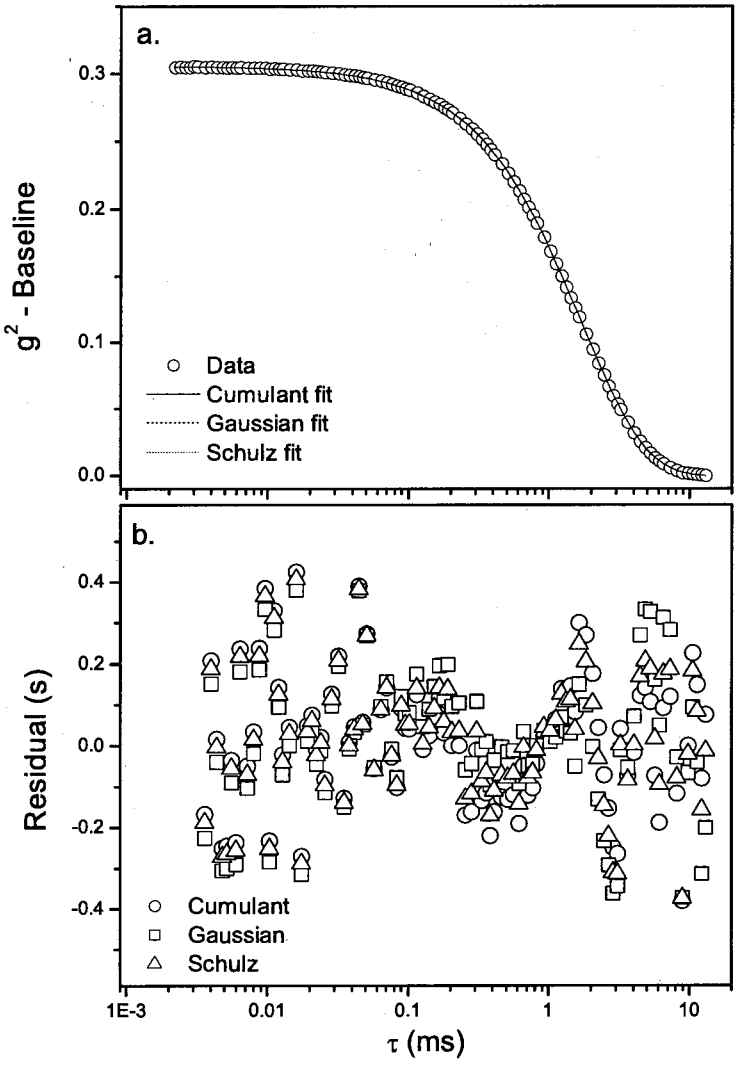

Figure 2.4: a. An example of the intensity-intensity autocorrelation function data shown together with the fits of Eqs. 2.33 and 2.40 using Gaussian and Schulz distributions. The data shown is for samples of 100 nm vesicles measured at scattering angle of 50°. b. The residuals (in the unit of standard deviation of the data s), the difference between the fits and the data, for the data and the fits in Fig. a.

methods, which is 0.4. This small value and the randomness of the residuals indicate that the theoretical expression for the intensity-intensity autocorrelation function is significantly consistent with the intensity-intensity autocorrelation function data for all different fitting functions.

2.4.1 Mean Radius $\overline{R_h}$ and Polydispersity σ_{R_h}

The mean radius $\overline{R_h}$ and the polydispersity σ_{R_h} for data of 50 and 100 nm vesicles taken at different scattering angles were determined using both the decay rate distribution and the moment-based analysis and the results are shown in Figs. 2.4.1.a and b, respectively. The values of $\overline{R_h}$ has been normalized to the values of $\overline{R_h}$ at a scattering angle of 20° to allow comparison of the q-dependence of $\overline{R_h}$ calculated for 50 nm and 100 nm vesicles. The results from both approaches are consistent. The mean radius $\overline{R_h}$ decreases with increasing q, and the q-dependence is more pronounced for the larger vesicles. The q-dependence of the mean radius is expected, since the radius of the vesicles is large. As explained previously, for such large particles, the scattered intensity diminishes as scattering angle increases. Therefore for polydisperse vesicles, more large vesicles are detected at the small scattering angles, while more small vesicles are detected at the large scattering angles. Results for σ_{R_h} also show some q-dependence. For 50 nm vesicles, a measured polydispersity is large at small scattering angle but small at the large scattering angle. However for 100 nm vesicles they are large at small and large angles and small in between.

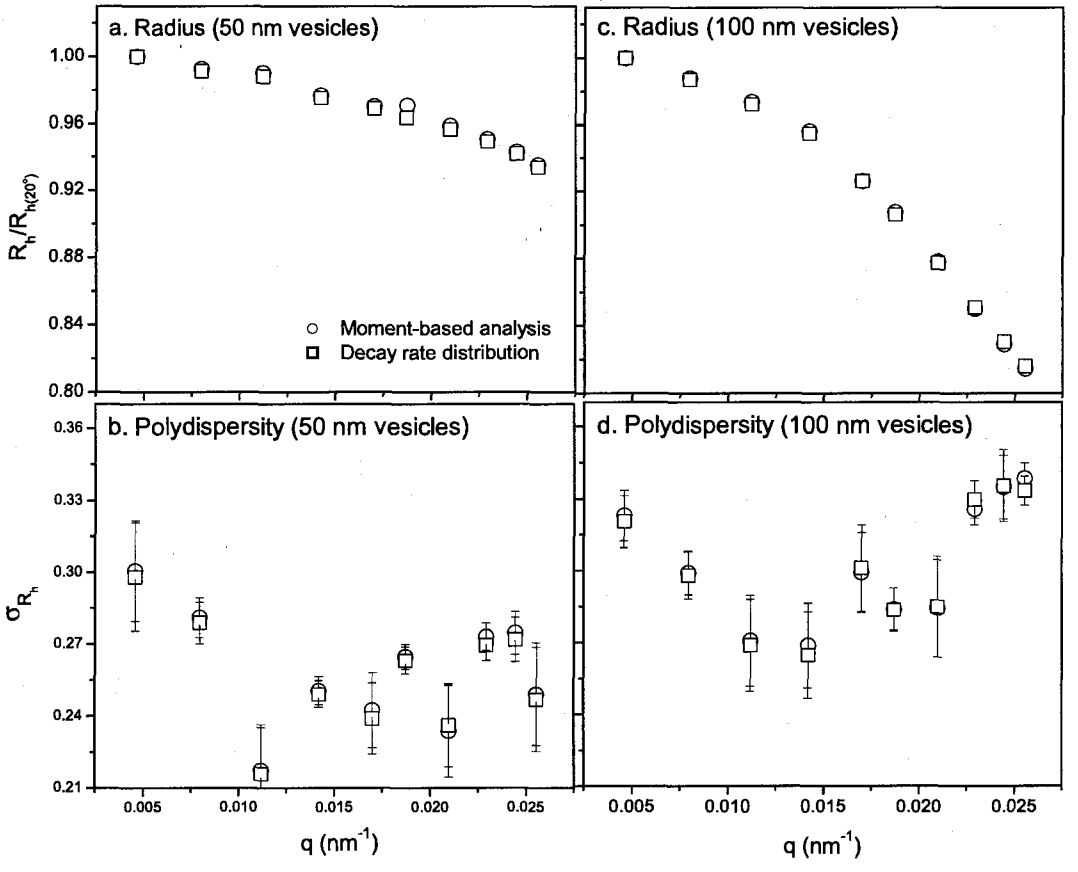

Figure 2.5: The mean radius $\overline{R_h}$ normalized by $\overline{R_h}$ at scattering angle of 20° of a. 50 nm vesicles and c. 100 nm vesicles as a function of the wavevector q. The associated polydispersity σ_{R_h} as a function of the wavevector q are shown in Figs. b and d for 50 nm and 100 nm vesicles, respectively. The values of $\overline{R_h}$ at a scattering angle of 20° are 69 and 108 nm for 50 and 100 nm vesicles, respectively. The results were determined using $g^{(1)}(\tau)$ consisting of either a decay rate distribution (Eq. 2.29) or moment-based analysis (Eq. 2.33). The error bars in Figs.b and d are the standard deviation of the mean from five measurements. The error bars in Figs.a and c are not shown because they are very small. (Eq. 2.33).

2.4.2 Mean Radius $\overline{R_i}$ and Polydispersity σ_{R_i}

The intensity-weighted mean radius $\overline{R_i}$ and polydispersity σ_{R_i} were determined for both a Gaussian and a Schulz distribution as a function of q. The results for 50 and 100 nm vesicles are shown in Fig. 2.6. There is no significant difference of the mean radius from both distributions, but polydispersity from Schulz distribution is larger than that for Gaussian distribution. Other fitting parameters are consistent. As expected, the intensity-weighted mean radius $\overline{R_i}$ also decreases as q increases, with the q-dependence of $\overline{R_i}$ more pronounced for larger vesicles for the reasons explained above. There is also some q-dependence of the polydispesity, consistent with that observed for σ_{R_h}.

2.4.3 Comparison of the Results from Decay Rate and Radius Distributions

In order to compare the mean radius and polydispersity determined from the decay rate and radius distribution, $\overline{R_h}$ and $\overline{R_i}$ as well as σ_{R_h} and σ_{R_i} are shown as a function of q in Fig. 2.7. The figure shows that there is a significant difference between the mean radii and between the polydispersities found using the decayrate and radius distributions. This reflects the fact that these are actually different averages; $\overline{R_i}$ is obtained by averaging over R while $\overline{R_h}$ is obtained by averaging over $1/R^{-1}$. $\overline{R_i}$ is larger than $\overline{R_h}$ for both Gaussian and Schulz distributions, and the Gaussian R_i is slightly smaller than the Schulz R_i. On the other hand, the Schulz σ_{R_i} is similar to σ_{R_h}, while the Gaussian σ_{R_i} is systematically smaller than both the Schulz σ_{R_i} and σ_{R_h}. The results showing that σ_{R_i} and σ_{R_h} are consistent only for σ_{R_i}

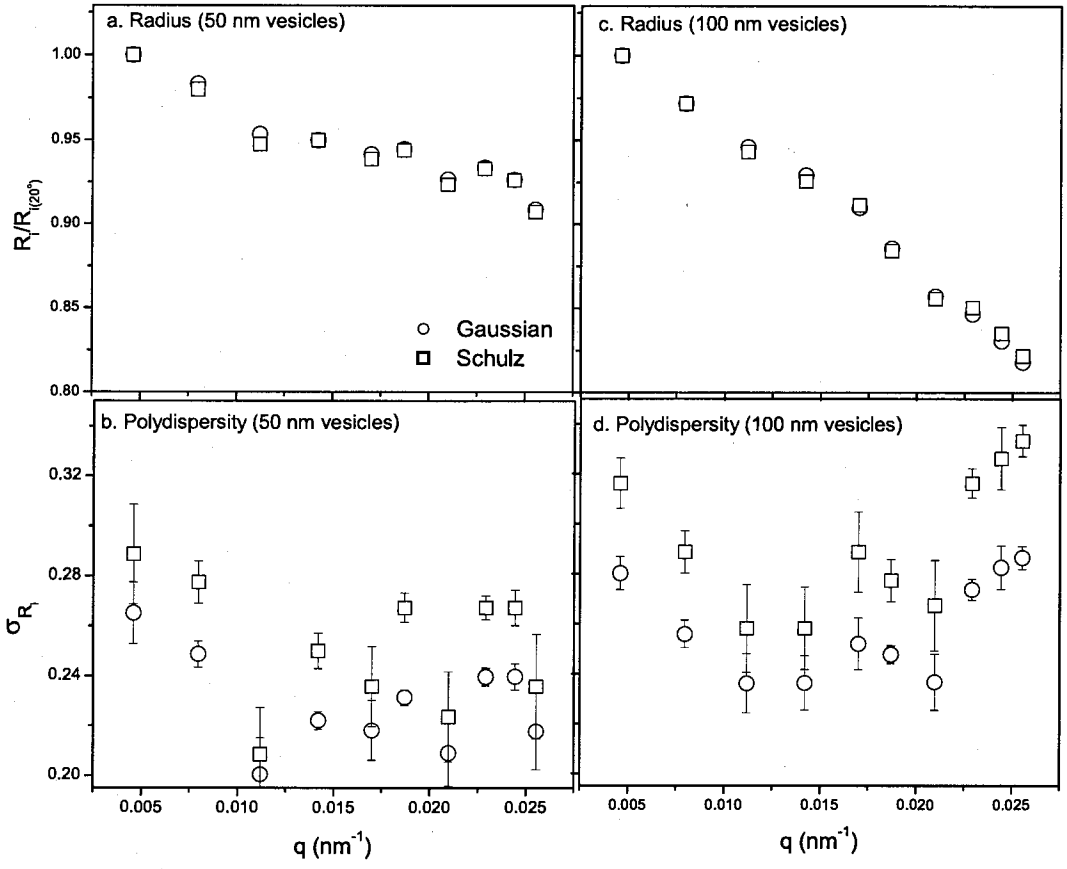

Figure 2.6: The intensity-weighted mean radius $\overline{R_i}$ of a. 50 nm vesicles and c. 100 nm vesicles as a function of the wavevector q. The associated polydispersities are shown in Figs.b and d for 50 nm and 100 nm vesicles, respectively. The results were determined using $g^{(1)}(\tau)$ expressed in terms of the intensity-weighted radius distribution $G_i(R)$ (Eq. 2.40), where Gaussian and Schulz distributions were used for $G_i(R)$. The error bars in Fig.b and d are the standard deviation of the mean from five measurements. The error bars in Fig.a and c are not shown because they are very small.

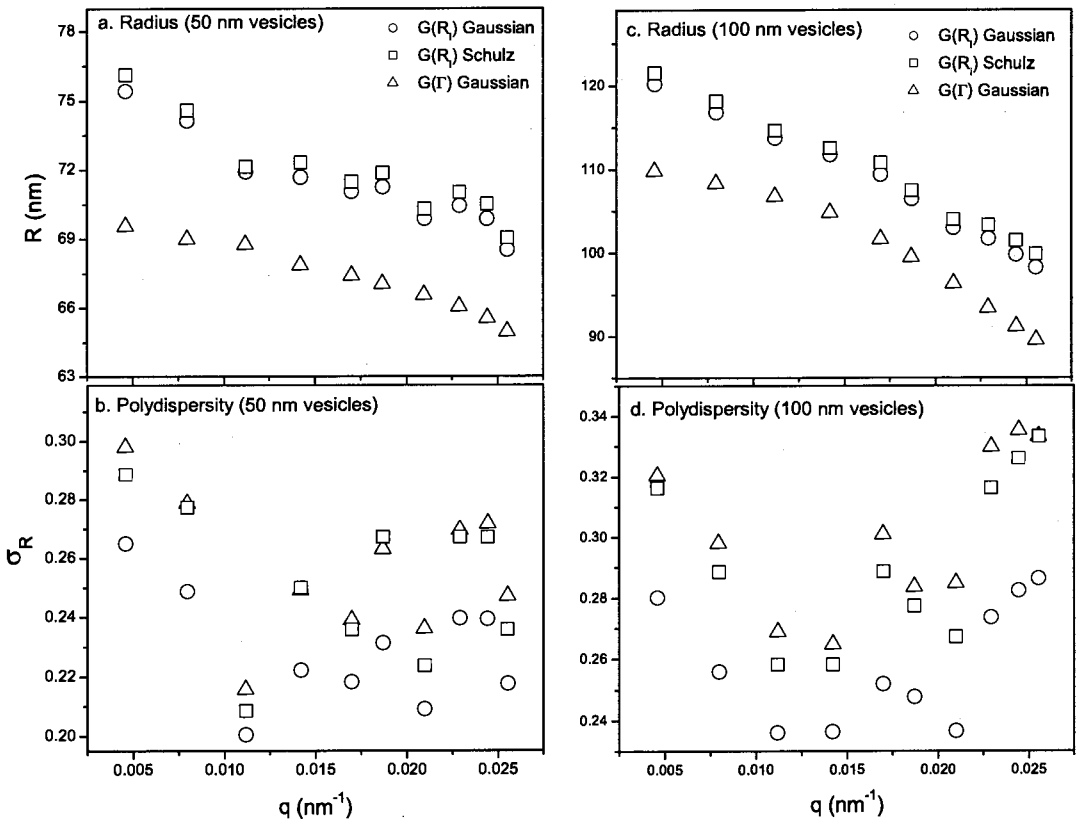

Figure 2.7: The mean radius determined from the intensity-weighted radius distribution $\overline{R_i}$ or decay rate distribution $\overline{R_h}$ as a function of the wavevector q for a. 50 nm vesicles and c. 100 nm vesicles. The associated polydispersities are shown in Figs.b and d for 50 nm and 100 nm vesicles, respectively.

of Schulz distribution indicate that Schulz distribution may be a better representation of vesicle size distributions.

2.4.4 Mean Radius $\overline{R_n}$ and Polydispersity σ_{R_n}

The results for the number-weighted mean radius $\overline{R_n}$ and polydispersity σ_{R_n} as a function of q for 50 and 100 nm vesicles are shown in Fig. 2.8. The values of $\overline{R_n}$ has been normalized to the value of R_o, the average radius from R_ns at all qs, excluding two smallest qs. For 50 nm vesicles, R_os are 54.3 nm and 58.8 nm for Gaussian and Schulz distributions, respectively. For 100 nm vesicles, R_os are 89.5 nm and 95.6 nm for Gaussian and Schulz distributions, respectively. Figures 2.8.a and c show the mean radii and Fig. 2.8.b and d show the polydispersities for 50 nm and 100 nm vesicles, respectively. The mean radius from Schulz distribution is slightly larger than that for Gaussian distribution as shown by the values of R_o. In contrast, polydispersity from Schulz distribution is smaller. Other fitting parameters are consistent. For Schulz distributions, q-dependence of $\overline{R_n}$ and σ_{R_n} is significantly reduced. For Gaussian distributions only $\overline{R_n}$ is significantly reduced; there is some q-dependence of σ_{R_n}.

There is a significant difference in the values found for $\overline{R_n}$ and σ_{R_n} depending on whether the Gaussian or Schulz distribution is used. The mean radius found using the Schulz distribution is larger than that found using the Gaussian distribution. The value of σ_{R_n} from the Gaussian distribution, however, is very large particularly at small q. The fact that analysis using the Schulz distribution produces values of $\overline{R_n}$ and σ_{R_n} which are q-independent indicates that the Schulz distribution may be a better representation of the vesicle size

distributions, a result which is consistent with the work of other authors [20].

The cause of the small values of $\overline{R_n}$ at the smallest q is not clear. However, it could be due to the fact that, in this q-range, the measurement is very sensitive to dust or aggregates in the sample. Neither would be accounted for in these distributions, which are monomodal. Alternatively, it could be caused by the fact that the type of distributions used does not match the size distribution of vesicles.

2.4.5 Number-Weighted Distribution Calculated from Intensity Weighted Distribution

Many researches use measurements of the intensity-weighted distribution to obtain either the number-weighted distribution or its moments. To investigate this practice, the number-weighted mean radius $\overline{R_n}$ and the associated polydispersity σ_{R_n} were also determined from the results for the intensity-weighted mean radius $\overline{R_i}$ and the associated polydispersity σ_{R_i} shown in Fig. 2.6 using Eq. 2.50. The results of the calculation using the Schulz distribution are shown in Fig. 2.9 together with the results for $\overline{R_n}$ and σ_{R_n} shown previously in Fig. 2.8. For this case, calculated values of $\overline{R_n}$ and σ_{R_n} are consistent with the results from direct fitting for $\overline{R_n}$ and σ_{R_n}. The results of the calculation using the Gaussian distribution are shown in Fig. 2.10 together with the results for $\overline{R_n}$ and σ_{R_n} shown previously in Fig. 2.8. For this case, calculated values of $\overline{R_n}$ and σ_{R_n} are significantly different with the results from direct fitting for $\overline{R_n}$ and σ_{R_n}; the results for $\overline{R_n}$ are much too small (less than 10 nm) and for σ_{R_n} are much too large (more than 100 %). Only results that can be calculated are shown.

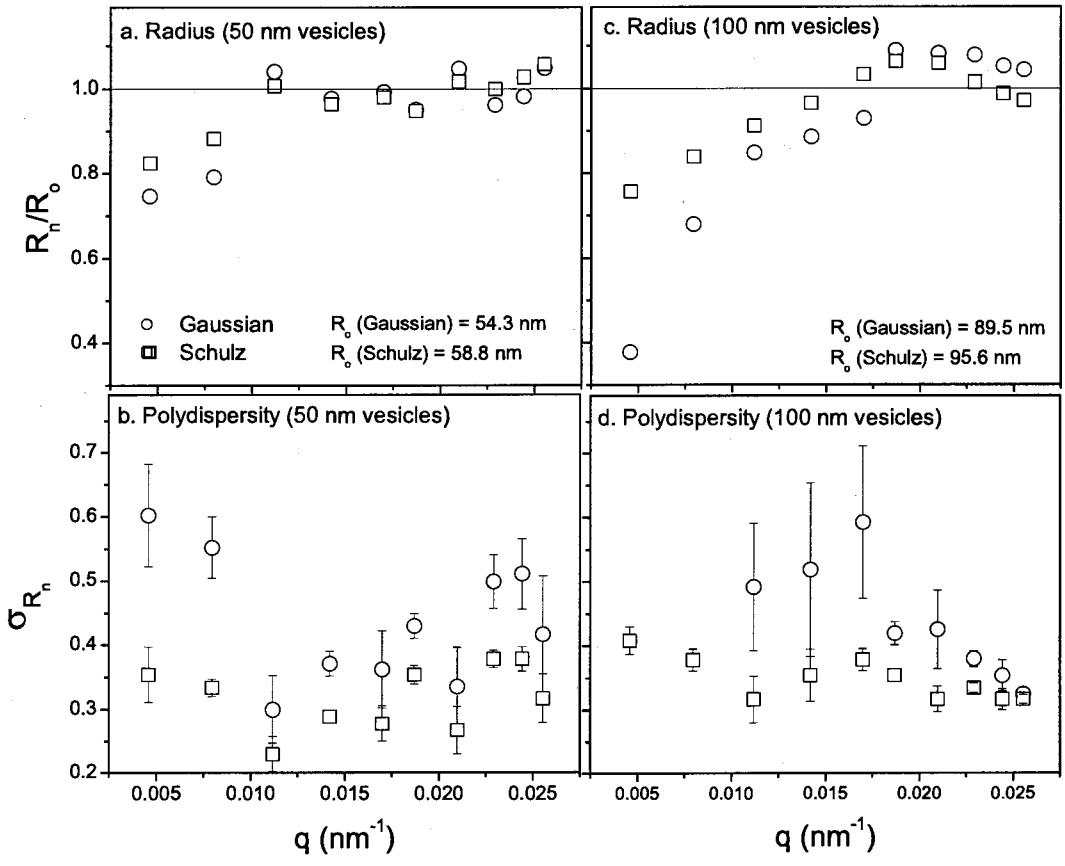

Figure 2.8: The number-weighted mean radius $\overline{R_n}$ of a. 50 nm vesicles and c. 100 nm vesicles as a function of the wavevector q. The associated polydispersities are shown in Figs.b and d for 50 nm and 100 nm vesicles, respectively. The results were determined using $g^{(1)}(\tau)$ expressed in terms of number-weighted radius distribution $G_n(R)$ (Eq. 2.47), where Gaussian and Schulz distributions were used for $G_n(R)$. $\overline{R_n}$ has been normalized to the value of R_o, the average radius from $\overline{R_n}$s at all qs, excluding two smallest qs. The error bars are the standard deviation of the mean from five measurements.

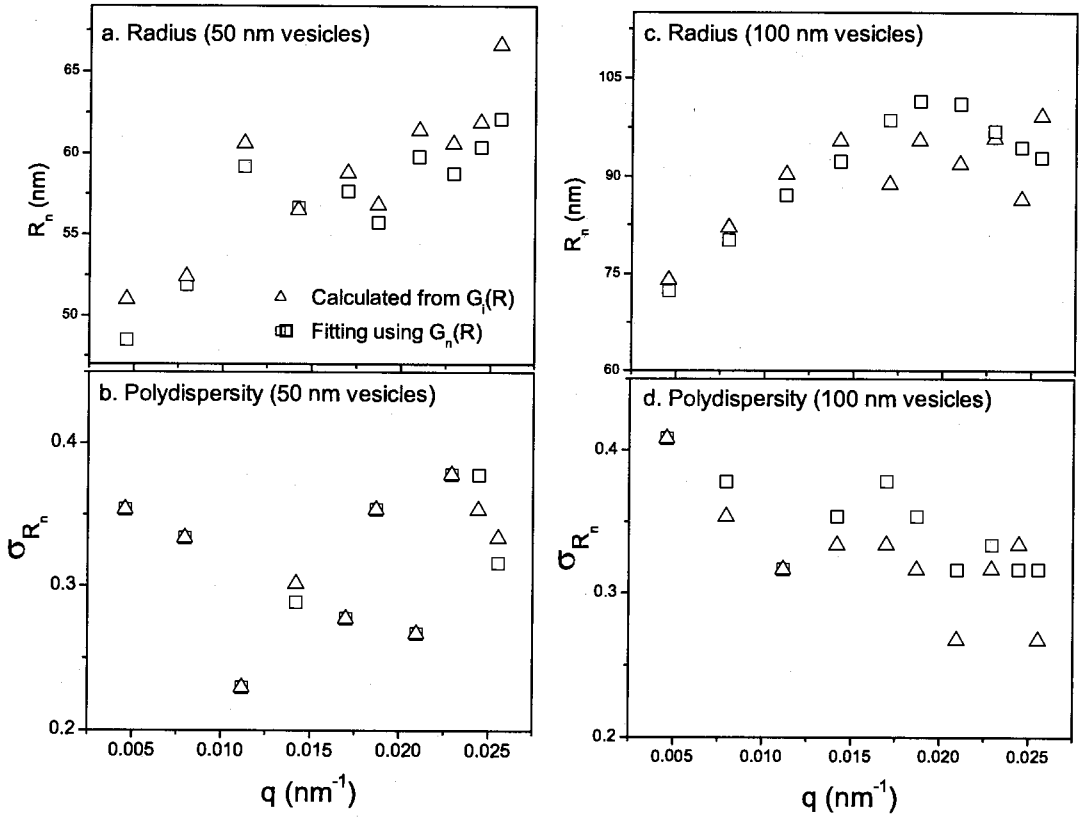

Figure 2.9: The number weighted mean radius $\overline{R_n}$ and σ_{R_n} calculated from $\overline{R_i}$ and σ_{R_i} for Schulz distribution. The results from directly fitting the number-weighted distribution to the data are also shown.

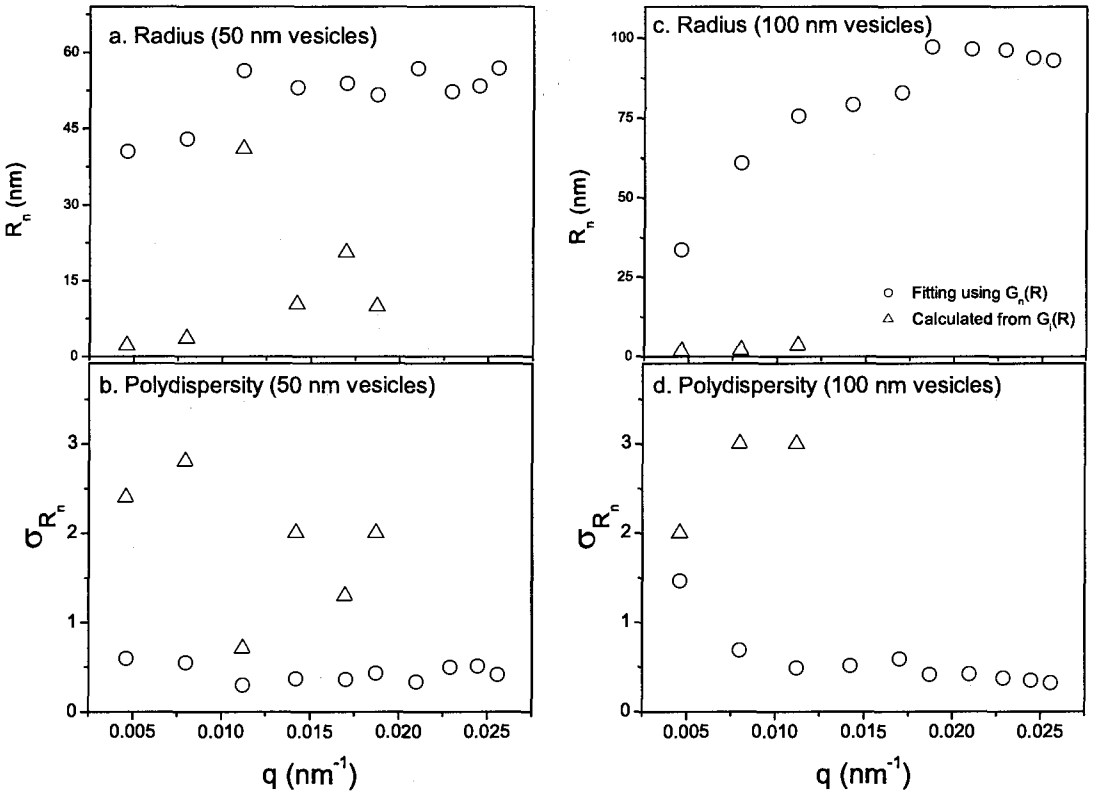

Figure 2.10: The number weighted mean radius $\overline{R_n}$ and σ_{R_n} calculated from $\overline{R_i}$ and σ_{R_i} for Gaussian distribution. The results from directly fitting the number-weighted distribution to the data are also shown.

The inconsistency in the results of $\overline{R_n}$ and σ_{R_n} between direct fitting and the calculation from $\overline{R_i}$ and σ_{R_i} when the Gaussian distribution is used may be due to the fact that these results are very sensitive to the polydispersity σ_{R_i}. To check this idea, I calculated $\overline{R_n}$ and σ_{R_n} from $\overline{R_i}$ and σ_{R_i} using Eq. 2.11 and a range of σ_{R_i} using $\overline{R_i}$ of 60 and 90 nm; results are shown in Figs. 2.11.a and 2.11.b, respectively. The values chosen for $\overline{R_i}$ are close to those measured for 50 and 100 nm vesicles. In the graph, the number-weighted values are normalized by the intensity-weighted values to make it easy to compare the results for different radii. When σ_{R_i} is small ($\sigma_{R_i} < 0.15$), $\overline{R_n}$ and σ_{R_n} are almost the same as $\overline{R_i}$ and σ_{R_i}, respectively, and the normalized values are close to 1. As σ_{R_i} increases, $\overline{R_n}$ becomes smaller than $\overline{R_i}$ while σ_{R_n} becomes larger than σ_{R_i}. For σ_{R_i} larger than a certain threshold value, $\overline{R_n}$ becomes very small, while σ_{R_n} increases. Values calculated using Gaussian distribution diverge abruptly near $\sigma_{R_i} < 0.15$, while values calculated using Schulz distribution remain reasonable to much higher polydispersity. The calculations show that converting intensity weighted- to number-weighted distributions using Gaussian distribution is problematic at higher polydispersity.

2.5 Summary

These studies show different analyzes used in determining the size distributions of vesicles from DLS data. The size distribution can be calculated from the decay rate distribution which is determined from the data-fitting procedure or can be determined directly from fitting using intensity- and number-weighted distributions. The size distributions resulting

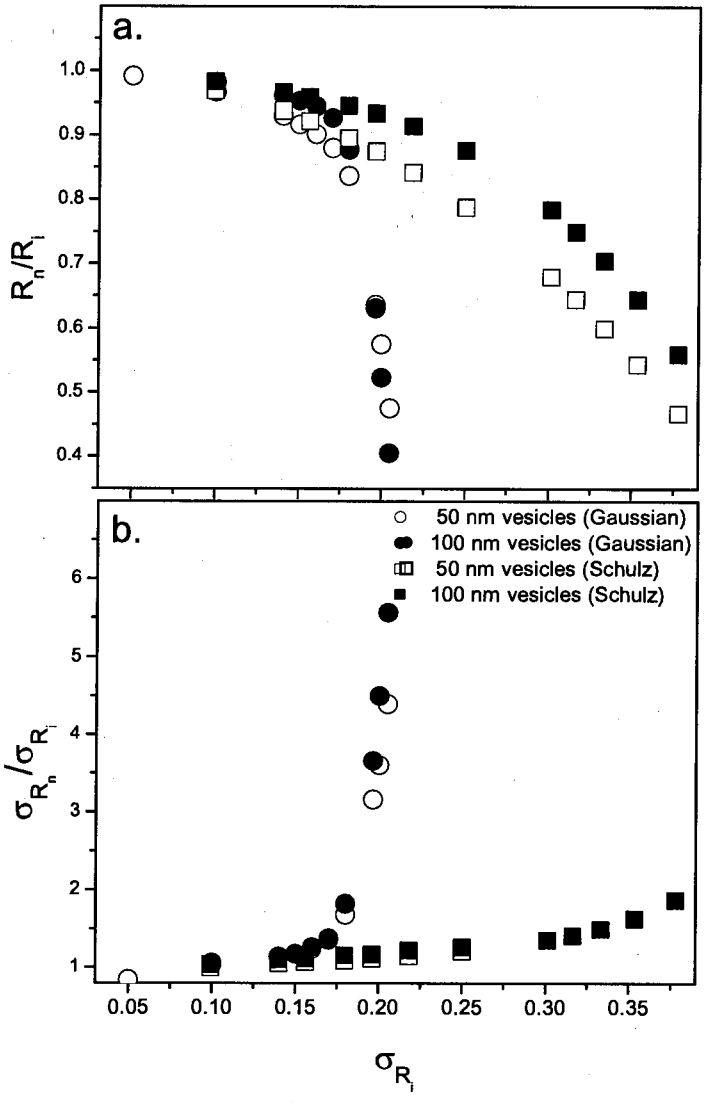

Figure 2.11: Values for a. $\overline{R_n}$ and b. σ_{R_n} calculated as a function of σ_{R_i} of vesicles with $\overline{R_i}$ values of 60 and 90 nm. The calculation was done using Eq. 2.50.

from the decay rate and the intensity-weighted radius distributions show a q-dependence. On the other hand, the q-dependence of the size distributions resulting from the number-weighted distributions reduces significantly only when Schulz distribution is used. When Gaussian distribution is used, there still some q-dependence especially on σ_{R_n}. The results indicate that Schulz distribution may be a better representation of size distribution of vesicles. The number-weighted distributions determined from direct fit to the data is consistent with the one calculated from intensity-weighted distributions only when Schulz distribution is used. When Gaussian distribution is used, there is a significant different between the values from direct fitting and calculation. This suggests that results obtained by an intensity-weighted distribution should be converted to number-weighted distribution with care, especially when the polydispersity is large.

Chapter 3

The Influence of the Pore Size Distribution on the Size Distribution and Lamellarity of Extruded Vesicles

3.1 Introduction

Vesicles are quasi spherical shells made from lipids that enclose an aqueous medium and separate it from an external aqueous medium. This characteristic makes vesicles a powerful tool in a wide range of applications [36, 37]. For example, since vesicles can compartmentalize certain active agents, they can be used as vehicles or carriers to deliver drugs to certain

sites of the body [38] or to deliver biomaterials such as DNA to various cells and microorganisms in order to alter their genetic code [39]. In addition, because of their similarities to cells, vesicles can also be used as model cells for research [40].

Vesicles can be produced in a wide range of sizes with different number of bilayers depending on the techniques applied. However, for most applications, unilamellar vesicles with the size between 25 nm to 250 nm and narrow distribution are of interest [36, 41]. This indicates that size, size distribution and number of lamellae (lamellarity) are important properties of the vesicles. In drug delivery, for example, having a narrow size distribution of vesicles averaging less than 50 nm radius has proved to be important in clinical success [42]. A narrow size distribution of vesicles is required because the circulation lifetime of drug-containing vesicles is size dependent [43]. Litzinger et al. [44] showed that vesicle size and polydispersity have a strong impact on dosage, targeting, and the rate of clearance from the body when vesicles are used to deliver drugs to specific targets. On the other hand, unilamellar vesicles have a relatively high encapsulation capacity compared to multilamellar vesicles of the same size.

Detergent dialysis, extrusion through small pores, and reverse-phase evaporation are three techniques that can be used to produce vesicles with radii between 25 and 250 nm [16, 36, 45, 46]. In detergent dialysis, the lipids are solubilized in detergent extract in the form of mixed micelles. The mixtures are then placed into a small volume dialysis bag, which in turn is placed into a large volume of buffer/aqueous medium. The free detergents will slowly diffuse into the buffer lowering the detergent concentration. When detergent

concentration is lower than their critical micelle concentration, the unilamellar vesicles with mean radius of around 20 nm will be formed [45]. This radius can be increased if cholesterol is introduced to the samples. In reverse-phase evaporation, the lipid is dissolved in an organic solvent, followed by the addition of aqueous medium which results in the formation of a homogenous emulsion. The organic solvent is then removed by rotary evaporation under reduced pressure resulting in the formation of unilamelar vesicles with a mean radius of around 240 nm [46]. In extrusion, the lipid is dispersed in aqueous medium which forms the multilamellar vesicles (MLVs). The MLVs are then pushed through pores in PCTE membranes repetitively [16]. The size and lamellarity of the vesicles vary from 25 nm to 200 nm and unilamellar to multilamellar, respectively, depending on the pore size used and the pressure applied [3, 47]

In detergent dialysis and reverse-phase evaporation, the detergent and the organic solvent are required to be removed after the vesicles are formed. Practitioners are concerned with incomplete removal of detergent and organic solvent from the samples. The incomplete removal of the organic solvent, such as chloroform or methanol, for example, can contribute to toxicity and influence the stability of the vesicles [48]. In addition, the time course for both methods in producing LUVs is on the order of several hours. Since extrusion requires no agents such as detergents or organic solvents, this technique has advantages over detergent dialysis and reverse-phase evaporation techniques. Moreover the time necessary for extrusion is short, typically of the order of a few minutes.

A number of studies have been conducted to investigate the parameters influencing the

size and lamellarity of extruded vesicles. These include studies of the influence of pore size on the size and lamellarity of the vesicles [47, 49], the effect of lipid composition, extrusion pressure and temperature on the size of vesicles [50], the influence of pore size and extrusion pressure on the size of the vesicles [3] and the effect of a polymer lipid and freeze-thawing process on the size and lamellarity of vesicles [51].

The size distribution of the vesicles can be characterized by different methods such as : freeze-fracture-electron microscopy [35, 47], cryogenic transmission electron microscopy [52, 53], field flow fractionation [54], static light scattering [55] and DLS [32, 56, 57, 58, 59]. In particular DLS has been used extensively because sample preparation is simple, the measurement is noninvasive and the measurement time is relatively short compared to other methods, including static light scattering.

The lamellarity of the vesicles can be estimated using an external or accessible surface determination [36, 60]. These methods require particular marker lipids which provide a signal and can be changed upon the addition of a particular external agent. There are various methods which estimate the lamellarity of vesicles using accessible surface determination, including: nuclear magnetic resonance (NMR) [16], electron paramagnetic resonance (EPR) [60], and fluorescence spectroscopy [60, 61]. For example, in ^{31}P-NMR, the paramagnetic ion Mn^{2+} interacts with the phosphate of the phospholipids which broadens the ^{31}P-NMR resonance. Assuming that Mn^{2+} is membrane impermeable so that it only interacts with the phospholipids at the outer leaflet of the outermost bilayer, vesicle lamellarity can be estimated by the ratio of the signal before and after the introduction of Mn^{2+}. Similar way

is shown in EPR and fluorescence spectroscopy using different markers and external agents; in EPR, CAT-16 and ascorbate are used as the marker and external agent, respectively; in fluorescence spectroscopy, fluorescent lipids and sodium dithionite are used as the marker and external agent, respectively. Gruber and Schindler [60] compare these different methods and found that they are consistent.

Using pore sizes varying from 15-200 nm, Mayer et al. [47] showed that small pores produce unilamellar vesicles with relatively narrow distributions, while large pores generate multilamellar vesicles or combinations of unilamellar and multilamellar vesicles with relatively broad distributions. They also observed the dependence of vesicle size on pore size and found that the radius of vesicles increases with the radius of pores. When small pores were used, the radius of the vesicles is larger than or comparable to the pore size. However, when large pores were used, the opposite was true; vesicle size became smaller than the pore size and deviated from it as pore size increased. Although larger pores can be used to produce larger vesicles, the vesicles produced are multilamellar and polydisperse, and their size does not represent the size of the pores. This is probably one of the reasons that a nominal pore radius of 50 nm is most frequently used in extrusion (in practice, nominal size is an upper bound and the average pore size is somewhat smaller). This limits the application of the technique in terms of the size of vesicle produced.

Knowledge of the factors influencing the size, the polydispersity and the lamellarity of extruded vesicles produced using large pores may extend the usefulness of extrusion techniques to larger vesicle size. For example, applying smaller pressure during extrusion

results in vesicles 20% larger than applying higher pressure [3]. Another factor that can affect the polydispersity of the vesicles is the polydispersity of the pores. There is a possibility that large polydispersity of extruded vesicles is produced by polydispersity of the pores. However, most previous studies mentioned used the nominal value of the pores and no polydispersity of the pores was available, so this relationship could not be explored. Detailed characterization of size distributions of the pores and associated extruded vesicles should reveal the relation between the polydispersities of pores and vesicles.

In this chapter, I describe experiments investigating the influence of the pore size distribution on the size distribution and lamellarity of extruded vesicles. Characterization of the pore size and vesicle lamellarity will be described; characterization of vesicle size has been described in Chapter 2. The size distribution of the pores will be compared to the size distribution of vesicles in order to see the relationship between the two. The results for size distribution and lamellarity of extruded vesicles are used to discuss the factors influencing the properties of extruded vesicles.

3.2 Materials and Methods

3.2.1 Materials

The lipids used, 1-palmitoyl-2-oleoyl-*sn*-glycero-3-phosphatidylcholine (POPC) and 1-palmitoyl-2-(6-((7-nitro2-1,3-benzoxadiazol-4-yl)amino)caproyl)-sn-glycero-3-phosphatidylcholine (NBD-PC) were purchased from Avanti Polar Lipids Inc. (Alabaster, AL). The PCTE membranes with nominal pore radii of 25 and 200 nm were purchased from Osmonics Inc. (Livermore,

CA) and nominal pore radii of 50 and 100 nm manufactured by Whatman Nucleopore Inc. (Clifton, NJ) were purchased from VWR Canlab (Missisauga, ON).

3.2.2 PCTE Pore Size Measurements

The size of the pores in PCTE membranes was characterized using scanning electron microscopy (SEM). The microscope used was FEI DualBeam Strata 235 Field-Emission Scanning Electron Microscope. Prior to the measurements, the PCTE membranes were carbon coated to prevent electron accumulation on the membrane surface due to the non-conductivity of the membranes. The images were analyzed to determine pore radius and the results were displayed in a histogram. A Gaussian distribution was fit to the histogram data from which the mean radius and the polydispersity were determined. In the text, PCTE membranes with nominal pore radii of 25, 50, 100, and 200 nm are defined as 25 nm, 50 nm, 100 nm, and 200 nm pores, respectively.

3.2.3 Vesicle Size Measurements

The preparation of the samples of vesicles is similar to that explained in Subsection 2.3.2. POPC lipid dispersions were extruded through PCTE membranes with nominal pore radii ranging from 25 to 200 nm. The samples were extruded at applied pressures of 300 psi when 25 nm and 50 nm pores were used, and 250 and 50 psi when 100 nm and 200 nm pores, respectively, were used. The lower pressure applied for the larger pores is due to the fact that the flowrate of the dispersion is too high when higher pressure applied. The pressures applied are to produce vesicle sizes as small as possible. Previous studies showed that the

radius of vesicles decreases with the pressure applied during extrusion [3].

The size distributions of the vesicles produced were characterized using DLS. The DLS apparatus has been explained in Subsection 2.3.3. The expression for the intensity-intensity autocorrelation function given by Eq. 2.25 was fit to the correlation function data, Eq. 2.47 was used for the field-field autocorrelation function and the number-weighted radius distribution $G_n(R)$ was assumed to follow the Schulz distribution. The number-weighted mean radius and the polydispersity were determined from the fitting procedure.

3.2.4 Determination of Vesicle Lamellarity

Vesicle lamellarity was determined using a fluorescence quenching assay [60, 61]. The assay is based on the fact that fluorescent-lipids (NBD-lipids) such as NBD-PC can be quenched by exposure to a solution of sodium dithionite. When a solution of sodium dithionite is introduced to the sample of vesicles made from the mixture of lipid and NBD-lipid, the exposed NBD-lipid will be quenched, which results in a reduction of the fluorescence intensity. The ratio of intensity difference to the original intensity indicates the fraction of lipids exposed to the outside of the solution. The number of bilayers can then be estimated from this information.

This assay is valid with the assumptions that: NBD-lipids are randomly distributed in the bilayer/s, the redistribution of NBD-lipids between inner and outer leaflets of the bilayer (flip-flop) is negligible and membrane permeation of sodium dithionite is negligible during the time course of experiments.

Samples of vesicles were prepared from mixtures of POPC and NBD-PC, with the

amount of NBD-PC less than 1 mol %. POPC and NBD-PC were dissolved separately in chloroform and the aliquot required to achieve the desired concentration was taken and put in a round-bottom flask. The solvent was removed by rotary evaporation. Residual solvent was removed by placing the flask under vacuum overnight. The lipid film was then dispersed in a solvent of 10 mM Tris with a pH of 7.4. The dispersion was then taken through the freeze-thaw-vortex process and extruded once through 2 PCTE membranes with nominal pore radius of 200 nm (pre-extrusion). The pre-extruded vesicles were then extruded through PCTE membranes of required pore sizes.

The fluorescence assay was done using a PTI Quanta Master Luminescence Spectrofluorimeter. Two milliliters of sample were put into a quartz cell, which was then placed in the Spectrofluorimeter. The sample was excited using light with a wavelength of 490 nm and the emission was detected at a wavelength of 532 nm. The values of excitation and emission wavelengths were chosen after doing excitation and emission scans before the measurements. One of the scan results is shown in Fig. 3.1.

The fluorescence intensity was monitored for 300 s during the measurements. Sodium dithionite solution was added 60 s after the beginning of the measurement and Triton X-100 was added after 250 s. Sodium dithionite quenches the NBD-PC in the outer leaflet of unilamellar vesicles or in the outer leaflet of the outermost bilayer of multilamellar vesicles. For simplicity, lipids located in these leaflets are defined as the outer lipids in the text. Triton X-100 solution was used to lyse vesicles, exposing all of the lipids to sodium dithionite and quenching NBD-PC located in the inner leaflet of bilayer of unilamellar vesicles or inner

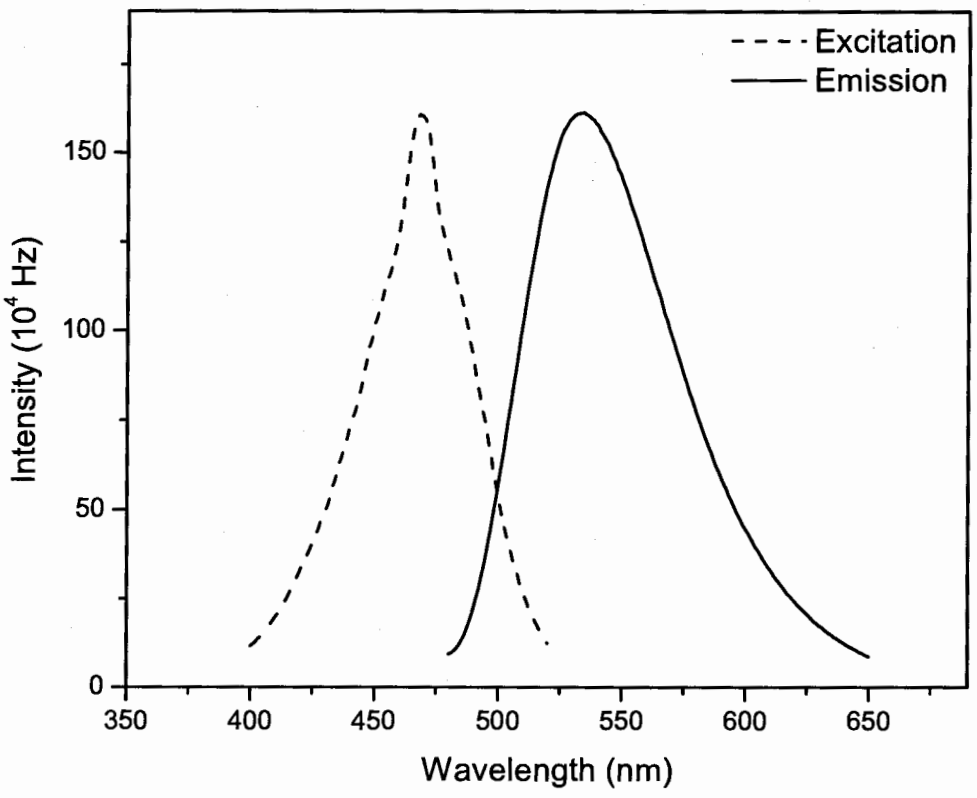

Figure 3.1: Emission and excitation scans for POPC:NBD-PC vesicles.

leaflet of the outermost bilayer plus inner bilayers of multilamellar vesicles. For simplicity, lipids located in these leaflets are defined as the inner lipids in the text.

The fraction of inner lipids can be calculated through the relation,

$$N_i = \left(\frac{I_D - I_T}{1 - I_T} \right), \tag{3.1}$$

where I_D and I_T are the normalized intensities after introduction of sodium dithionite and Triton X-100, respectively. In these studies, the NBD-PC molecules are assumed to be located randomly among the POPC molecules; hence, the fraction of outer lipids or inner lipids can be represented by the fraction of outer NBD-PC or inner NBD-PC. This is reasonable, since both lipids were dissolved in organic solvent, chloroform, and were well mixed.

For small vesicles, the effect of the radius of curvature on the amount of inner lipids and outer lipids in the vesicle bilayer/s may need to be taken into account. The number of lipids in two leaflets of a bilayer is proportional to the area of the sphere formed by those leaflets. The radii of those spheres differ by the thickness of the bilayer. For unilamellar vesicles, the fraction of inner lipids as a function of vesicle radius can be estimated using the relation,

$$N_i(unilamellar) = \left(\frac{(R-t)^2}{R^2 + (R-t)^2} \right), \tag{3.2}$$

where R and t are the vesicle radius and thickness of the bilayer, respectively. For bilamellar vesicles, the fraction of the inner lipids can be estimated using the relation,

$$N_i(bilamellar) = \left(\frac{(R-t)^2 + (R-d)^2 + (R-d-t)^2}{R^2 + (R-t)^2 + (R-d)^2 + (R-d-t)^2} \right), \tag{3.3}$$

where d is the separation between the bilayers.

Figure 3.2 shows the fraction of the inner lipids for unilamellar and bilamellar vesicles as a function of the vesicle radius assuming bilayer thickness of 3.9 nm [62] and separation between bilayers d of 10 nm [47]. For simplicity, the lines in Fig. 3.2 are called the unilamellar and bilamellar lines for unilamellar and bilamellar vesicles, respectively. If the fraction of the inner lipids from vesicles with a particular radius estimated from Eq. 3.1 is close to the unilamellar line, the vesicles are assumed to be unilamellar. If the fraction is above the unilamellar line, the vesicles may be multilamellar or both unilamellar and multilamellar. If the fraction is close to the bilamellar line, the vesicles may consist of only bilamellar vesicles, or combination of unilamellar, bilamellar and more than two bilayer vesicles. Fractions above bilamellar line may indicate that vesicles are multilamellar. For the purpose of these studies, it is assumed that vesicles only have up to 2 bilayers (bilamellar vesicles).

The fraction of unilamellar (f_1) and bilamellar (f_2) vesicles, then, can be determined from the value of N_i from the fluorescence quenching assay using the relation,

$$N_i = f_1 * N_i(1\ bilayer) + f_2 * N_i(2\ bilayers), \tag{3.4}$$

where $f_1 + f_2 = 1$.

3.3 Results and Discussions

3.3.1 Pore Size Distribution

SEM images were taken of at least 30 areas chosen randomly from each PCTE membrane. Typical SEM micrographs of surfaces of PCTE membranes are shown in Fig. 3.3. The mean

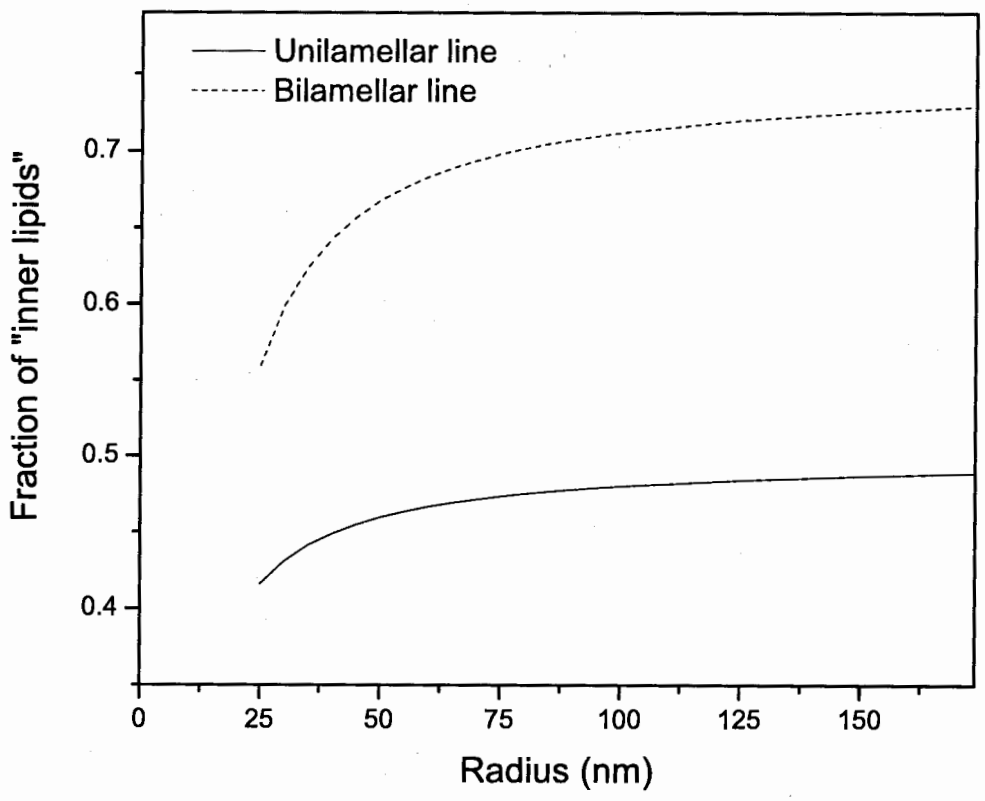

Figure 3.2: Fraction of the inner lipids for unilamellar and bilamellar vesicles as a function of vesicle radius.

radii and the polydispersities of the pores in these images were determined by analyzing 556, 365, 596 and 1028 pores for 25 nm, 50 nm, 100 nm and 200 nm pores, respectively. The radius data was plotted as a histogram and a Gaussian distribution was fit to the data to estimate the mean radius and the standard deviation.

Figures 3.4.a, b, c and d show the data for the nominal pore radii of 25 nm, 50 nm, 100 nm and 200 nm, respectively. The figure also contains the fits of the Gaussian distribution to the data. The mean radius and the standard deviation (written in terms of the polydispersity) resulting from the fits are summarized in Table 3.1.

Nominal Radius (nm)	Measured Radius (nm)	Polydispersity
25	31.4	0.153
50	36.5	0.101
100	65.2	0.086
200	155.2	0.105

Table 3.1: The mean radii and the polydispersities of the pores.

The results show a significant difference between the nominal pore radius and the measured pore radius of PCTE membranes. The membrane with nominal pore radius of 25 nm has a measured mean radius 25.6 % larger than the nominal pore radius, while membranes with nominal pore radii of 50, 100 and 200 nm have measured mean radii of 27.0, 34.8 and 22.4 %, respectively, smaller than the nominal pore radii. In addition, the polydispersity decreases with increasing nominal pore size.

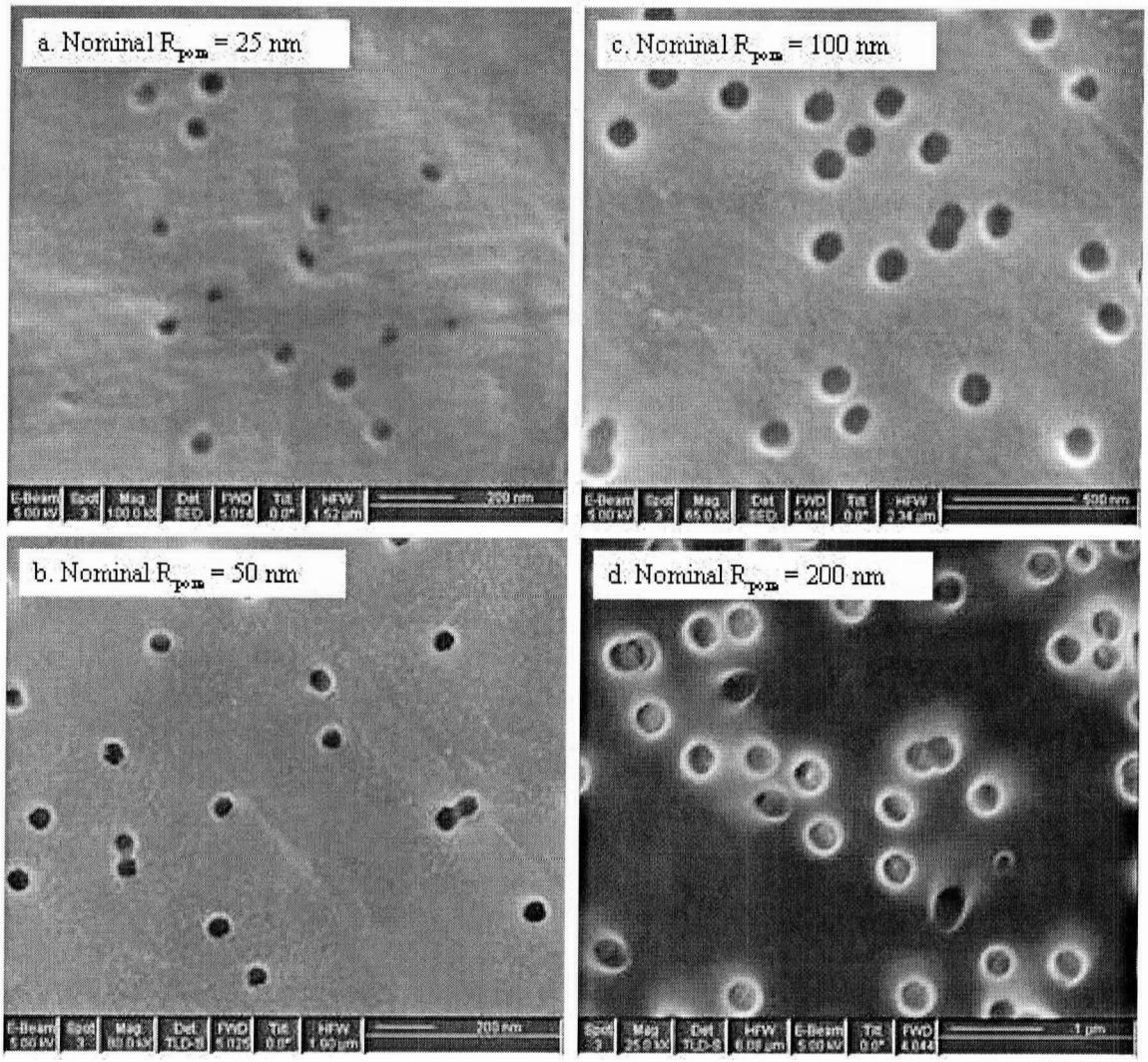

Figure 3.3: Scanning electron micrographs of surfaces of PCTE membranes with nominal pore radii of a. 25 nm, b. 50 nm, c. 100 nm, and d. 200 nm.

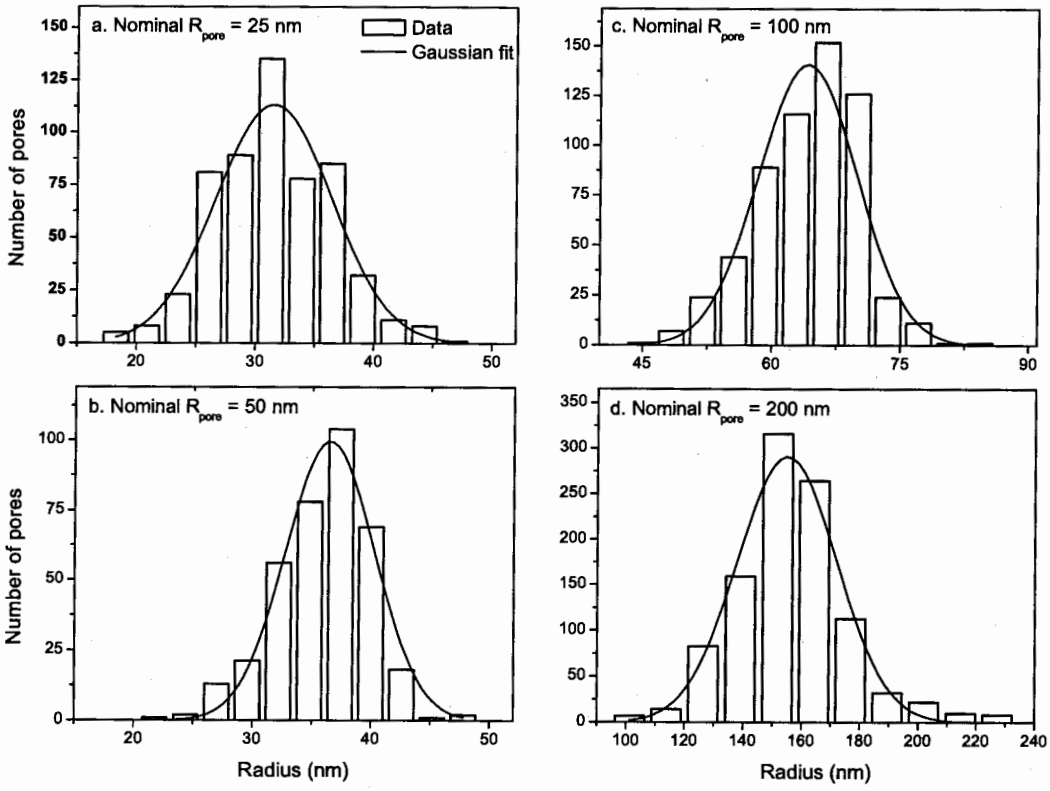

Figure 3.4: Histogram of pore radius data for a. 25 nm, b. 50 nm, c. 100 nm, and d. 200 nm pores and the fits to the data.

3.3.2 Vesicle Size Distribution

The results of the DLS measurements of the size distributions of vesicles produced using different sizes of the pores are plotted as a function of nominal pore radius. Figure 3.5.a and b show the mean radii and the polydispersities of the vesicles, respectively, as a function of the nominal pore radius. For comparison, the mean radii and polydispersities of the pores from Table 3.1 are also shown. The error bars in Fig. 3.5 are the uncertainties from the fits. The figure shows that the mean radii of vesicles produced using 25 nm and 50 nm pores are larger than the measured mean radii of the pores. In contrast, the mean radii of the vesicles produced using 100 nm and 200 nm pores are smaller than the measured mean radii of the pores. The figure also shows that the polydispersity of the vesicles increases with the radius of the pores up to a nominal radius of 100 nm and levels off for larger pores. The polydispersity of the vesicles is always larger than the polydispersity of the pores. This suggests that the polydispersity of the vesicles is not strongly dependent on the polydispersity of the pores but is mainly dependent on pore size. To compare the size distributions of pores and vesicles, probability distribution functions representing pore size distribution (Gaussian) and vesicle size distribution (Schulz) are plotted. Figures 3.6.a, b, c and d show radius distributions of 25 nm, 50 nm, 100 nm and 200 nm pores, respectively, and associated vesicles produced.

The fact that the polydispersity of the vesicles is dependent mainly on the size of the pores but not on the polydispersity of the pores raises the question of how the size of the pores influences the polydispersity of extruded vesicles. One possible explanation is that the

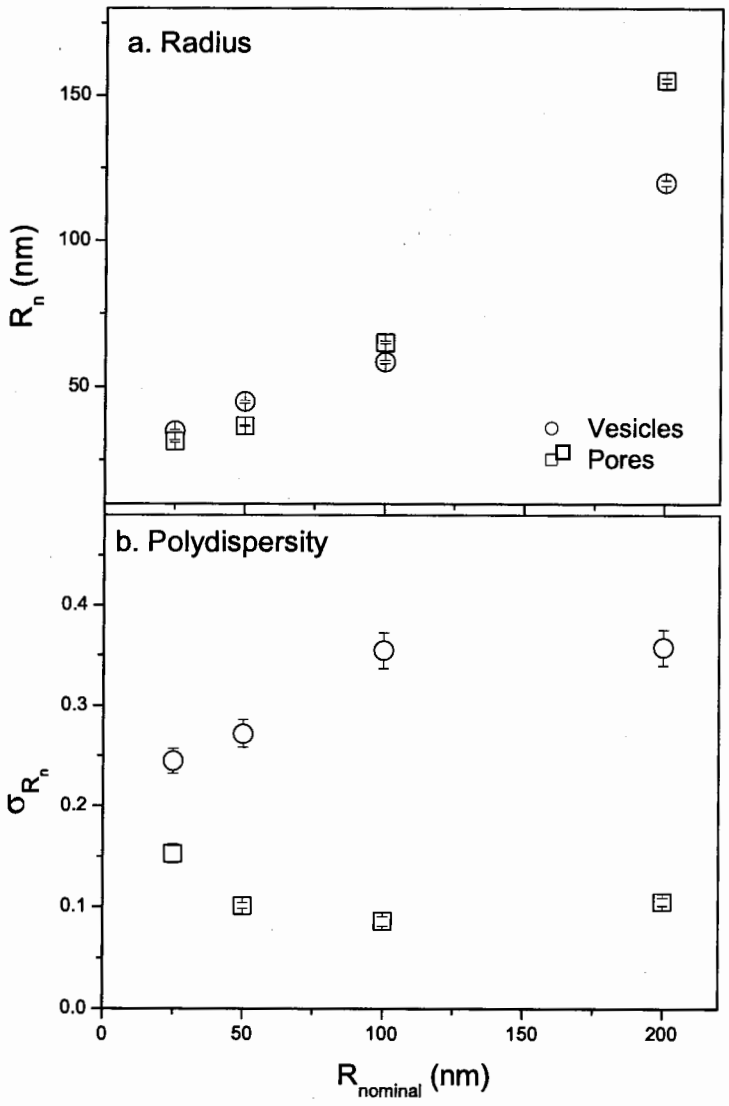

Figure 3.5: a. The mean radii R_n and, b. the polydispersities σ_{R_n} of the extruded vesicles and the pores as a function of the nominal pore radius $R_{nominal}$. The error bars are the uncertainties from the fits

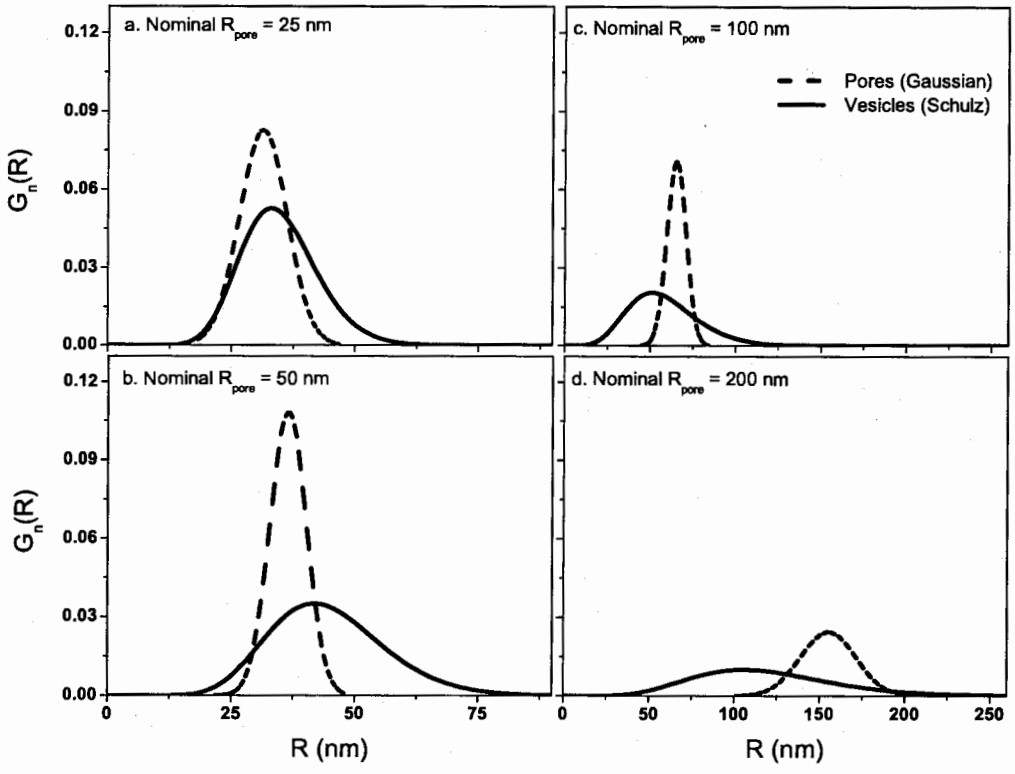

Figure 3.6: Comparison of the radius distributions of the vesicles and the pores for vesicles extruded through PCTE membranes with nominal pore radii of a. 25 nm, b. 50 nm, c. 100 nm, and d. 200 nm. The dashed lines represent radius distributions of the pores determined from the fits in Fig. 3.4, while the solid lines are the number-weighted radius distribution of vesicles resulting from the DLS fits.

pre-extruded samples contain small vesicles that can pass through large pores easily without being ruptured. When small pores are used, the polydispersity is small because the small vesicle size is comparable to the size of the pores. However, when large pores are used, the polydispersity is large since the small vesicles are smaller than the size of the pores; the vesicle distribution is, therefore, a combination of small vesicles and vesicles comparable to the size of the pores. The existence of small vesicles is supported by previous studies of the vesicle size distributions using fractionation of vesicles through column chromatography [63].

The presence of small vesicles may be caused by the freeze-thaw-vortex (FTV) process. In order to investigate this, experiments were done to compare size distributions of vesicles produced using 100 nm pores with and without FTV process and the results is shown in Fig. 3.7. Applying the FTV process does appear to produce more small vesicles as indicated by a smaller mean radius and a larger polydispersity. However, even in the non-FTV vesicles, there are still many vesicles smaller than the size of the pores that must be caused by other means. For example, small vesicles could be produced spontaneously when lipid is dispersed in water or as a consequence of the process of extrusion.

3.3.3 Vesicle Lamellarity

Samples of POPC:NBD-PC lipid dispersion were extruded at least 10 times each through PCTE membranes with nominal pore radii varying from 25 nm to 200 nm and were then subjected to the fluorescence quenching assay. Figure 3.8.a shows the fluorescence intensity of the POPC:NBD-PC vesicles before and after the introduction of sodium dithionite and

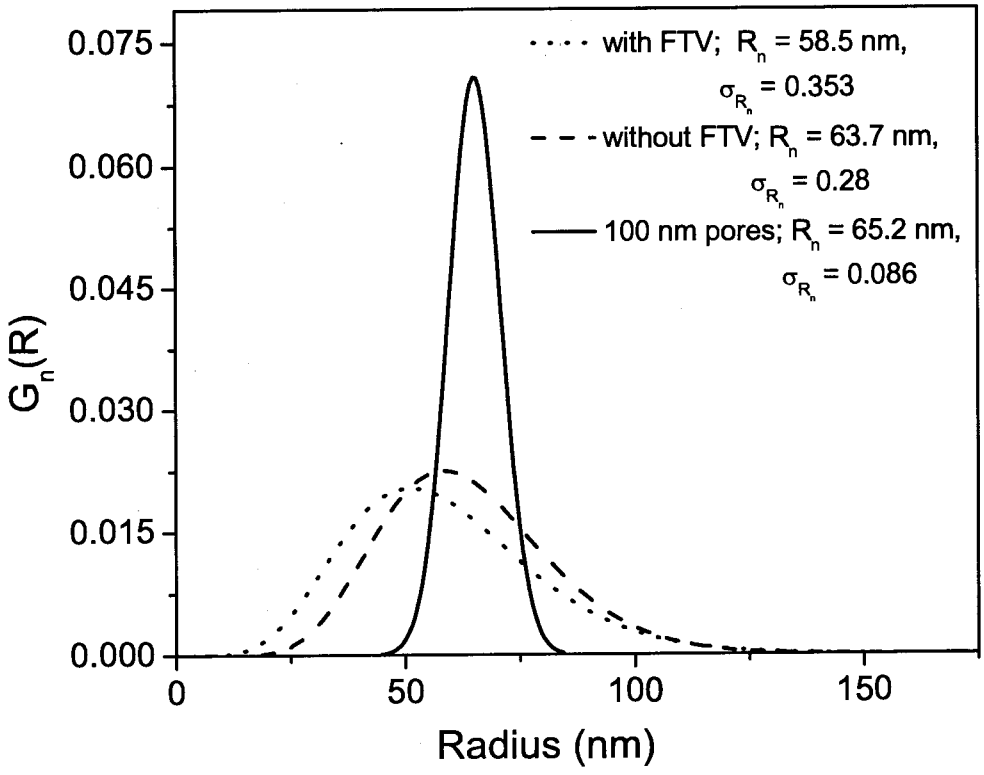

Figure 3.7: Radius distribution of 100 nm vesicles prepared with and without FTV process and radius distribution of the 100 nm pores.

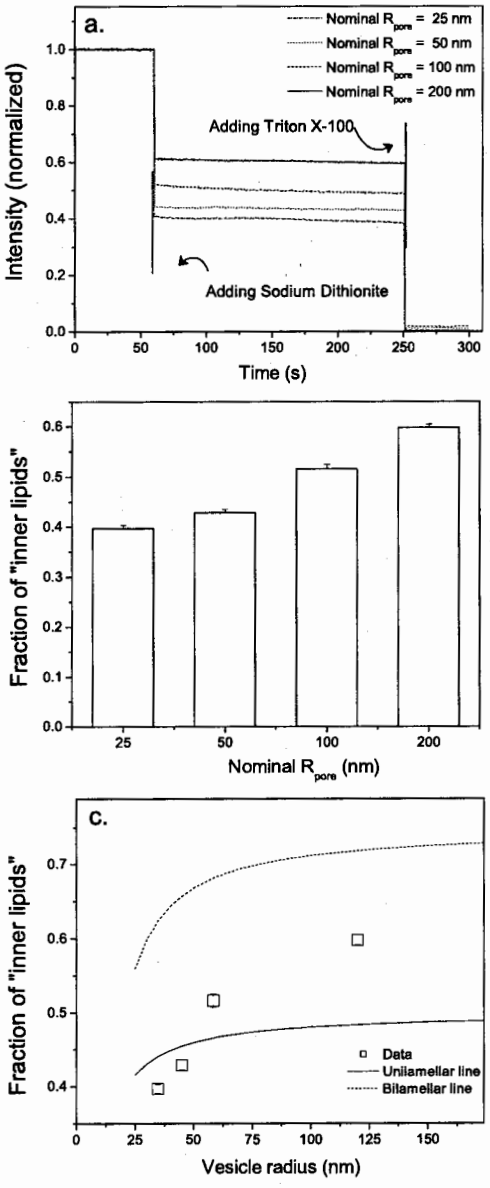

Figure 3.8: a. The intensity (normalized) of POPC:NBD-PC vesicles before and after introduction of sodium dithionite to quench the outer NBD-PC and Triton X-100 to lyse the vesicles, consequently quenching inner-NBD PC. b. Fraction of inner lipids calculated using Eq. 3.1. c. Fraction of inner lipids as a function of vesicle radius; the unilamellar and bilamellar lines are shown for comparison.

Triton X-100 for samples of vesicles extruded through PCTE membranes with nominal pore radii varying from 25 nm to 200 nm. Fraction of inner NBD-PC, representing the fraction of inner lipids, was calculated using Eq. 3.1 and is shown in Fig. 3.8.b. In Fig. 3.8.c the fraction of inner NBD-PC is plotted as a function of vesicle radius. The radii of vesicles are 34.8, 44.9, 58.8 and 120 nm for vesicles produced using 25 nm, 50 nm, 100 nm and 200 nm pores, respectively. These values are taken from the results shown in Fig. 3.5. The unilamellar and bilamellar lines are also included in Fig. 3.8.c.

The data for 25 nm and 50 nm vesicles, which is below the unilamellar line, indicates that these vesicles are unilamellar. However, it raises an issue of the cause of the data below the unilamellar line. This issue may be explained by two possible scenarios: the permeation of the sodium dithionite into the bilayer quenching inner lipids to some extent or the geometry of NBD-PC favors the lipid to be more probably located at the outer leaflet. It has been shown by other authors [60] that sodium dithionite permeates to some extent, when sonicated small vesicles were used, but not for large vesicles such as extruded vesicles used in these studies. Judging from the flat intensity during time course after the addition sodium dithionite and the fact that the measurements were taken directly after stirring the sample, the permeation of sodium dithionite may not be the case. The headgroup of PC is large so that it favors the outer leaflet of the bilayer. However, in NBD-PC, the NBD is attached to the acyl chains of the lipid and at some extent changing the geometry of the lipid molecule. There is no information available on whether NBD-PC favor the outer or inner leaflet of the bilayer. So, up to this point there is no clear explanation on why the the

data for 25 and 50 nm vesicles below the unilamellar line. Previous experiments studying the lamellarity of vesicles extruded through 25 and 50 nm pores using an NMR technique do not show the inner lipid fraction as low as what I find [47]. Further experiments using NMR technique may confirm the results in NBD-experiments.

The data for 100 nm and 200 nm vesicles, which are above the unilamellar line, indicate that these vesicles could contain a combination of unilamellar and multilamellar vesicles. Using Eq. 3.4, the fraction of unilamellar and bilamellar vesicles was calculated for 100 and 200 nm vesicles. There are 23 % and 50 % of the bilamellar vesicles (77 % and 50 % of unilamellar vesicles) for 100 and 200 nm vesicles, respectively. This is with the assumption that vesicles only have up to 2 bilayers.

Experiments were also done to observe the influence of the number of passes through the extruder on the lamellarity of the vesicles. Figure 3.9 shows the percentage of the inner lipids as a function of number of passes through extruder for vesicles produced using 25 nm, 50 nm, 100 nm and 200 nm pores. For small pores, vesicle lamellarity decreases with number of passes, while for large pores the lamellarity achieves the equilibrium at first two passes. This indicates that small pores are more effective in rupturing multilamellar vesicles than large pores. These results lead to the following possible scenario of vesicle rupture during extrusion. At the first pass through the extruder, the MLVs break up into smaller MLVs and LUVs when large and small pores were used, respectively. Since the size of the smaller MLVs is comparable to the size of the large pores, they can squeeze easily through the pores without rupturing at the second and subsequent passes. With the mean radii of 65 nm and

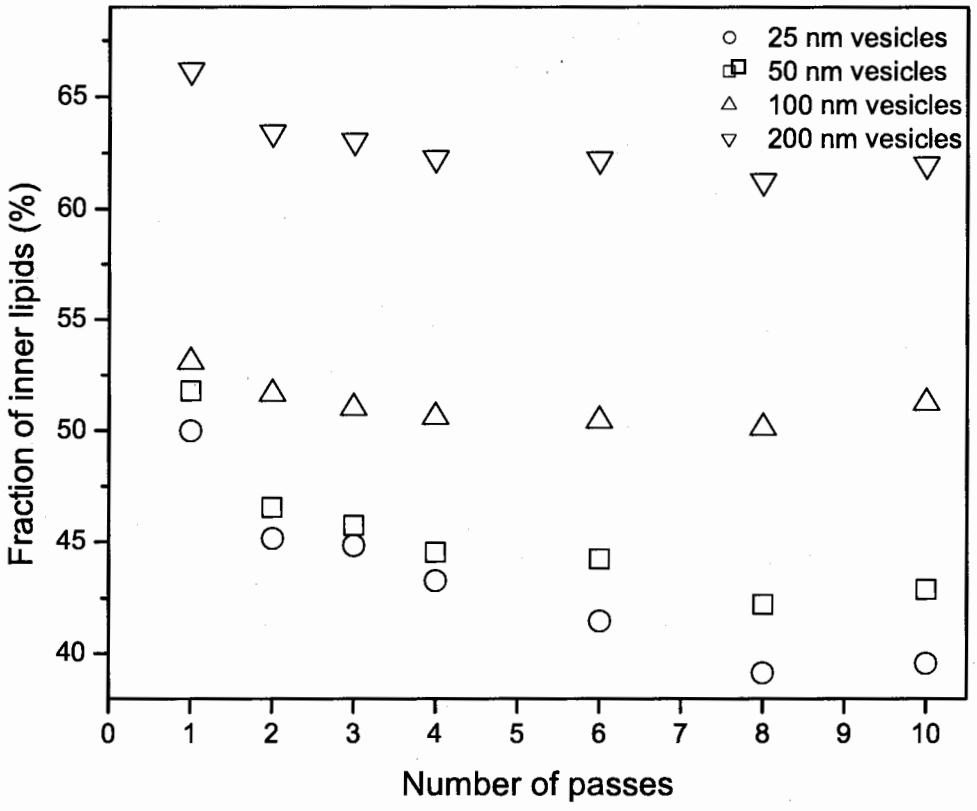

Figure 3.9: Fraction of inner lipids as a function of number of passes for vesicles produced using 25 nm, 50 nm, 100 nm and 200 nm pores.

155 nm for 100 nm and 200 nm pores, respectively, the smallest vesicles of approximately 11 nm [64], and the separation between the bilayers for multilamellar vesicles of 10 nm [47], the formation of multilamellar vesicles comparable to the size of 100 nm and 200 nm pores is possible. These multilamellar vesicles do not rupture when extruded through the pores.

3.4 Summary

The results of these studies show that, although the size of the extruded vesicles can vary depending on the size of the pores used, only small vesicles have narrow size distributions and are unilamellar. The polydispersity of the vesicles produced using larger pores is large, although the polydispersity of the pores is small. The polydispersity of the vesicles is most likely due to the presence of small vesicles that are produced spontaneously when the lipid was initially dispersed in water or, alternatively, as a consequence of the process of extrusion. On the other hand, the multilamellarity of extruded vesicles when produced using large pores is presumably due to the break-up of MLVs into smaller MLVs that are comparable to the size of the pores. The smaller MLVs then can squeeze easily through pores without further rupture.

Chapter 4

Effect of Sterols on the Mechanical Strength of Lipid Membranes

4.1 Introduction

In this chapter, I discuss the effect of sterols on the mechanical strength of lipid membranes. The strength of membranes was probed by measuring the lysis tension of vesicles made from mixtures of POPC and various sterols, including cholesterol, lanosterol and ergosterol. Extrusion methods used in determination of the lysis tension will be discussed and the results for the lysis tension will be compared to other membrane properties, including the lipid order parameter, the area expansion modulus and the bending rigidity determined from other studies.

Lipid molecules have a polar domain that is hydrophilic connected to a non-polar domain

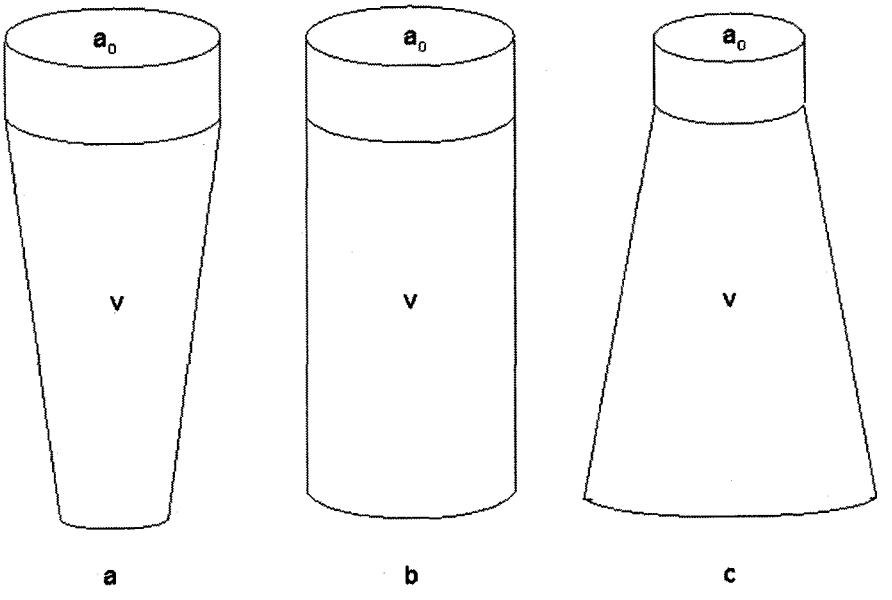

Figure 4.1: Shapes of lipid molecules : a. a truncated cone, b. a cylinder and c. an inverted cone. a_o is surface area occupied by a lipid molecule and v is volume of the hydrocarbon chain/chains.

that is hydrophobic. There is an enormous diversity of lipids, which vary in the composition of their polar and/or non-polar domains. It is the hydrophobic/hydrophilic nature of lipid molecules that causes them to associate into different structures when exposed to an aqueous environment, since by doing this the free energy of the system can be lowered. Exposing a hydrophobic molecule to water causes the rupture of hydrogen bonds between water molecules adjacent to the hydrophobic domain and the reorientation of the bonds, forming a hydrogen bonding network around the hydrophobic domain. This causes a restriction on the hydrogen bonding network, thus decreasing the entropy and increasing the free energy [65]. On the other hand, interaction between water molecules and hydrophilic headgroups decreases the free energy of the system. For these reasons, when a lipid is dispersed in water, the molecules will aggregate into structures that shield the hydrophobic tails and expose the hydrophilic headgroups to decrease the free energy of the system.

A variety of structures, such as micelles, bilayers or inverted micelles may be formed when lipid molecules are dispersed in an aqueous environment. The structures formed in each specific case are dictated by the geometry of the lipid molecules, which can be described as a truncated cone, a cylinder, or an inverted cone, as shown in Fig. 4.1. The structures formed depend on the value of volume of the hydrocarbon chains v, the surface area occupied by the lipid molecule a_o, and the maximum length of the hydrocarbon chain l_c through a shape factor defined as $\frac{v}{a_o l_c}$ [64, 66]. Lipids with shape factors less than $\frac{1}{3}$ and between $\frac{1}{3}$ and $\frac{1}{2}$ tend to aggregate into spherical micelles and cylindrical micelles, respectively. Lipids with shape factors between $\frac{1}{2}$ and 1 and greater than 1 tend to form bilayers and inverted

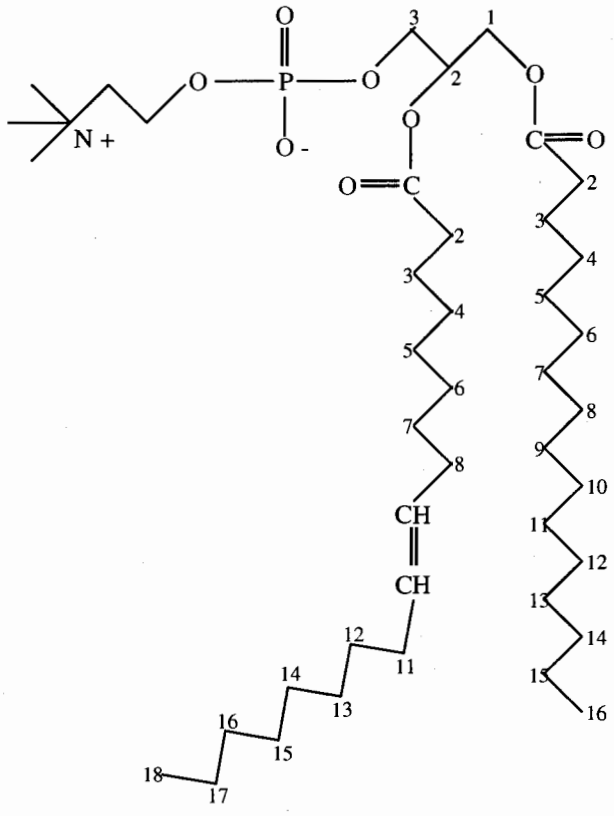

Figure 4.2: The molecular structure of POPC. The polar domain consists of a positively charged choline group attached to a negatively charged phosphate group and is neutral overall. The non-polar domain consists of two hydrocarbon chains : one is a 16 carbon fatty acid, known as palmitic acid, and the other is an 18 carbon fatty acid with one double bond between carbons 9 and 10, known as called oleic acid.

micelles, respectively.

As an example, Fig. 4.2 shows the molecular structure of POPC, the main lipid used in these studies. The polar domain consists of a positively charged choline group attached to a negatively charged phosphate group and is neutral overall. The non-polar domain consists of two hydrocarbon chains : one is a 16 carbon fatty acid, known as palmitic acid, and the other is an 18 carbon fatty acid with one double bond between carbons 9 and 10, known as oleic acid. Because of the presence of a double bond in one of its hydrocarbon chains, POPC is called a mono-unsaturated lipid. Lipids with no double bonds in their hydrocarbon chains are called saturated lipids. The POPC molecule favors the formation of bilayers when dispersed in water. Once the bilayer is formed, it tends to close up into a vesicle to prevent the exposure to water of hydrocarbon chains around the perimeter of the bilayer [67].

A bilayer has an area per molecule a which is set by forces originating from lipid-lipid and lipid-water interactions. The compressive force which tends to decrease a is the result of hydrophobic interactions. This force can be represented by an energy per molecule of the form γa, where γ is the surface tension of the water and lipid interface. This force is balanced by a steric repulsive force that tends to increase a, which is due mainly due to the interaction between hydrocarbon tails. The steric force is strong at short distance and falls off rapidly as a increases and can be represented by a potential of the form C/a, where C is a positive constant. The energy per molecule from these two terms can be written as [64],

$$E = \gamma a + C/a \quad . \tag{4.1}$$

E has a minimum at the value of a at equilibrium, a_o. C can be determined in terms of γ

and a_o by setting $dE/da = 0$. Equation 4.1 can then be expressed as,

$$E = 2\gamma a_o + \frac{\gamma}{a_o}(a - a_o)^2 \quad , \tag{4.2}$$

which is valid only when a is close to a_o.

Three properties of the membrane that are relevant to these studies and have been studied extensively are the area expansion (compressibility) modulus K_a, the lysis tension γ_{lysis} and the bending rigidity k_c. When tension or compression is applied to the bilayer at equilibrium, the area per molecule will deviate from the equilibrium value a_o. Fig. 4.3.a shows an area dilation under the influence of isotropic tension τ. The change in area Δa is characterized by an isothermal area expansion (compressibility) modulus K_a, defined as

$$K_a = \frac{\tau}{\alpha} \quad , \tag{4.3}$$

where α is the fractional change in membrane area equal to $\frac{\Delta a}{a_o}$ produced by an isotropic membrane tension τ.

If the tension applied is larger than the tension the bilayer can withstand while keeping the lipid molecules together, the vesicle will rupture. The tension require to rupture or lyse the vesicle is called the lysis tension γ_{lysis}. It is a measure of the mechanical strength of the bilayer. Vesicle bilayers typically rupture when Δa is in the range of 2 - 5 % [66].

In order to force a flat membrane into a curved shape, a stress associated with curvature must be applied. Fig. 4.3.b shows the change in membrane curvature due to the bending moment M (torque per unit length). This change in membrane curvature is characterized

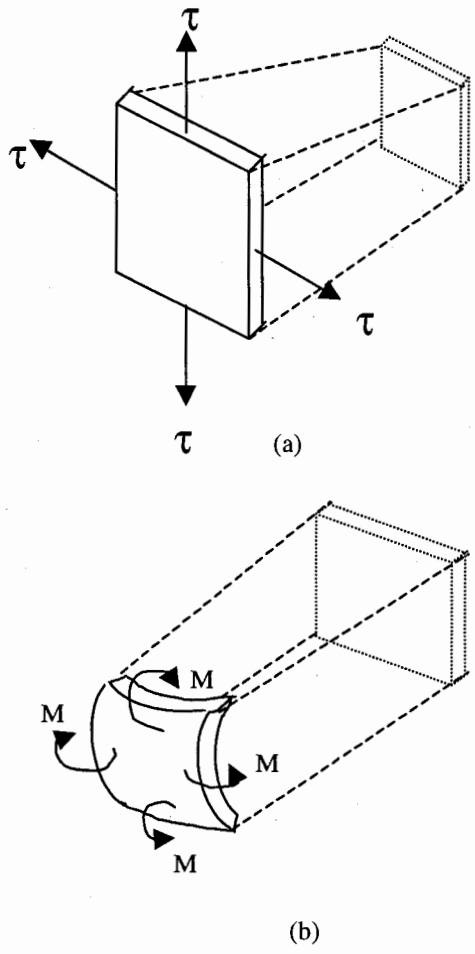

Figure 4.3: Membrane shape changes as a response to mechanical forces. a. Isotropic area dilation due to isotropic tension τ, b. bending or curvature change due to bending moment M.

by the bending rigidity k_c of a bilayer,

$$M = k_c \Delta c = k_c \left(\frac{1}{R_1} + \frac{1}{R_2} - c_0 \right) \quad , \tag{4.4}$$

where $\Delta c = c - c_0$ is the deviation of membrane curvature from its preffered value, c_0 is a parameter which represents spontaneous curvature a bilayer may have due to the compositional inhomogeneities in its two leaflets, and R_1 and R_2 are the principal radii of curvature at a given point on the membrane surface.

Studies show that K_a, γ_{lysis} and k_c are affected by the addition of sterols to the membrane. Most knowledge of the effect of sterols on these membrane properties comes from studies using cholesterol. For example, it has been shown that cholesterol increases the membrane lysis tension [3, 2], the area expansion modulus [68], and the bending rigidity [69, 70]. In addition, cholesterol also changes the phase behavior of membranes in a way that appears to be universal for membranes made from both saturated lipids such as DPPC [71] and mono-unsaturated lipids such as SEPC [72], PPetPC and POPC [73]. It induces acyl chain order, while breaking up the lateral packing of the lipid bilayer in the liquid crystalline state, consequently increasing lipid mobility within the bilayers. The more ordered acyl chains resemble a gel state, while increased lipid lateral mobility is associated with a liquid crystalline state. Cholesterol induces a new lipid state known as the liquid-ordered state, in which the lipids have a high conformational order and fast lateral diffusion [73]. Lipid membranes in this new state have the mechanical properties of the gel state and the lateral mobility of the liquid crystalline state. Both properties are important for the functioning of biological membranes.

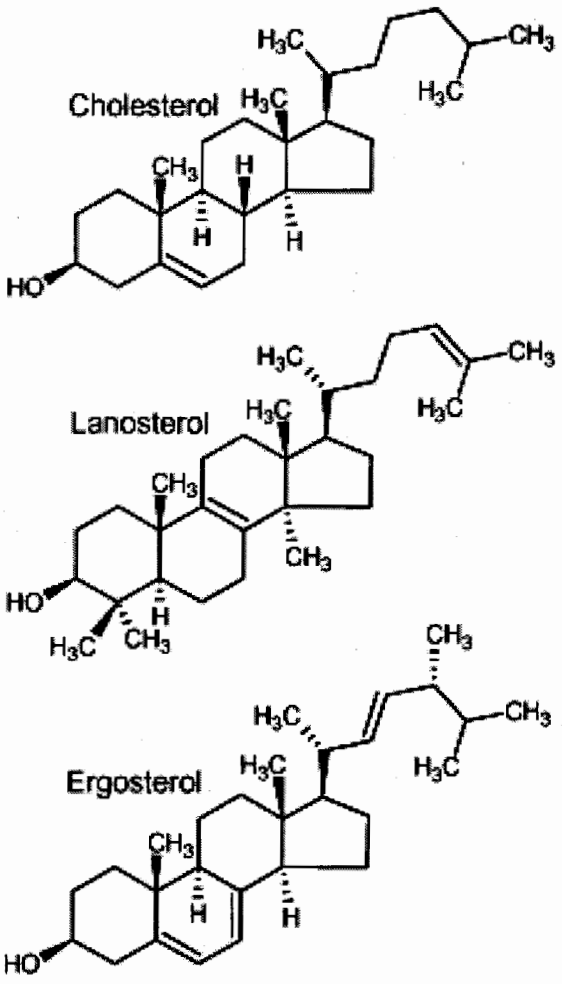

Figure 4.4: The molecular structure of cholesterol, lanosterol and ergosterol.

Cholesterol is the major sterol in plasma membranes of mammalian cells [4]. Other sterols of interest are lanosterol and ergosterol. Lanosterol predominates in some prokaryotic membranes, while ergosterol is abundant in plasma membranes of lower eukaryotes such as certain protozoa, yeast, fungi and insects such as Drosophila [5]. The molecular structures of cholesterol, lanosterol and ergosterol are shown in Fig. 4.4. The main structure of these sterols is quite similar. Cholesterol consists of a fused tetracyclic ring, a hydroxyl covalently attached to the first ring, and an extended hydrocarbon side chain attached to the fourth ring. Lanosterol differs from cholesterol as it has three additional methyl groups and a double bond on its side chain. On the other hand, ergosterol differs from cholesterol by a methyl group on its side chain and two extra double bonds, one on its side chain and the other on the second ring.

In recent years, the effect of lanosterol and ergosterol in comparison to cholesterol on lipid membranes has become the focus of many studies [74, 75, 76, 77, 78, 79, 80]. These studies show that the effect of these sterols on the properties of membranes is different depending on whether the membranes are composed of saturated or unsaturated lipids.

Ergosterol has been shown to be more effective than cholesterol in inducing acyl chain ordering in membranes composed of DPPC, a saturated lipid [78]. Lanosterol, on the other hand, is less effective than cholesterol in inducing acyl chain order of membranes composed of DMPC, also a saturated lipid [76]. In DPPC membranes with 40 mol % sterols, all sterols increase the area expansion modulus K_a, with ergosterol showing the largest effect followed by cholesterol and lanosterol [74]. The same studies also show limited change in the lysis

tension of the membranes with the introduction of sterols.

On the other hand, cholesterol has been shown to be the most influential followed by lanosterol and ergosterol in inducing acyl chain ordering in membranes composed of POPC, an unsaturated lipid [80]. The same studies show that the area expansion modulus K_a and the bending rigidity k_c increase with the introduction of sterols, with cholesterol producing the most significant increase in both values, followed by lanosterol and ergosterol [77, 80].

Measurements of the lysis tension of lipid membranes as a function of lanosterol and ergosterol content, however, is lacking, especially for unsaturated lipid membranes. This is in spite of the fact that this property of the membranes is important both in cells and in vesicle application as carriers. It is important for cell viability, which depends on maintaining an intact plasma membrane. In the application of the vesicles as carriers in drug delivery, for example, it is important that vesicles be resistant to stress induced by lytic agents in the host.

In this chapter, I describe experiments designed to observe the effect of cholesterol, lanosterol and ergosterol on the lysis tension of lipid vesicles. Preparation of vesicles used in lysis tension determination will be described and the extrusion methods used to determine the lysis tension of vesicles will be discussed. The results for the lysis tension will be compared to other membrane properties, including the lipid order parameter, the area expansion modulus and the bending rigidity determined from other studies to see the relationship between these membrane properties as sterols are introduced.

4.2 Materials and Methods

4.2.1 Vesicle Preparation

Materials used in these experiments were POPC, cholesterol, ergosterol and lanosterol. POPC and cholesterol (98% purity) were purchased from Avanti Polar Lipids, Inc., while ergostrol (98% purity) and lanosterol (97% purity) were purchased from Sigma-Aldrich Co.

Samples of POPC:sterols were prepared by mixing POPC and each sterol in powder form at the required concentrations. The mixed powder was then dissolved in a benzene:methanol mixture (4:1). The solution was gently shaken until all powder disappeared. The solution was lyopholized, i.e., it was frozen in liquid nitrogen and then evaporated under vacuum for about 6 hours. After lyophilization, the powder was hydrated using purified water from a Milli-Q water purification system (Millipore, Bedford MA) in the ratio of 1 mg of lipid per 1 ml of water. The dispersions were then taken through a freeze-thaw-vortex process before being extruded through 200 nm pores (pre-extrusion). The pre-extruded vesicles then were diluted to a concentration of 0.1 mg/ml and were used for experiments to determine lysis tension.

4.2.2 Lysis Tension Determination

Determination of the lysis tension of vesicles follows methods explained previously [3]. The lysis tension is related to the minimum pressure required to burst or lyse a vesicle at the entrance of a pore. Figure 4.5 shows a diagram of a vesicle at the entrance of a pore. R_p and R_v are the radii of pore and vesicle, respectively, while P_1 is the applied pressure, P_2

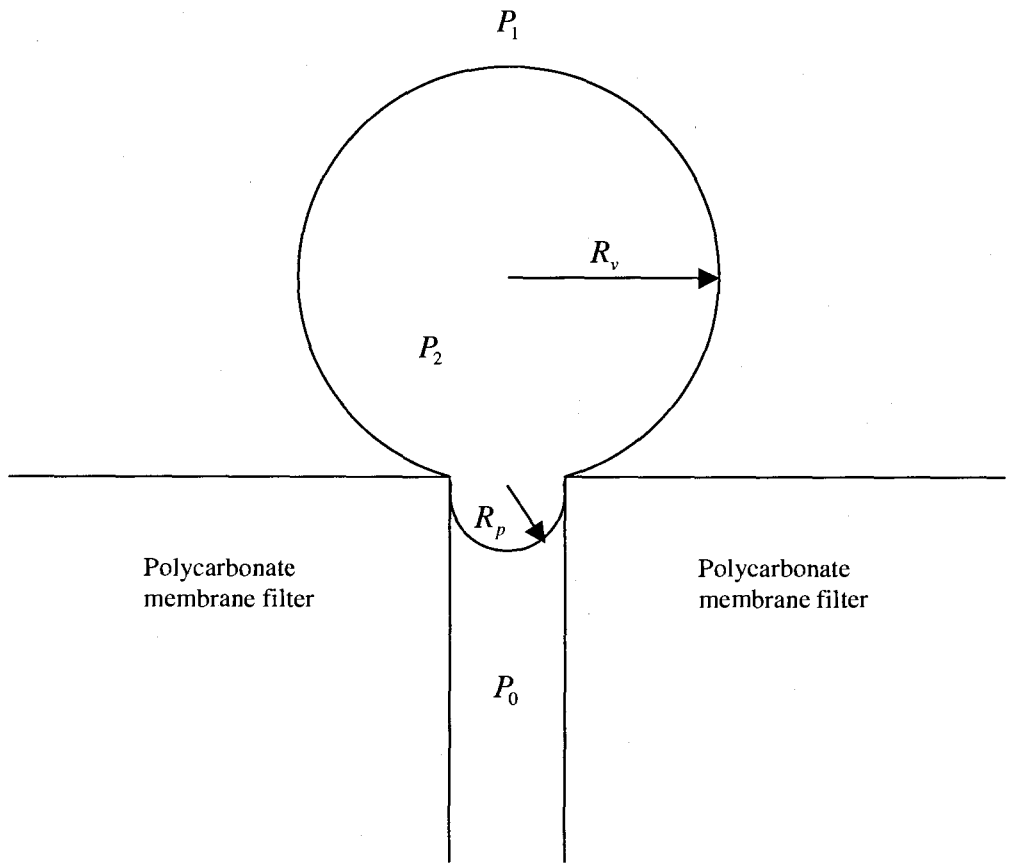

Figure 4.5: Schematic diagram of a vesicle at the entrance of a pore. Symbols are defined in the text.

is the pressure inside the vesicle and P_0 is atmospheric pressure. To enter the pore, a large vesicle must reduce its volume by bursting. As a large vesicle of radius R_v is pulled into a pore of radius R_p, a surface tension γ is induced in the membrane. The vesicle bursts when the induced surface tension is greater then the lysis tension of the bilayer. A relation between applied pressure P, γ, R_p and R_v can be derived by applying the Laplace relation between pressure and curvature $P = 2\gamma H$ [81], where H and γ are the mean curvature and surface tension, respectively, to small and large fragments of vesicles in Fig. 4.5. The Laplace pressure for the large fragment is given by,

$$P_2 - P_1 = \frac{2\gamma}{R_v} \quad , \tag{4.5}$$

and for the small fragment is given by,

$$P_2 - P_0 = \frac{2\gamma}{R_p} \quad . \tag{4.6}$$

Substracting Eq. 4.5 from Eq. 4.6 yields

$$P = 2\gamma(\frac{1}{R_p} - \frac{1}{R_v}) \quad , \tag{4.7}$$

where the pressure difference $P = P_1 - P_0$. The lysis tension γ_{lysis} can be calculated when the minimum pressure required to rupture the vesicles and the radii of the pores and of the vesicles are available.

The radii of the pores and the vesicles were determined using SEM and DLS, respectively. The details of DLS and SEM measurements have been described in Chapters 2 and 3, respectively.

The minimum pressure was determined from measurements of the flowrate of the vesicle dispersion through the pores of the PCTE membrane. When vesicle suspensions are pushed through pores with a pressure larger than P_{min}, the flowrate of the suspension is proportional to the pressure applied following Darcy's law for flow through N_p cylindrical tubes,

$$Q = \frac{N_p \pi R_p^4 (P - P_{min})}{8\eta L} \quad , \tag{4.8}$$

where η is the viscosity of the solvent, R_p and L are the mean radius and the length of the cylindrical pores, respectively. Applying pressures smaller than P_{min} results in no flow of suspension through the pores. In this case, the pressure is not enough to cause a tension sufficient to rupture the vesicles. The vesicles then just block the pores. The minimum pressure, then, can be defined as a pressure at and below which the flowrate of the vesicle suspension is zero. Since the flowrate is proportional to the pressure, the minimum pressure can be determined by measuring the flowrate at several different pressures and fitting a line to the flowrate pressure data to extrapolate to zero flowrate pressure.

The flowrate of the suspension was measured by accumulating solution for a certain interval time and weighing the solution. This was achieved using a flowmeter. In the flowmeter, a three-branch valve is coupled to a stopwatch, where one of the three branches is connected to the exit tube from the extruder. The other two branches are directed into two graduated cylinders. Under normal operation, one of these two branches is open, while the other is closed. Initial conditions involve flow of solution through one branch directed into the first cylinder. When the start button is pushed, the stopwatch starts to count and the flow is switched to the other branch entering the second cylinder, which is initially

empty. When the stop button is pushed, the stopwatch stops the count and the flow goes back to the initial conditions. The solution in the second cylinder is then weighed and the flowrate is calculated.

4.3 Results and Discussions

Lysis tensions of vesicles made from mixtures of POPC:cholesterol, POPC:lanosterol, and POPC:ergosterol were determined. Equation 4.7 was used for lysis tension calculation, with γ and P replaced by γ_{lysis} and P_{min}, respectively,

$$\gamma_{lysis} = \frac{P_{min}}{2}\left(\frac{R_p\, R_v}{R_v - R_p}\right) \quad . \tag{4.9}$$

In order to calculate the lysis tension of vesicles, the radii of the pre-extruded vesicles R_v and the pores R_p, and the minimum pressure required to rupture vesicles P_{min} need to be measured.

The radius of pre-extruded vesicles was measured using DLS. Equation 2.25 was fit to the autocorrelation function data and Eq. 2.29 was used for the field-field autocorrelation function. Pre-extruded vesicles are quite polydisperse, but a mean can be determined from the fits. The results from samples of POPC, POPC:cholesteol, POPC:lanosterol and POPC:ergosterol with different concentrations of sterols are summarized in Table 4.1.

The radius of the pores was measured using SEM. There are 471 pores analyzed from SEM micrographs. Figure 4.6.a shows a typical micrograph of the surface. The radius data was displayed in a histogram and a Gaussian distribution was fit to the data to determine the mean radius of the pores. Figure 4.6.b shows the histogram and the Gaussian fit. The

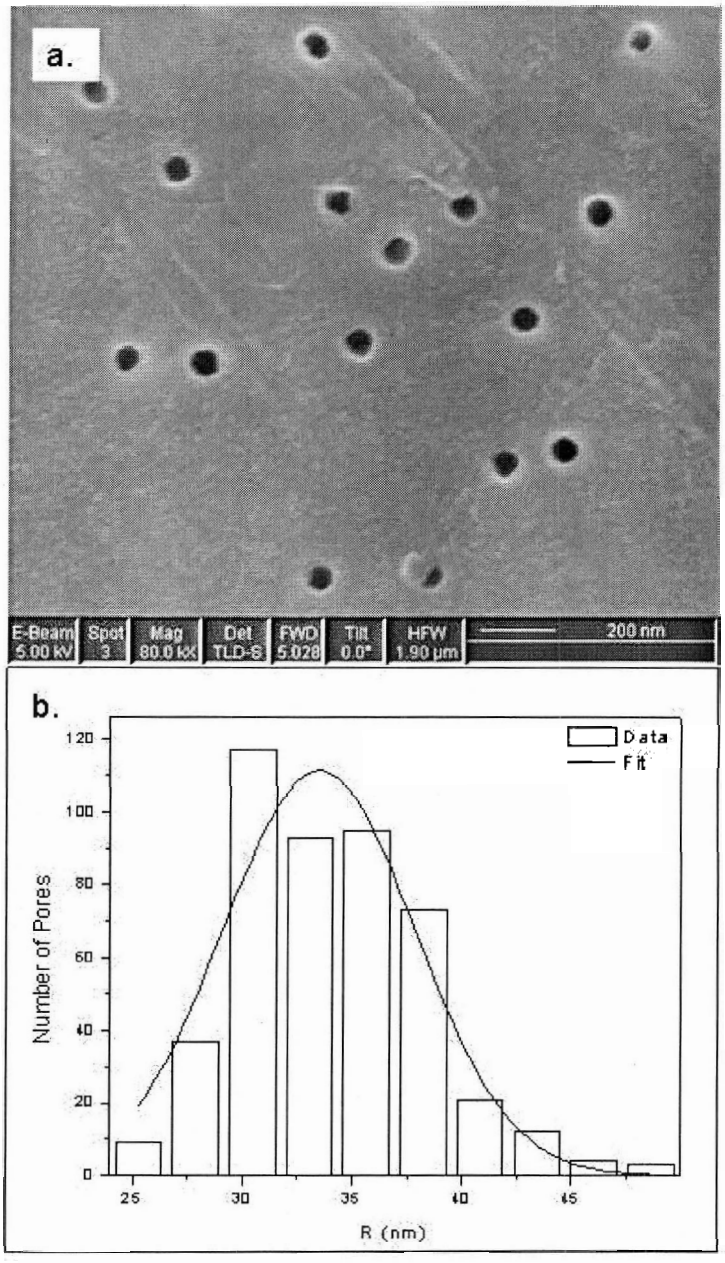

Figure 4.6: a. Typical SEM micograph of pores in a 50 nm PCTE membrane and b. the histogram data of the pore radii from SEM measurements.

Sterol	% Sterol	Mean Radius (nm)
	0	195 ± 1.3
Cholesterol	10	193 ± 1.2
	20	211 ± 2.0
	30	226 ± 1.6
Lanosterol	10	215 ± 1.5
	20	187 ± 1.5
	30	157 ± 1.7
Ergosterol	10	228 ± 2.8
	20	199 ± 2.2
	30	177 ± 0.7

Table 4.1: The mean radius of pre-extruded vesicles. The uncertainties represent the standard deviations from 5 measurements.

Sterol	% Sterol	P_{min} (psi)
	0	56.2 ± 5
Cholesterol	10	69.3 ± 3.6
	20	78.5 ± 5.3
	30	88.0 ± 4.9
Lanosterol	10	67.1 ± 2.9
	20	71.7 ± 2.9
	30	76.0 ± 4.1
Ergosterol	10	63.4 ± 2.0
	20	67.3 ± 6.2
	30	67.3 ± 6.3

Table 4.2: The minimum pressure for extrusion of vesicle solution through PCTE membranes. The values are for vesicles made from the mixtures of POPC:sterols and were determined from linear fits to the data as shown in Fig.4.7.

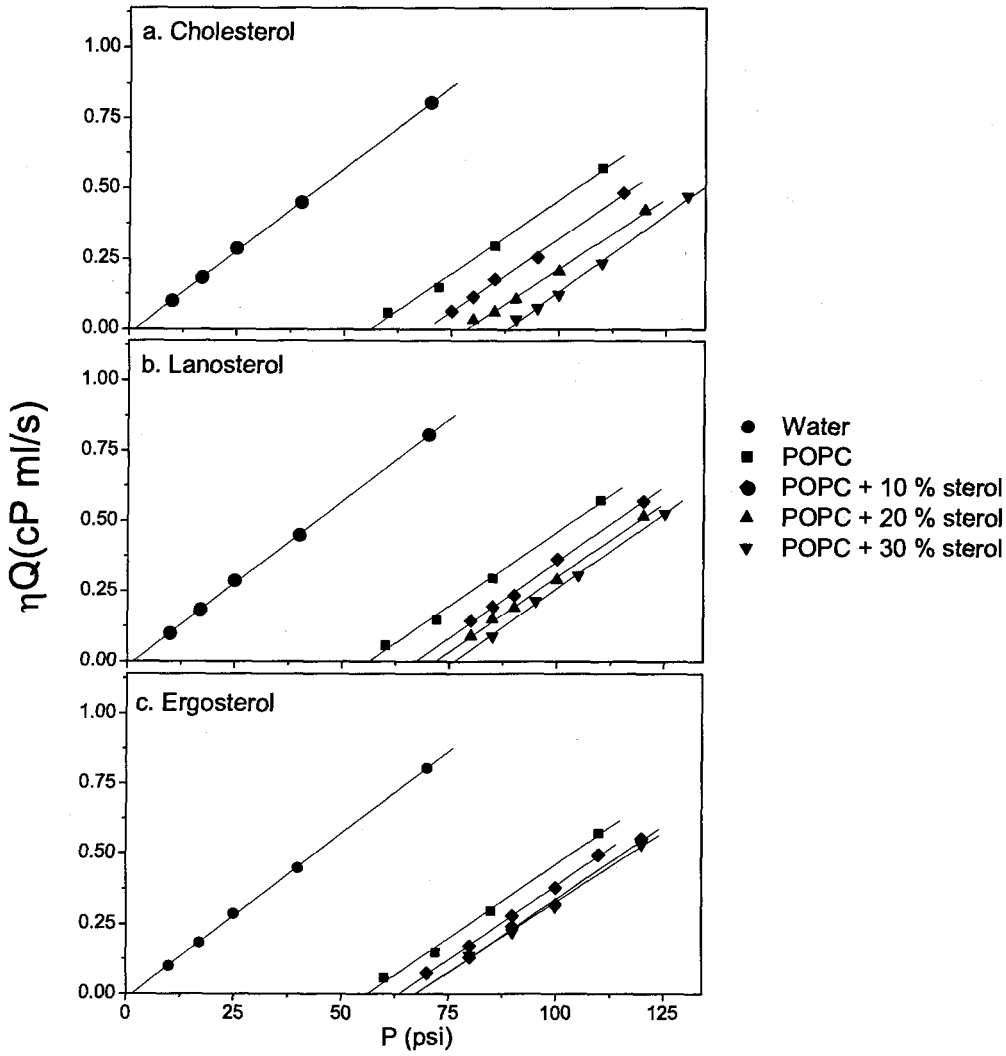

Figure 4.7: The product of the solvent viscosity and the flowrate ηQ as a function of pressure for POPC:sterol with the concentration of sterols varying from 10 to 30 mol %. A linear function was fit to the data to determine the zero flowrate pressure defined as the minimum pressure P_{min}. The data for water is shown for comparison. The lines are the linear fits.

mean radius resulting from the fits is 33.5 ± 0.5 nm.

The minimum pressure P_{min} for each sample was determined from the flowrate measurements of vesicle suspension at different pressures and the product of the solvent viscosity and the flowrate ηQ is plotted as a function of pressure. The data and the linear fits are shown in Fig. 4.7 and the results for P_{min} and the uncertainty of P_{min} from the fit are summarized in Table 4.2.

The lysis tension of POPC vesicles with different concentrations of sterols was then calculated using Eq. 4.9. The results are shown in Fig. 4.8. The figure shows that all sterols increase the lysis tension of POPC membranes, with cholesterol showing the largest effect, followed by lanosterol and ergosterol. The increase in lysis tension as a function of sterol concentration is almost linear for all sterols. The lines in the graphs are linear fit through the data of pure POPC vesicles.

The increase in lysis tension of POPC membranes due to the incorporation of cholesterol is consistent with results from previous studies on POPC [3] and other unsaturated lipids such as SOPC [2]. However, there is less information for the lysis tension of unsaturated lipid membranes in the presence of lanosterol and ergosterol. Nevertheless, there are results on the effect of cholesterol, lanosterol and ergosterol on other properties of POPC membranes, including the order parameter measured by the first moment of ^{2}H-NMR spectra M_1, the bending rigidity k_c and the area expansion modulus K_a [77, 80]. Sterols increase the order parameter M_1, the bending rigidity k_c and the area expansion modulus K_a of POPC membranes following the sequence cholesterol > lanosterol > ergosterol [77, 80] (For

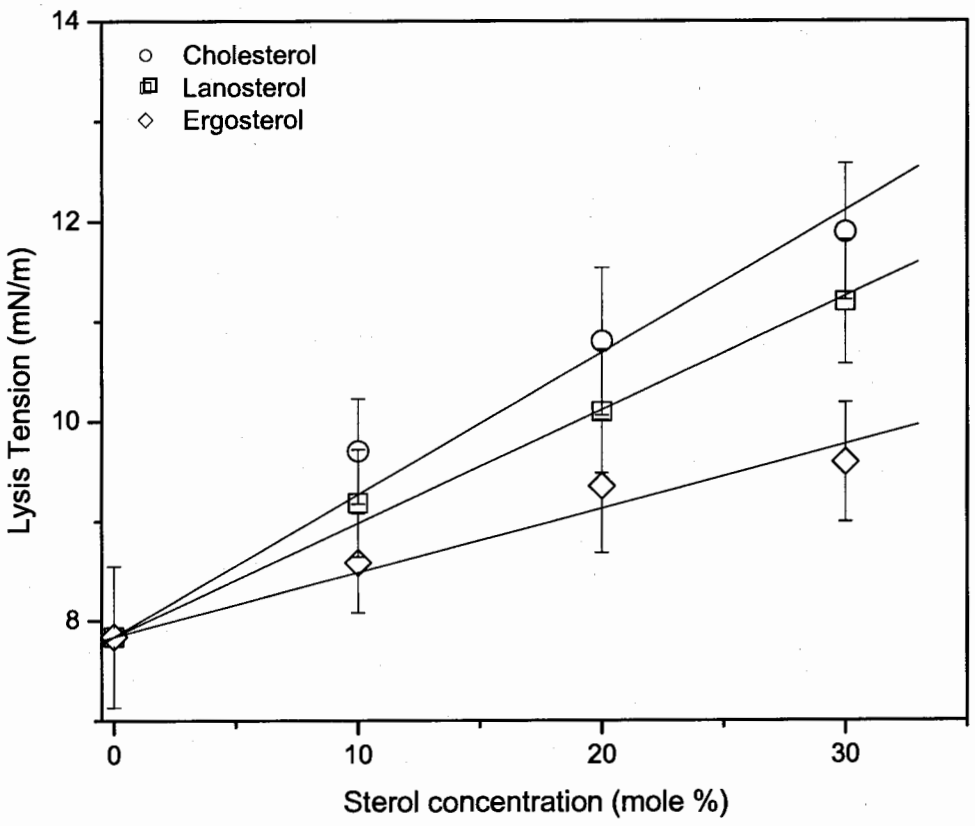

Figure 4.8: The lysis tension of POPC vesicles as a function of sterol concentration. The lines are linear fits through the value of the lysis tension of POPC vesicles.

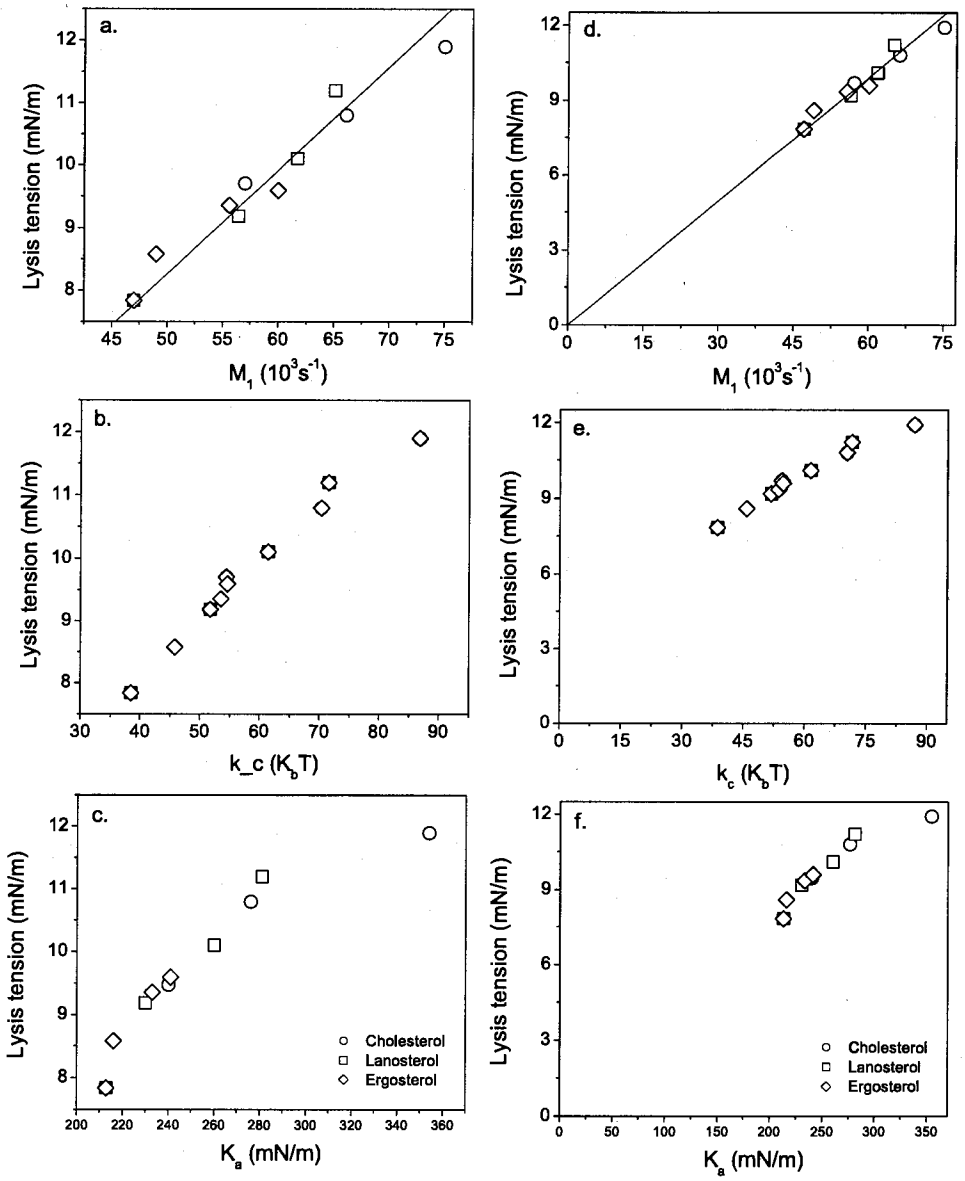

Figure 4.9: The lysis tension γ_{lysis} of POPC:sterol membranes as a function of a. the order parameter M_1, b. bending rigidity k_c, and c. the area expansion modulus K_a. Values of M_1, k_c and K_a are taken from Table 1 of ref. [80]. In d,e and f, the data is shown respecting to point zero

simplicity, I have used the order order parameter to describe M_1). This data is correlated to the increase in the lysis tension that also follows the sequence cholesterol > lanosterol > ergosterol. The correlation between lysis tension γ_{lysis} of POPC membranes from these studies with order parameter M_1, bending rigidity k_c and area expansion modulus K_a of POPC membrane can be shown by plotting γ_{lysis} as a function of M_1, k_c and K_a. Figure 4.9 show the plot of γ_{lysis} as a function of M_1, k_c and K_a, where values of M_1, k_c and K_a are taken from Table 1 of Ref. [80]. The data for different mixtures collapse to a universal curve for all graphs.

The M_1, k_c and K_a for POPC:ergosterol saturates after 20 % ergosterol [80]. However, for the lysis tension, as shown from these studies, it cannot be concluded, since the error bar is quite large.

The relation between lysis tension and order parameter shown in Fig. 4.9.a is linear and data from all samples collapse to a single curve. This indicates that lipid chain order and membrane mechanical strength are related. Since the increase in the chain order is attributed to an increase in the membrane thickness [82], the linear relation between lysis tension and the order parameter suggests that lysis tension is also related to the hydrophobic thickness of the membranes. This is reasonable because, in the process of membrane rupture, there is competition between the applied tension that forms pores and the edge energy associated with the pore formation [83]. The increase in the thickness of the membrane as a consequence of the presence of sterols should make pore formation more difficult because of increased edge energy.

There is a relation between the lysis tension and the the bending rigidity as well as the lysis tension and the area expansion modulus, as shown by the collapse of the data to a singe curve. However these relations are not linear.

4.4 Summary

These studies show that cholesterol, lanosterol and ergosterol increase the mechanical strength of POPC membranes as indicated by an increase in the membrane lysis tension. Despite their similarity in molecular structure these sterols impact the lysis tension of the lipid membrane to a varying extent. Cholesterol exhibits the largest effect followed by lanosterol and ergosterol. The lysis tension of POPC membranes increases almost linearly as a function of sterol content for cholesterol and lanosterol up to 30 mol % sterols. However, the lysis tension saturates after 20 mol % for POPC:ergosterol system. The increase in the lysis tension of POPC membranes by sterols is correlated to the increase in the chain order of the lipids by sterols.

Chapter 5

Vesicle Aggregation Induced by cytidine 5'-triphosphate : phosphocholine cytidylyltransferase

5.1 Introduction

In this Chapter, I describe the interaction between CCT and lipid membranes, which is studied by observing vesicle aggregation induced by CCT. The effect of CCT on the aggregation of vesicles composed of activating and non-activating lipids will be compared. The effect of CCT on the aggregation of class I and class II lipid vesicles will be discussed and

factors influencing vesicle aggregation will be proposed.

Cytidine 5'-triphosphate(CTP):phosphocholine cytidylyltransferase (CCT) is a key regulatory enzyme in the synthesis of phosphatidylcholine (PC). It catalyzes the formation of cytidine 5'-diphosphate choline, the head-group donor used in the synthesis of PC. This enzyme is amphitropic : it interconverts between a soluble form where it is inactive and a membrane-bound form where it is active. The equilibrium between soluble and membrane-bound forms is determined by the lipid composition of the membrane and by the phosphorylation state of the enzyme. A membrane containing anionic lipids, for example, stabilizes the active membrane-bound form of the enzyme [8, 9, 10], while phosphorylation on the enzyme favors its inactive soluble form [8]. PC production catalyzed by CCT is important because it compensates for the degradation of PC due to the action of phospholipases, enzymes that catalyze the hydrolysis of phospholipid. When inactive CCT senses a decrease in the amount of PC in a membrane, it will bind to the deficient PC membranes and become active [7]. Studies show that CCT responds quickly to PC catabolism [84, 85, 86]. In some cells, CCT is distributed in the nucleus where it is inactive or less active and in the endoplasmic reticulum (ER) where it is active [87, 88]. The distribution of CCT between the nucleus and the ER changes in response to the stimulation for PC synthesis.

CCT has a dimeric structure [6]. Each monomer consists of 367 residues that can be classified into four functional domains : domains N, C, M and P, as shown in Fig. 1.1.a. Domain N (residues 1-72) contains a cluster of positively charged amino acids [89]. The catalytic domain, domain C (residues 73-236) [90], together with domain N, is involved in the

dimerization [91]. The membrane binding domain, domain M (residues 237-300), contains three consecutive repetitions of 11 residues (residues 256-288) that form a random coil in the absence of lipid vesicles and an amphipathic α helix in the presence of anionic lipid vesicles [92]. Domain P (residues 301-367) is rich in serine-proline and is highly phosphorylated [93].

CCT binds to and becomes activated by membranes containing anionic lipids [8, 9, 10], dioleylglycerols (DOG) and phosphatidylethanolamines (PE) [11, 12, 13]. These activating lipids can be categorized into two classes. For membranes made up of anionic lipids, the binding of CCT to the membrane occurs by electrostatic interaction between the positively charged binding domain (domain M) of CCT and the negatively charged surface of the membrane followed by hydrophobic insertion of domain M [9, 10, 14]. These lipids are known as class I lipids. For membranes composed of DOG and PE, the binding of CCT is postulated to occur because CCT relieves the negative curvature strain which exists in these membranes [12, 13]. These lipids are known as class II lipids. Long chain fatty acids, which are both charged and induce negative curvature strain, also promote binding and activation of CCT. CCT binds poorly to and shows very weak activity in membranes containing Egg PC [8, 94, 95]. Egg PC, therefore, is often categorized as a non-activating lipid.

Experiments on anionic lipid membranes show that there are two steps for CCT activation : electrostatic binding to the membrane and intercalation of the domain M into the hydrophobic area of the membrane [14]. Although CCT binds to membranes in both liquid crystalline and gel phases, it is active only in a liquid-crystalline phase membrane. This suggests that an additional interaction other than binding, which can be achieved only

in liquid crystalline phase membrane, is required for CCT activation. These results have led to a model of activation, in which domain M is the inhibitor of the catalytic domain. This inhibition is relieved when domain M intercalates into the hydrophobic region of the membrane [7]. This model is supported by the finding that CCT activity is proportional to the amount of activating lipids present, while the fragment of CCT that lacks the membrane binding domain, CCT-236 is always active independent of lipid concentration [96].

The binding affinity and the activity of CCT depend on the lipid composition of the membrane. The binding affinity for class I lipids is larger than that for fatty acids or class II lipids by up to a factor of ten [8, 9, 12, 13]. Class I lipids are also more potent than class II lipids and long chain fatty acids in activating CCT [9, 95]. This suggests that CCT-membrane binding affinity and CCT activity are correlated.

The binding of CCT to the membrane of a single vesicle is thought to occur by binding of both domain Ms of the CCT dimer, as shown in Fig. 1.1a. However, it is also possible that each domain M can bind to the surface of different vesicles, cross bridging the two vesicles, as shown in Fig. 1.1b. The cross-bridging mode will result in the aggregation of vesicles. It has been observed that addition of CCT to small unilamellar anionic vesicles increases the turbidity of the samples, suggesting the occurrence of aggregation [15].

This chapter contains studies on the effect of CCT on the size distribution of large unilamellar vesicles. The effect of CCT on vesicles made from activating and non-activating lipids will be compared. The effect of CCT on the aggregation of vesicles made from class I and class II lipids will be discussed. Factors affecting aggregation of vesicles will be proposed.

5.2 Materials and Methods

5.2.1 Materials

The lipids used in these experiments were L-α Phosphatidylcholine (Egg PC), L-α Phosphatidylglycerol (Egg PG), 1,2-Dioleoyl-*sn*-Glycero-3-Phosphoethanolamine (DOPE), 1-Palmitoyl-2-Oleoyl-*sn*-Glycero-3-Phospho-L-Serine (POPS) and oleic acid (OA). Egg PC and Egg PG were purchased from Northern Lipids Inc. (Vancouver, BC), OA from Sigma, while DOPE and POPS were purchased from Avanti Polar Lipids Inc. (Alabaster, AL). Rat liver CCTα and CCTα236 (encoding amino acids 1-236) were expressed by baculovirus infection of *Trichoplusia ni* cells and were purified as described previously [15]. The pure enzymes were stored in aliquots at -80° C and their concentrations were determined by quantitative amino acid analysis (Alberta Peptide Institute, Edmonton, AB). A 57-mer peptide (residues 237-293 of rat liver CCTα) was synthesized by K. Piotrowska at the University of British Columbia Peptide Service Laboratory (Vancouver, BC) as described previously [15]. The CCTα, CCTα236 and peptide were prepared by Dr. Joanne Johnson from Prof. Rosemary Cornell's Lab (Dept. of Molecular Biology and Biochemistry SFU).

5.2.2 Vesicle Preparation

Lipids in powder form were dissolved in chloroform. Aliquots of lipid or lipid mixture solutions were put in a round bottom flask before drying by rotary evaporation. The dried lipid films were then placed under vacuum overnight to remove traces of residual solvent.

The lipid films were dispersed in a buffer (10 mM Tris, pH 7.4, 1 mM ethylen-diaminetetra-acetic acid (EDTA), 150 mM NaCl, and 10 mM dithiothreitol (DTT)) to a concentration of 4 mM. The suspension was taken through a freeze-thaw-vortex process, as explained in the previous chapters. The lipid suspension was then diluted to a concentration of 0.1 mM and extruded through 2 polycarbonate membrane filters with a nominal pore radius of 25 nm held in an extruder (Lipex Biomembrane, Vancouver BC). The extrusion was repeated 14 times at a pressure of 200 psi.

5.2.3 Vesicle Size Measurements

The mean radius and the polydispersity of the vesicles/vesicle aggregation before and after introduction of CCT were measured using DLS. For vesicles, the mean radius is represented by the hydrodynamic radius, since it can be assumed as having spherical shapes. However, the vesicle aggregations are not spheres, so it is not the hydrodynamic radius which is measured. The mean radius of the vesicles aggregation in the following discussion then means the effective radius, the radius of particles which are not spheres, but is approximated as spheres.

The autocorrelation function measurement was repeated 5 times at a scattering angle of 90°. Equation 2.25 was fit to the intensity-intensity autocorrelation function using Eq. 2.40 for the field-field autocorrelation function. The intensity-weighted mean radius $\overline{R_i}$ and polydispersity σ_{R_i} were determined from the fitting procedure. The intensity-weighted distribution was determined instead of the number-weighted distribution because the aggregated structures within the samples are very polydisperse. As explained in Chapter 2,

the use of number-weighted distributions for polydisperse samples is limited. In addition, the form factor of the vesicle aggregation is not known, because the shape of vesicle aggregation is unclear. The use of intensity-weighted distribution is, however, still acceptable for the purpose of these studies as it allows the observation of the change of vesicle radius and polydispersity. The radius distribution is assumed to follow a Schulz distribution as described by Eq. 2.52. As explained previously, the Schulz distribution is asymmetric and skews to the large size of the distribution, which is appropriate for vesicle aggregations.

For DLS samples, CCT from 5.5 μM stock solution was introduced to a 0.1 mM vesicle suspension to produce CCT concentration in the range of 1-100 nM. The ratio of CCT to vesicles was determined from the concentration of CCT, the concentration of lipids and the number of lipid molecules per vesicle. The number of lipid molecules per vesicle was determined using an average vesicle radius as determined from these experiments, a bilayer thickness of 4 nm [97], and a headgroup area of 0.68 nm^2 for Egg PG, Egg PC and POPS [98] and 0.28 nm^2 for OA [99]. The lipid concentration was determined by the method of Bartlett [100].

To confirm the results from DLS measurements, negatively stained transmission electron microscopy (TEM) was conducted on some samples. 8 μL samples of vesicle solution with and without CCT were pipetted onto copper formfar coated grids (300 mesh). After removing the excess material by blotting with filter paper, the specimen grid was stained with 8 μL of 2 % aqueous uranyl acetate for a few seconds. The excess stain was then

removed by filter paper. The micrographs were taken from at least 2 grids for each sample. The microscope used was a Hitachi H-760 transmission electron microscope (Hitachi, Tokyo, Japan) located at the Bio-imaging facility, The University of British Columbia. The measurements were conducted by Dr. Svetla Taneva from Prof. Rosemary Cornell's Lab (Dept. of Molecular Biology and Biochemistry SFU).

5.3 Results

5.3.1 Effect of CCT on Activating and Non-Activating Lipid Vesicles

The effect of CCT on the aggregation state of activating and non-activating lipid vesicles was studied by observing the change in their size and polydispersity using DLS before and after introduction of CCT. Egg PG and Egg PC were chosen for activating and non-activating lipids, respectively, as Egg PG membranes are very strong activators of CCT, while Egg PC membranes are very weak activators of CCT.

Figures 5.1.a and b show intensity-intensity autocorrelation function data for vesicles made from Egg PC and Egg PG, respectively, before and after introduction of CCT. There is no difference in the decay time of the intensity-intensity autocorrelation function when CCT was introduced to Egg PC vesicles, although the ratio of CCT per vesicle was as high as 42. In contrast, an increase in the decay time is observed when CCT was introduced to Egg PG vesicles with a ratio as small as 1 CCT per vesicle. As explained in Chapter 2, DLS distinguishes small and large particles through the decay time of the intensity-intensity autocorrelation function : the larger the particles, the longer the decay time. These results

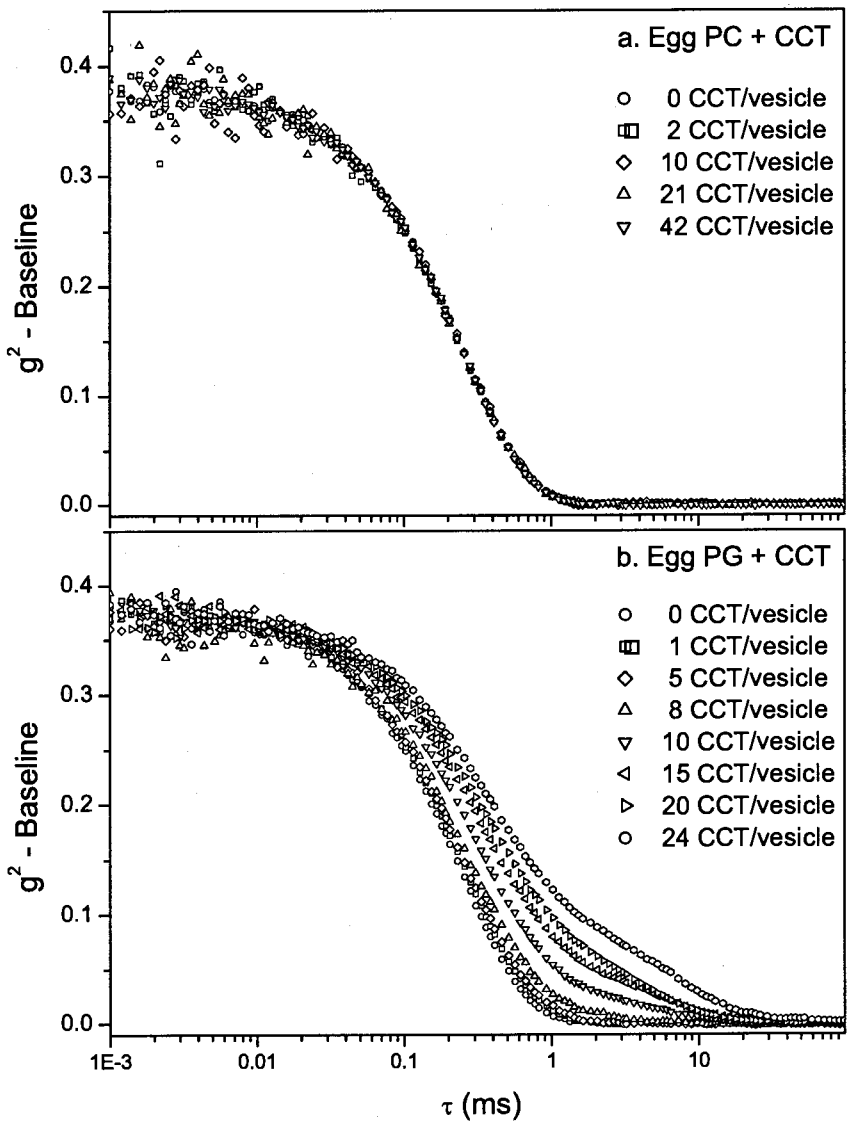

Figure 5.1: Intensity-intensity autocorrelation function data from DLS measurements of vesicles made from a. Egg PC and b. Egg PG before and after introduction of CCT protein.

suggest that CCT protein induces aggregation of Egg PG vesicles but not Egg PC vesicles. The figure also shows that DLS is a sensitive tool for detecting a difference between un-aggregated and aggregated vesicle states through the difference in decay time of the intensity-intensity autocorrelation function : a change in decay time is detectable for concentrations as low as 1 CCT per vesicle.

The mean radius and polydispersity of vesicles before and after the introduction of CCT were determined by fitting Eq. 2.25 to the intensity-intensity autocorrelation function data, with Eq. 2.40 used as the field-field autocorrelation function. Figures 5.2.a and b show the mean radius and the polydispersity, respectively, as a function CCT concentration for Egg PC and Egg PG vesicles. There is no change in vesicle size and polydispersity when CCT with concentration as large as 40 CCT/vesicle was introduced to Egg PC vesicles. In contrast, the radius and polydispersity of Egg PG vesicles increase when CCT was introduced with concentration as small as 1 CCT/vesicle. As indicated in Fig. 5.1, CCT does not induce aggregation of vesicles made from EggPC, a weak CCT activator. However, CCT induces aggregation for vesicles made from Egg PG, a strong CCT activator.

When CCT is introduced into the vesicle dispersions, there is a possibility of an initial local concentration of CCT that is quite high. This could cause the binding of CCT to only a few vesicles in the area where CCT was initially introduced. To check for this possibility, DLS measurements were conducted on CCT-vesicles prepared by two different methods. In the first one, CCT is added to a dilute vesicle dispersion, as explained in the method section. In the second, a concentrated vesicle dispersion is added to a dilute CCT solution.

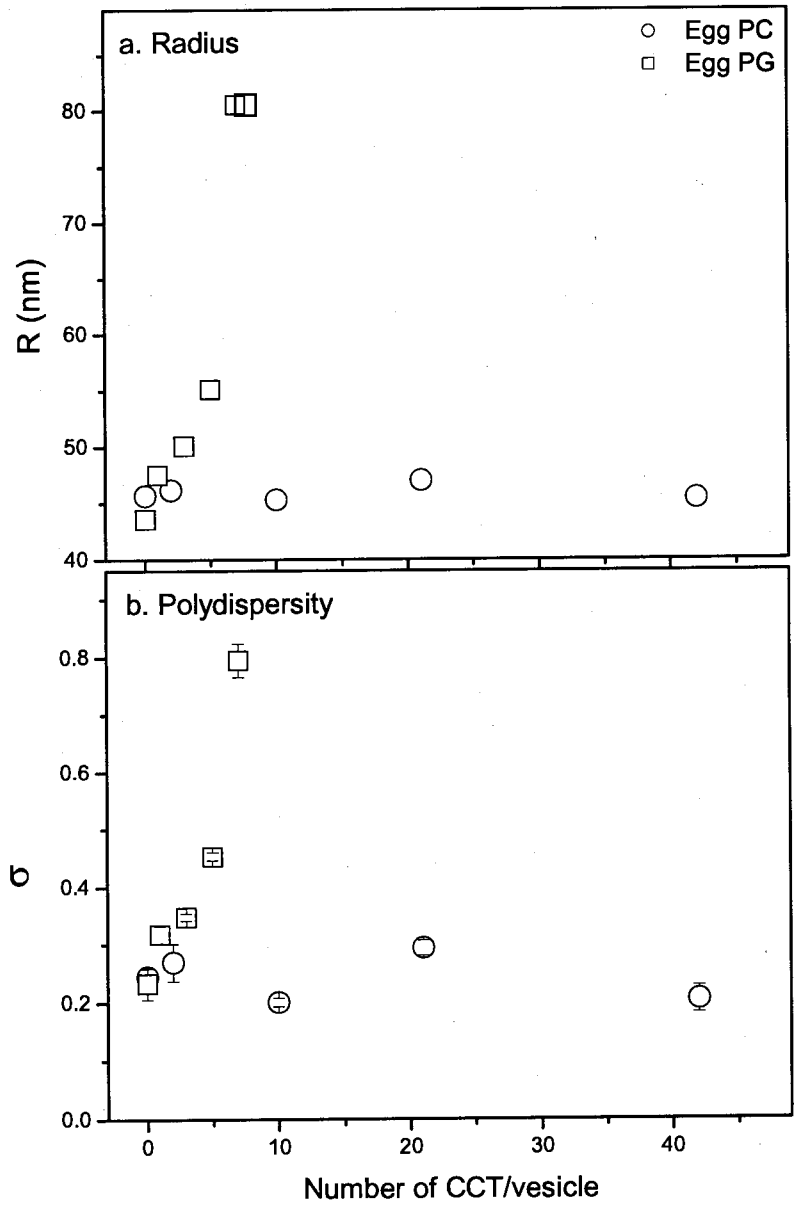

Figure 5.2: a. The mean radius R and b. the polydispersity σ of vesicles made from Egg PC and Egg PG before and after introduction of CCT.

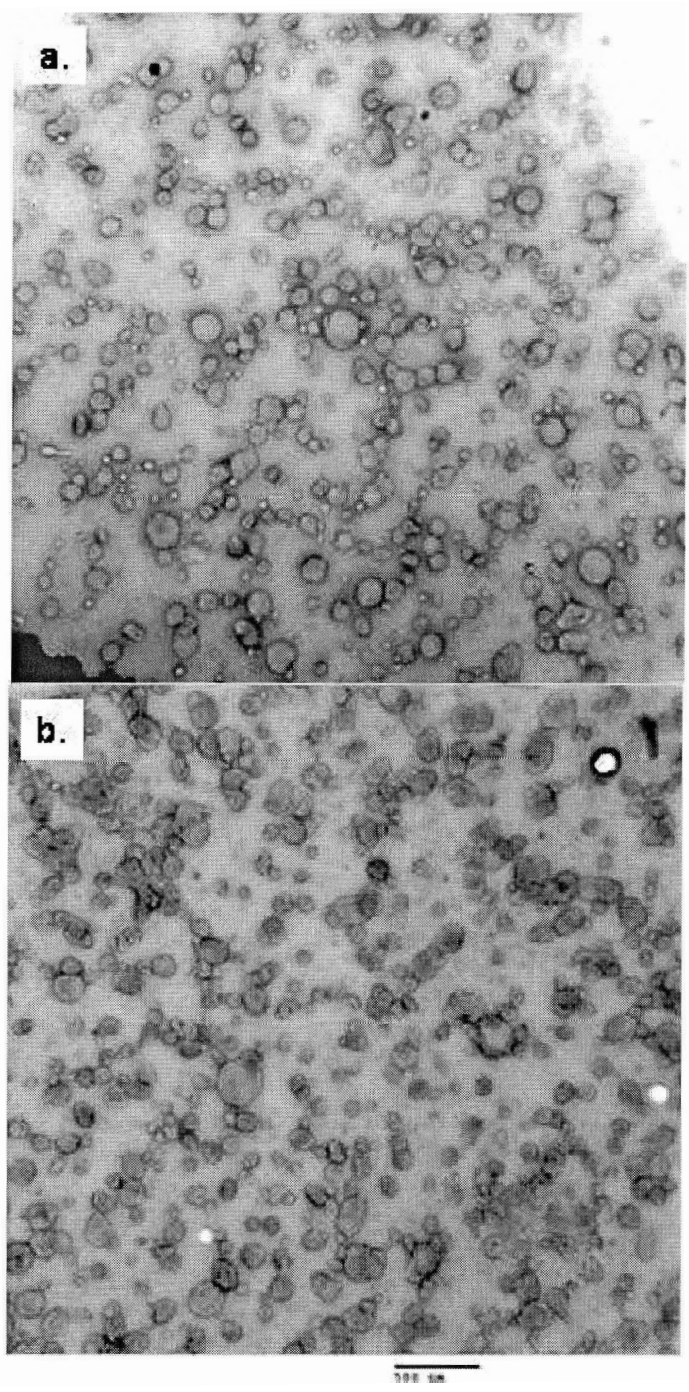

Figure 5.3: A typical TEM micrographs of a. pure Egg PG vesicles and b. Egg PG vesicles plus CCT with concentration of 3 CCT/vesicle.

The second procedure ensures the uniform distribution of CCT in the vesicle dispersion. The results of the measurements show no difference in the mean radius and polydispersity of CCT-vesicles prepared by these two procedures. Therefore, I believe that there is no CCT dispersion problem in the experiments.

To confirm the results from DLS measurements, the effect of CCT on the aggregation state of Egg PG vesicles was also observed using TEM. Figure 5.3 shows a typical TEM micrograph of a) pure Egg PG vesicles and b) Egg PG vesicles plus CCT with concentration of 3 CCT/vesicle. The mean radius and polydispersity of this particular sample were determined by analyzing at least 300 vesicles. Figure 5.4 shows the histogram of vesicle radius for vesicles whose representative micrographs are shown in Fig. 5.3. The mean radius of Egg PG increases from 46.0 ± 24.0 nm for pure Egg PG to 56.0 ± 28.0 nm when CCT with a concentration of 3 CCT/vesicle was introduced. The values are comparable to the mean radius from DLS which increases from 43.6 ± 10.1 nm for pure Egg PG to 50.1 ± 17.4 nm when CCT with the same concentration was introduced. The uncertainties in the mean radius values are the standard deviations of the distributions. Results of TEM measurements for other concentrations of CCT show that the mean radius increases with CCT concentration, which is consistent with those from DLS.

To examine the amount of Egg PG in Egg PG:Egg PC membranes required for vesicle aggregation to occur, DLS was used to monitor the radius and polydispersity of vesicles made from mixtures of Egg PC and Egg PG in the presence of CCT. The concentrations of Egg PG used for these experiments were 15, 25, 33, 50 and 100 mol %. Figures 5.5.a and b

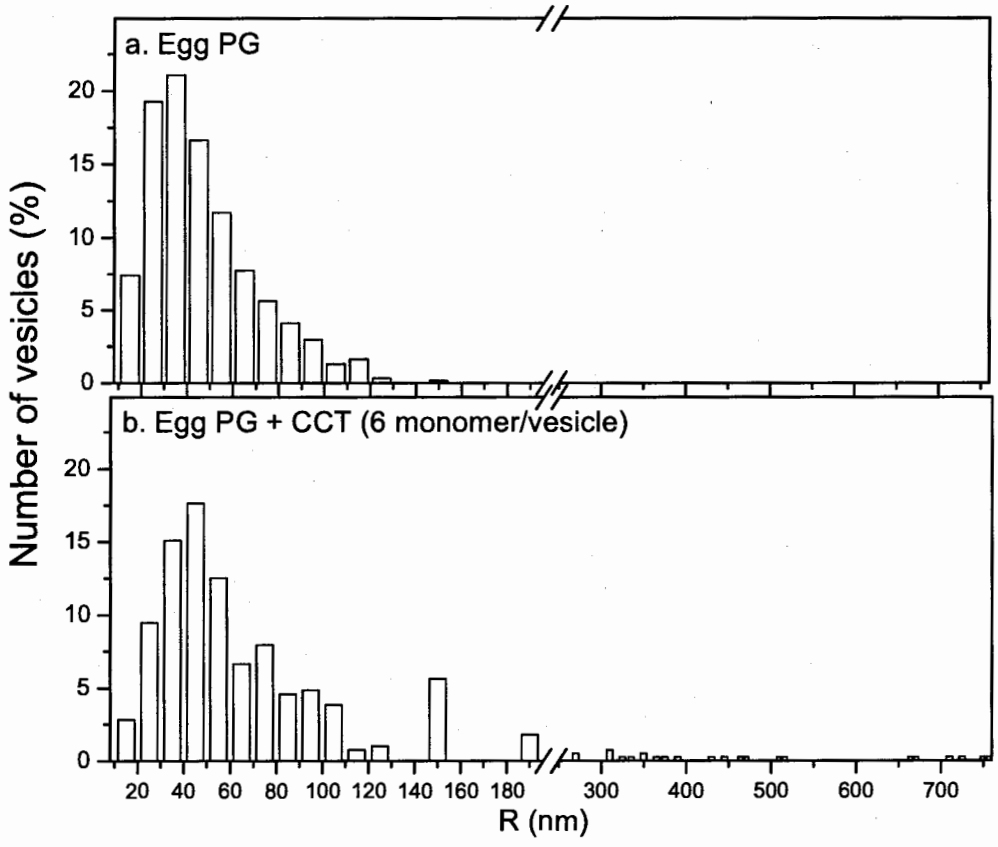

Figure 5.4: Histogram of vesicle radius data for a. Egg PG and b. Egg PG plus CCT with concentration of 3 CCT/vesicle from TEM measurements.

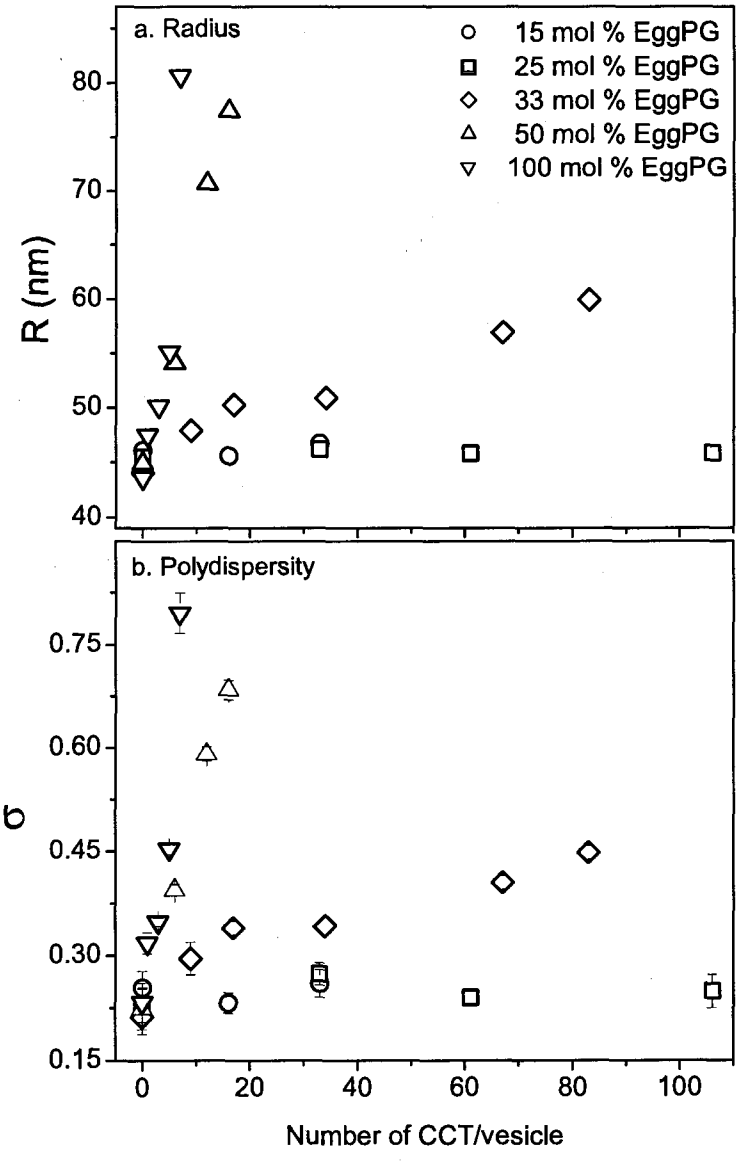

Figure 5.5: a. The mean radius and b. the polydispersity of Egg PC:Egg PG mixtures before and after the introduction of CCT.

show the plot of the mean radius and the polydispersity of vesicles made from Egg PC:Egg PG mixtures before and after introduction of CCT. The figure shows that no aggregation occurs in mixtures containing 15 and 25 mol % of Egg PG. Aggregation starts to occur when the concentration of Egg PG reaches 33 mol %, as indicated by an increase in vesicle size and polydispersity.

DLS experiments were also conducted to observe the ability of different domains of CCT, including CCT-236 (CCT without domain M) and the 57-mer peptide (only domain M), to induce vesicles aggregation. Figure 5.6 shows the mean radius and the polydispersity of Egg PG vesicles before and after introduction of CT-236 or peptide. Similar data for CCT from Fig. 5.2 is shown for comparison. The figure shows that fragments of CCT, CCT-236 and 57-mer peptide, do not cause vesicle aggregation. Therefore, the whole structure of CCT is required for aggregation of Egg PG vesicles.

5.3.2 Effect of CCT on Class I and Class II Lipid Vesicles

The effect of CCT on the aggregation state of class I and class II lipid vesicles was studied by observing the change in their size and polydispersity using DLS before and after introduction of CCT. POPS, in addition to Egg PG, represents class I lipids, while EggPC:DOPE (40:60) and EggPC:DAG (85:15) represent class II lipids. In addition, experiments were done on vesicles made from Egg PC:OA (50:50), where OA shares characteristics of both class I and class II lipids. Figures 5.7.a and b show the mean radius and the polydispersity of vesicles, respectively, made from Egg PG, POPS, EggPC:DOPE, EggPC:DAG and Egg PC:OA as a function of CCT concentration. There is a significant change in the mean radius and

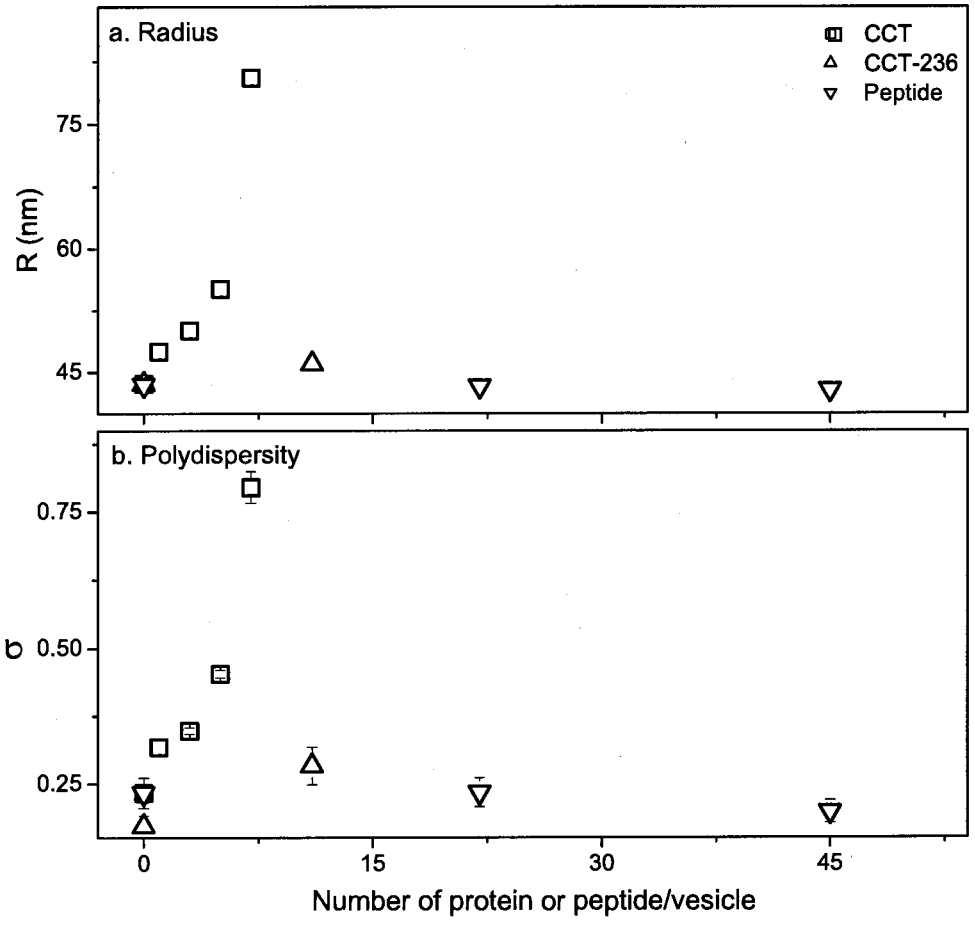

Figure 5.6: a. The mean radius and b. the polydispersity of Egg PG vesicles before and after introduction of CCT or CCT-236 or peptide.

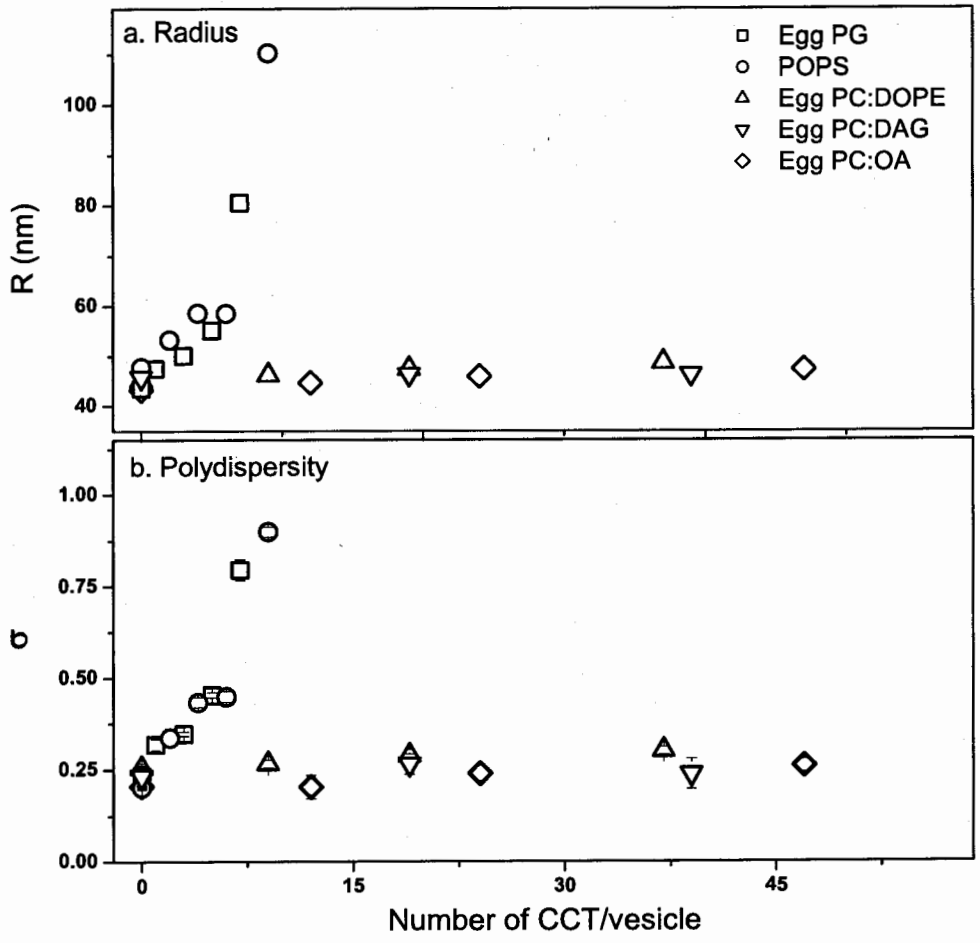

Figure 5.7: a. The mean radius and b. the polydispersity of vesicles made from Egg PG and POPS, Egg PC:DAG (85:15) and Egg PC:DOPE (40:60), Egg PC:OA.

polydispersity when CCT is introduced into vesicles made from class I lipids, including Egg PG and POPS. This indicates that CCT induces aggregation of vesicles made from class I lipids. However, there is no significant change in the mean radius and polydispersity when CCT is introduced to vesicles made from class II lipids, including Egg PC:DAG and Egg PC:DOPE. This indicates that CCT does not induce aggregation of vesicles made from class II lipids. A change in the mean radius of 10 % is observed when CCT with concentration of 40 CCT/vesicle is introduced to vesicles made from Egg PC:OA. This indicates that CCT induces some aggregations of vesicles made from Egg PC:OA.

5.4 Discussion

5.4.1 CCT-Membrane Binding Strength and Vesicle Aggregation

Although CCT binds to class I and II lipid membranes, aggregation takes place only for class I lipid vesicles. As class I lipids are more potent than class II lipids in binding CCT [9, 95], the aggregation of CCT seems to be correlated to the CCT binding strength to the membrane. This is supported by the results of aggregation of vesicles made from Egg PC:Egg PG mixture where the concentration of Egg PG was varied. Since membrane-CCT binding strength depends on the amount of anionic lipids in the membrane, varying the concentration of Egg PG changes the membrane binding strength of CCT. The results show that no aggregation takes place at small concentration of Egg PG and aggregation starts to occur when the concentration of Egg PG reaches 33 mol %. This suggests that aggregation can take place when the CCT binding strength is sufficient. The observation that no aggregation

of vesicles occurs when CCT is introduced to Egg PC vesicles is consistent with the fact that CCT binds poorly to Egg PC membrane [8, 94].

The CCT binding strength required for the aggregation can be estimated by determining the binding strength of CCT to membranes of Egg PC:Egg PG (67:33) or Egg PC:OA (50:50). There is some aggregation observed when CCT is introduced to vesicles made from these mixtures. The CCT binding strength can be determined using the relation,

$$\Delta G_{binding} = -R\ T\ ln\ K_x, \tag{5.1}$$

where the partition coefficient K_x is the ratio of bound to free proteins. The partition coefficients for these membranes are in the range of 5 - 8 x 10^5 [95]. This value corresponds to a free energy of binding $\Delta G_{binding}$ of -7.7 to -8 kcal/mol and suggests that the binding strength must be at least approximately 8 kcal/mol (10 k_bT/molecule) to allow the occurrence of aggregation.

Previous studies of the kinetics of binding of myelin basic protein [101] and mitochondrial creatine kinase octamer [102] to vesicle membranes as well as vesicle aggregation induced by the proteins show that aggregation is a relatively slow process compared to binding. Based on these results, for aggregation to take place, the time for interaction between protein and membrane must be longer than the time scale for aggregation. The requirement for sufficient binding strength for CCT to the membranes, therefore, is caused by the fact that the stronger binding may increase the interaction time between CCT and the membranes. Consequently, the strong binding of CCT to class I lipid membranes may produce an interaction time which is sufficient for aggregation to occur. On the other hand, the weak binding of CCT to class

II lipid membranes may result in a short interaction time, so that CCT dissociates faster than aggregation can occur.

5.4.2 Cross-Bridging Mechanism for Aggregation

The fact that it takes only 1 CCT per vesicle to stimulate the aggregation of anionic lipid vesicles favors the cross-bridging mechanism for aggregation. This mechanism is different from aggregation induced by other proteins such as : annexin IV [103], myelin proteolipid [104], and cytochrome c [105], where proteins cover the vesicle surface causing protein oligomerization [103, 104] and/or vesicle charge neutralization [105].

The results showing that CCT induces aggregation of vesicles made from class I but not from class II lipids reveal the existence of a different mode of binding of CCT on the membranes for these two activators. In membranes of class I lipids, the mode where each monomer of CCT binds to the membranes of two vesicles in a cross-bridging mode as shown in Fig. 1.1b. dominates. However, in membranes of class II lipids, both monomers probably bind to the membrane of one vesicle as shown in Fig. 1.1a. Alternatively, the weaker energetics of interaction of CCT and class II lipid suggests that only one monomer binds to one vesicle, while the other remains unbound [95].

The results showing that CCT induces aggregation of vesicles made from class I but not for class II lipids and that CCT can be activated by both class I and II lipids indicate that cross-bridging is not a required step for CCT activation. Although Class II lipids activate CCT, there is no indication of cross-bridge mode on vesicles containing these lipids.

The ability of CCT to cross-bridge anionic lipid vesicles is a new aspect of the interactions

between CCT and lipid membranes that has not been studied previously. The in vivo function of CCT in relation to this ability is not known. However, in Endoplasmic reticulum and nuclear membranes where CCT translocates, there are 20-30 mol % anionic lipids [106, 107]. This amount is comparable to the threshold concentration of 33 mol % for anionic lipids in membrane to promote vesicle cross-bridging. This suggests that CCT has the potential to cross-bridge cell membranes that are in close proximity.

5.4.3 Electrostatic Repulsion of Charged Membranes versus Aggregation

The results showing that CCT induces aggregation of negatively charged vesicles (Egg PG and POPS vesicles) raise an issue of the contribution of the repulsive electrostatic interaction between charged vesicles. For negatively charged lipid vesicles in an electrolyte solution, cations in the solution approach the membrane surface, while the anions are repelled from the surface. Balance between electrostatic forces as well as thermal motion of the ions results in a high concentration of cations and a low concentration of anions near the membrane surface which is known as the diffusive double layer. As cations bind to the surface, they neutralize the surface charge, reducing the repulsive electrostatic interaction between vesicles. Far from the surface, the concentration of ions is the same as the bulk concentration. The repulsive electrostatic double layer interaction is a long range interaction. The vesicles also feel a long range van der Waals interaction which is attractive. The combination of these interactions is described by the Derjaguin-Landau-Verwey-Overbeek (DLVO) theory [64].

For negatively charged membranes composed of vesicles with radius R in a monovalent electrolyte solution, the electrostatic energy between surfaces of two vesicles is expressed by

[108],

$$U = \frac{64\pi k_b T R n}{\kappa^2} \left(\tanh \left(\frac{e\Psi_o}{4k_b T} \right) \right)^2 \exp(-\kappa D), \tag{5.2}$$

where e, κ and Ψ_o are the electron charge, the Debye constant and the surface potential of the membrane, respectively, n is the density of monovalent electrolyte and D is the distance between surfaces. The Debye constant κ is determined using the relation,

$$\kappa = \left(\frac{2ne^2}{\epsilon_r \epsilon_o k_b T} \right), \tag{5.3}$$

where ϵ_r and ϵ_o are the relative permittivity of the medium and permittivity of vacuum, respectively. The relation between surface potential Ψ_o and charge density σ of the membrane is written as [108],

$$\sigma = \frac{2\epsilon_r \epsilon_o \kappa k_b T}{e} \sinh \left(\frac{e\Psi_o}{2k_b T} \right). \tag{5.4}$$

In Eq. 5.4, the charge density σ is defined as a cation-bound surface, thus smaller than the original charge density σ_o. The relation between σ_o and σ is written as [109]

$$\sigma = \frac{\sigma_o}{1 + Kn \exp\left(-\frac{e\Psi_o}{2k_b T} \right)}, \tag{5.5}$$

where K is the binding constant for the monovalent cation. The surface potential can be determined by equating Eqs. 5.4 and 5.5, if K and σ_o are known.

The van der Waals interaction energy between surfaces of two vesicles separated by distance D is written as [110],

$$V = V(R, R) + V(R - t, R - t) - 2V(R, R - t), \tag{5.6}$$

where t is the thickness of the bilayer and,

$$\begin{aligned} V(R, R-t) &= -\frac{A}{6}\Big(\frac{2R(R-t)}{(D+2R)-(R+(R-t))^2} \\ &+ \frac{2R(R-t)}{(D+2R)-(R-(R-t))^2} \\ &+ \ln\frac{(D+2R)-(R+(R-t))^2}{(D+2R)-(R-(R-t))^2}\Big). \end{aligned} \tag{5.7}$$

Thus, the total interaction energy of two vesicles is given by,

$$G = U + V. \tag{5.8}$$

There are also solvation and steric interactions at short range, but for monovalent electrolyte such as NaCl used in these experiments, the interaction can be described sufficiently by DLVO theory [109].

Figure 5.8 shows the graphs of U, V and G as a function of distance between surfaces of two vesicles for Egg PG vesicles in 150 mM NaCl as used in these experiments. Values used in these calculations include σ_o of approximately 0.235 C/m^2, equivalent to 1 electron per headgroup, a binding constant K for Na^+ of 0.7 M^{-1} [111], and a bilayer thickness of 4 nm [97], while the radius of the vesicles was estimated from DLS experiments. The figure shows that two vesicles repel each other over all length scales with a maximum value at a separation distance around 0.2 nm. Figure 5.8 indicates that the ions present, which can screen the surface charge are not sufficiently concentrated to induce vesicle aggregation, which is consistent with observations of pure POPS and Egg PG vesicle dispersions. The figure also suggests that, for aggregation to take place, the dimension of CCT must be comparable to or larger than 4 nm, the distance where the system experiences more repulsive

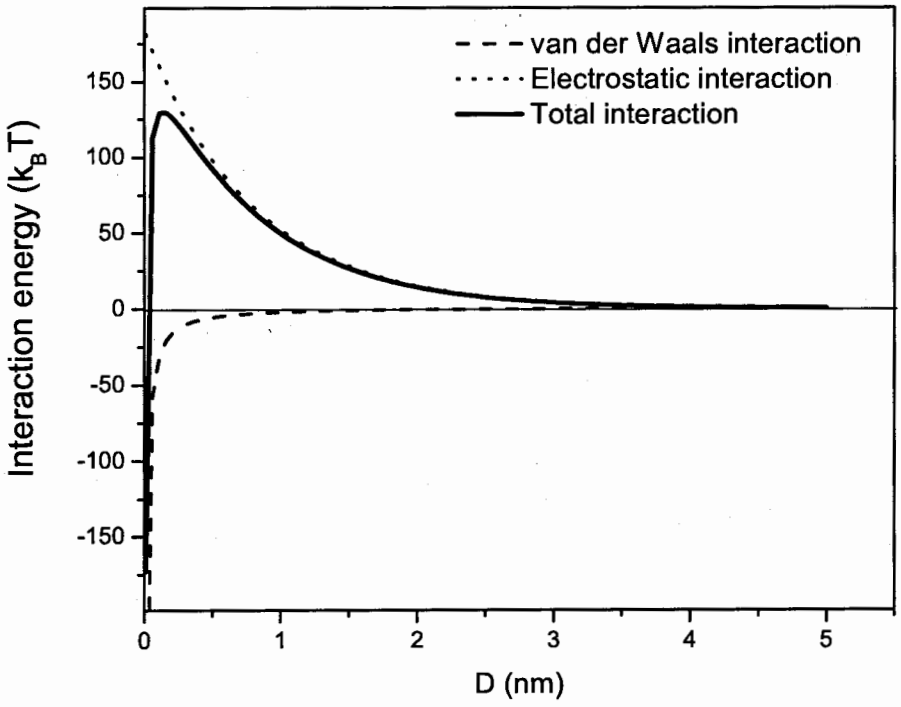

Figure 5.8: Electrostatic and van der Waals energy between vesicles as a function of surface separation D.

interactions when the vesicles approach each other. The diameter of the CCT dimer has been estimated to be 10 nm as determined from the structure of glycerophosphate cytidylyltransferase [90] and domain M [112]. Thus, there is a repulsive interaction between vesicles at a very short distances that CCT must overcome, but the CCT dimension is sufficient to make this possible.

5.5 Summary

This chapter contains studies on the effect of CCT on aggregaion of vesicles containing class I and class II CCT activators. Aggregation occurs when CCT is introduced to samples of class I lipid vesicles. In contrast, there is no indication of aggregation when CCT is introduced to samples of class II lipid vesicles. The results suggest that binding of CCT to class I lipid membranes was dominated by the cross-bridging mode, while in class II lipid membranes either two domain Ms bind to the same vesicle or only one monomer binds while the other is unbound. It is thought that the cross-bridging mode is correlated to the strength of the CCT binding to the membrane, which presumably enables interaction time between CCT and membrane. The cross-bridge only occurs when one domain M of CCT dimer is bound to one vesicle and the second domain M is not bound and collides with another vesicle. This requires binding time scale larger than collision or cross-bridging time scale.

Chapter 6

Conclusion

There are four different studies described in this thesis. The first shows comparison of the size distribution of vesicles determined from different methods of DLS data analysis. The second discusses the properties of extruded vesicles, including size distributions and lamellarity, as affected by the size distributions of the pores in PCTE membranes. The third studies the effect of sterols, including cholesterol, lanosterol and ergosterol on the mechanical strength of lipid membranes, as probed by measuring the lysis tension of vesicles. The fourth investigates the interaction between CCT and lipid membranes by observing the aggregation of lipid vesicles induced by CCT.

DLS data taken at different scattering angles were analyzed to determine size distributions of vesicles using different methods of analyzes. To extract the actual size distribution of vesicles from DLS data is a complicated task. Instead, in these studies, I assumed a functional form of the size distributions of vesicles and determine parameters associated with the

size distribution from fitting procedure. The Schulz and Gaussian distributions were chosen to describe the size distribution of vesicles and the results show that the Schulz distribution is more appropriate than the Gaussian distribution. This is shown by the fact that the measured distribution is independent of the scattering angle when the Schulz distribution is used.

Different sizes of the pores in PCTE membranes are used to produce vesicles and the size distribution and the lamellarity of the vesicles were determined. The results show that although the size of the extruded vesicles can vary depending on the size of the pores used, only small vesicles have narrow size distributions and are unilamellar. The multilamellarity of extruded vesicles when produced using large pores is presumably due to the break-up of MLVs into smaller MLVs that are comparable to the size of the pores. The smaller MLVs then can squeeze easily through pores without further rupture. The polydispersity of the vesicles produced using larger pores is large, although the polydispersity of the pores is small. The polydispersity of the vesicles is most likely due to the presence of small vesicles that are produced spontaneously when the lipid was initially dispersed in water or, alternatively, as a consequence of the process of extrusion.

Vesicles made from mixtures of POPC and various sterols were used to observe the effect of sterols on the lysis tension of lipid membranes. The concentration of sterols incorporated into the vesicles was varied from 10 to 30 mol %. The lysis tension increases with the concentration of sterols, where cholesterol shows the largest effect followed by lanosterol and ergosterol. The increase in lysis tension as a function of sterol concentration is almost

linear for all sterols. The increase in the lysis tension of POPC membranes due to the incorporation of sterols is correlated to the increase in the order parameter, the bending rigidity and the area expansion modulus. The plot of the lysis tension data as a function of the order parameter, the bending rigidity and the area expansion modulus shows that data for different mixtures collapse to a universal curve for all graphs independent of the sterols used. This shows the strong relationship between the lysis tension with these properties of the membranes.

There is a strong linear relationship between the lysis tension measured in these studies and the order parameter measured by other authors. So, the effect of sterols on the lysis tension of POPC membranes is correlated to their effect on the lipid chain order. The increase in the lysis tension and, consequently, the strength of lipid membranes, as sterols are incorporated into model membranes confirms the contribution of sterols to cell viability, which depends on maintaining an intact plasma membrane. In addition, the mechanical strength of lipid membranes is an important factor in the application of vesicles as carriers in drug delivery, where the strength relates to a stress resistance induced by lytic agents in the host.

Sterols impact the lysis tension of vesicles depending on whether vesicles are composed of saturated or unsaturated lipids, as indicated in these studies using POPC, an unsaturated lipid, and other studies mentioned in the text using DPPC, a saturated lipid. The impact of sterols on other properties of membranes of saturated and unsaturated lipids, for example, the area expansion modulus, has also been observed. Cholesterol shows the the largest effect

in unsaturated membranes, while ergosterol shows the largest effect in saturated membranes. This indicates that the impact of the sterols on the properties of the membranes depends on both the structure of the sterols and the nature of the lipids. Other experiments of interest are measurements of membrane properties for membranes made up of mixtures of saturated and unsaturated lipids. The results of these studies could reveal other characteristics of lipid:sterol interactions.

The interaction between CCT and lipid membranes was conducted by observing the vesicle aggregation after introducing CCT to sample of vesicles made both from lipids that activate CCT, including class I and class II lipids, and lipids that do not activate CCT. CCT induces aggregation of vesicles made from class I lipids but does not induce aggregation of vesicles made from both non-activating and class II lipids. The fact that CCT binds to membranes of both class I and class II lipids but only induces aggregation of class I lipid vesicles suggests that the mode of CCT binding is different for membranes of class I and class II lipids. The occurrence of aggregation suggests that the CCT dimer is bridging between two vesicles. In class I lipid membranes, the cross-bridging mode dominates. In class II lipid membranes, we propose two possible binding mechanisms, either two domain Ms bind to one vesicle or only one monomer binds while the other is unbound.

The ability of CCT to cross-bridge class I lipid vesicles is a new aspect of interactions between CCT and lipid membranes that has not been studied previously. The in vivo function of CCT in relation to this ability is not known; but this ability shows that CCT has the potential to cross-bridge cell membranes that are in close proximity.

Binding of CCT in the cross-bridging mode, which is dominant in class I lipid membranes, ensures the binding of two domain Ms, while binding in the non-cross-bridging mode, as is the case for class II lipid membranes, indicates the possibility that one domain M is unbound. This raises the question of whether or not the higher activity of CCT in class I lipid membranes is due to the fact that both domain Ms are engaged in the membrane, while in class II lipid membranes only one domain M is bound to the membrane. However, these experiments cannot distinguish the mode of binding as depicted in Fig. 1.1.b from the other mode where only one monomer binds. Further experiments using CCT heterodimers containing only one membrane-binding domain may answer this question. One possible scenario to produce CCT heterodimers is by separating monomers of each CCT and and the 57-mer peptide (CCT dimer without domain M), mixing the products containing different combinations of dimers, and isolating the dimers, where only one monomer contains domain M. Separation of monomers of CCT and the peptide can be done using detergents, since they are bound by hydrophobic interactions. However, isolating the dimer of interest from a few different dimers may be a complicated task.

Bibliography

[1] R. B. Gennis. *Biomembranes Molecular Structure and Function.* Springer-Verlag, New York, 1989.

[2] D. Needham and R.S. Nunn. Elastic deformation and failure of lipid bilayer membrane containing cholesterol. *Biophys. J.* 58:997-1009, 1990.

[3] P.J. Patty and B.J. Frisken. The pressure-dependence of the size of extruded vesicles. *Biophys. J.* 85:996-1004, 2003.

[4] L. Finegold, *Cholesterol in Membrane Models.* CRC Press, Boca Raton, 1995.

[5] K.E. Bloch. Sterol structure and membrane function. *CRC. Crit.Rev.Biochem.* 14:47-92, 1983.

[6] R.B. Cornell. Chemical cross-linking reveals a dimeric structure for CTP:phospho-choline cytidylyltransferase. *J. Biol. Chem.* 264:9077-9081, 1989.

[7] R.B. Cornell and I.C. Northwood. Regulation of CTP:phosphocholine cytidylyltransferase by amphitropism and relocalization. *Trends Biochem. Sci* 25:441-447, 2000.

[8] R.S. Arnold, A. De Paoli-Roach and R.B. Cornell. Binding of CTP:phosphocholine cytidylyltransferase to lipid vesicles: Diacylglycerol and enzyme dephosphorylation increase the affinity for negaively charged membrane. *Biochemistry* 36:6149-6156, 1997.

[9] J.E. Johnson N.M. Rao, S.W. Hui and R.B. Cornell. Conformation and lipid binding properties of four peptides derived from the membrane-binding domain of CTP:phosphocholine cytidylyltransferase. *Biochemistry* 37:9509-9519, 1998.

[10] J.E. Johnson, M. Xie, L.M. Sing, R. Edge and R.B. Cornell. Both acidic and basic amino acids in an amphitropic enzyme, CTP:phosphocholine cytidylyltransferase, dictate its selectivity for anionic membranes. *J. Biol. Chem.* 278:514-522, 2003.

[11] H. Jamil, G. Hatch, and D.E. Vance. Evidence that binding of CTP:phosphocholine cytidylyltransferase to membranes in rat hepatocytes is modulated by the ratio of bilayer- to non bilayer-forming lipids. *Biochem. J.* 291:419-427, 1993.

[12] G.S. Attard, R.H. Templer, W.S. Smith, A.N. Hunt, and S. Jackowski. Modulation of CTP:phosphocholine cytidylyltransferase by membrane curvature elastic stress. *Proc. Natl. Acad. Sci. USA.* 97:9032-9036, 2000.

[13] S.M.A. Davies, R.M. Epand, R. Kraayenhof, and R.B. Cornell. Regulation of CTP:phosphocholine Cytidylyltranferase activity by physical properties of lipid membranes: An important role for stored curvature strain energy. *Biochemistry* 40:10522-10531, 2001.

[14] R.S. Arnold and R.B. Cornell. Lipid regulation of CTP:phosphocholine cytidylyltransferase : electrostatic, hydrophobic, and synergistic interactions of anionic phospholipids and diacylglycerol. *Biochemistry* 35:9917-9924, 1996.

[15] S. Taneva, J.E. Johnson and R.B. Cornell. Lipid-induced conformational switch in the membrane binding domain of CTP:Phosphocholine Cytidylyltransferase: A circular dichroism study. *Biochemistry* 42:11768-11776, 2003.

[16] M.J. Hope, M.B. Bally, G. Webb and P.R. Cullis. Production of large unilamellar vesicles by a rapid extrusion procedure: characterization of size, trapped volume and ability to maintain a membrane potential. *Biochim. Biophys. Acta* 812:55-65, 1985.

[17] B.J. Berne and R. Pecora. *Dynamic Light Scattering with Applications to Chemistry, Biology and Physics.* Oxford University Press, Oxford, 1993.

[18] P. Stepanek. Data analysis in dynamic light scattering. In W. Brown. Ed., *Dynamic Light Scattering : The Method and Some Applications,* pp.177-241. Oxford University Press, Oxford, 1993.

[19] C. Tanford. *Physical Chemistry of Macromolecules.* John Wiley & Sons, Inc, New York, 1961.

[20] F.R. Hallett, T. Craig, J. Marsh and B. Nickel. Particle size analysis : number distributions by dynamic light scattering. *Can. J. Spectr.* 34:63-70, 1989.

[21] G. Bryant, C. Abeynayake and J.C. Thomas. Improve particle size distribution measurements using multiangle dynamic light scattering. 2. Refinements and applications. *Langmuir* 12:6224-6228, 1996.

[22] D.E. Koppel. Analysis of macromolecular polydispersity in intensity autocorrelation spectroscopy : the method of cumulants. *J. Chem. Phys.* 57:4814-4820, 1972.

[23] B.J. Frisken. Revisiting the method of cumulants for analysis dynamic light scattering data. *J. Appl. Opt.* 40:4087-4091, 2001.

[24] L.H. Hanus and H.J. Ploehn. Conversion of intensity-average photon correlation spectroscopy measurements to number-average particles size distributions.1. Theoretical development. *Langmuir* 15:3091-3100, 1999.

[25] J.C. Thomas. The determination of log normal particle size distributions by dynamic light scattering. *J. Colloid Interface Sci.* 117:187-192, 1987.

[26] C.B. Bargeron. Measurements of continuous distribution of spherical particles by intensity correlation spectroscopy : analysis by cumulants. *J. Chem. Phys.* 61:2134-2138, 1974.

[27] D.S. Horne. Determination of the size distribution of Bovine Casein micelles using photon correlation spectroscopy. *J. Colloid Interface Sci.* 98:537-548, 1984.

[28] T.W. Taylor, S.M. Scrivner, C.M. Sorensen and J.F. Merklin. Determination of the relative number distribution of particle sizes using photon correlation spectroscopy. *Appl. Opt.* 24:3713-3717, 1985.

[29] J.C. Selser. Letter : A light scattering method of measuring membrane vesicle-number average size and size dispersion. *Biophys. J.* 16:847-848, 1976.

[30] G. Maulucci, M. De Spirito, G. Arcovito, F. Boffi, A.C. Costellano and G. Briganti. Particle size distribution in DMPC vesicles solutions undergoing different sonication times. *Biophys. J.* 88: 3545-3550, 2005.

[31] B. Chu. *Laser Light Scattering: Basic Principle and Practice.* Academic Press, Inc, New York, 1991.

[32] F.R. Hallett, J. Watton and P. Krygsman. Vesicle sizing-number distribution by dynamic light scattering. *Biophys. J.* 59:357-362, 1991.

[33] H.C. Van De Hulst. *Light Scattering by Small Particles.* Dover Publications, Inc, New York, 1981.

[34] J. Pencer and F.R. Hallett. Effect of vesicle size and shape on static and dynamic light scattering measurements. *Langmuir* 19:7488-7497, 2003.

[35] B. Mui, P.R. Cullis, E. Evans and T.D. Madden. Osmotic properties of large unilamellar vesicles prepared by extrusion. *Biophys. J.* 64:443-453, 1993.

[36] R.R.C. New. Influence of liposome characteristics on their properties and fate. In J.R.Philippot, F.Schuber. Eds., *Liposomes as Tools in Basic Research and Industry,* pp.4-20 CRC Press, Boca Raton, 1995.

[37] D.D. Lasic. *Liposomes : from Physics to Applications.* Elsevier, Amsterdam, 1993.

[38] G. Gregoriadis, Ed. *Liposomes as Drug Carrier Recent Trends and Progress.* John Wiley and Sons, New York, 1988.

[39] C. Nicolau and A. Cudd. Liposomes as carriers of DNA. *Crit. Rev. Therap. Drug Carr. Systems* 6:239-271, 1989.

[40] J.L. Rigaud and B. Pitard. Liposomes as tools for reconstituion of Biological systems. In J.R.Philippot, F.Schuber. Eds. *Liposomes as tools in basic research and industry* pp.71-88. CRC Press, Boca Raton, 1995.

[41] D.D. Lasic. Novel applications of liposomes. *TIBTECH* 16:307-321, 1998.

[42] A. Chonn and P.R. Cullis. Recent advances in liposome technologies and their applications for systemic gene delivery *Adv. Drug Deliv. Rev.* 30:73-83, 1998.

[43] M.C. Woodle, M.S. Newman, and P.K. Working. Biological properties of sterically stabilized liposomes. In D. Lasic, and F. Martin. Eds., *Stealth Liposomes*, CRC Press, Boca Raton, 1995.

[44] D.C. Litzinger, A.M.J. Buiting, N. van Rooijen, and L. Huang. Effect of liposome size on the circulation time and intraorgan distribution of amphiphatic poly (ethylene glycol)-containing liposomes. *Biochim. Biophys. Acta* 1190: 99-107, 1994.

[45] V. Roden and S.M. Goldin. Formation of unilamellar lipid vesicles of controlable dimensions by detergent dialysis. *Biochemistry* 18:4173-4176, 1979.

[46] F. Szoka and D. Papahadjopoulos. Procedure for preparation of liposomes with large internal aqueous space and high capture by reverse-phase evaporation. *Proc. Natl. Acad. Sci. USA* 75:4194-4198, 1978.

[47] L.D. Mayer, M.J. Hope and P.R. Cullis. Vesicles of variable sizes produced by a rapid extrusion procedure. *Biochim. Biophys. Acta* 858:161-168, 1986.

[48] R. Cortesi, E. Esposito, S. Gambarin, P. Telloli, E. Menegatti, and C. Nastruzzi. Preparation of liposomes by reverse-phase evaporation using alternative organic solvents. *J. Microencapsul.* 16:251-256, 1999.

[49] K. Matsuzaki, O. Murase, K. Sugishita, S. Yoneyama, K. Akada, M. Ueha, A. Nakamura, S. Kobayashi. Optical characterization of liposomes by right angle light scattering and turbidity measurement. *Biochim. Biophys. Acta* 1467:219-226, 2000.

[50] D.G. Hunter and B.J. Frisken. The effects of lipid composition and extrusion pressure and temperature on the properties of phospholipid vesicles. *Biophys. J.* 74:2996-3000, 1998.

[51] S. Sriwongsitanont and M. Ueno. Effect of a PEG lipid (DSPE-PEG2000) and freeze-thawing process on phospholipid vesicle size and lamellarity. *Colloid Polym. Sci.* 282:753-760, 2004.

[52] Y. Talmon, J.L. Burns, M.H. Chesnut, D.P. Siegel. Time-resolved Cryotransmission electron microscopy. *J. Electron Microsc. Tech.* 14:6-12, 1990.

[53] M. Almgren, K. Edwards, and G. Karlsson. Cryo transmission electron microscopy of liposomes and related structures. *Colloid. Surf. A.* 174:3-21, 2000.

[54] B.A. Korgel, J.H. van Zanten, and H.G. Monbouquette. Vesicle size distribution measured by field-flow-fractionation couple with multiangle light scattering. *Biophys. J.* 74:3264-3272, 1998.

[55] J.H. van Zanten, and H.G. Monbouquette. Characterization of vesicles by classical light scattering. *J. Colloid Interface Sci.* 146:330-336, 1991; Phosphatidylcholine vesicle diameter, molecular weight and wall thickness determined by static light- scattering. *J. Colloid Interface Sci.* 165:512-518, 1994.

[56] J.C. Selser and R.J. Baskin. A light scattering characterization of membrane vesicles. *Biophys. J.* 16:337-356, 1976.

[57] S. Kolchens, V. Ramaswami, J. Birgenheier, L. Nett and D.F. O'Brien. Quasi-elastic light scattering determination of the size distribution of extruded vesicles. *Chem. and Phys. Lipids* 65:1-10, 1993.

[58] A.J. Jin, D. Huster and K. Gawrisch. Light scattering characterization of extruded lipid vesicles. *Eur. Biophys. J.* 28:187-199, 1999.

[59] B.J. Frisken, C. Asman and P.J. Patty. Studies of vesicle extrusion. *Langmuir* 16:928-933, 2000.

[60] H.J. Gruber and H. Schindler. External surface and lamellarity of lipid vesicles: a practice-oriented set of assay methods. *Biochim. Biophys. Acta* 1189:212-224, 1994.

[61] J.C. McIntyre and R.G. Sleight. Fluorescence assay for phospholipid membrane asymmetry. *Biochemistry* 30:11819-11827, 1991.

[62] M. Vogel, C. Munster, W. Fenzl, and T. Salditt. Thermal unbinding of highly oriented phospholipid membranes. *Phys. Rev. Lett.* 84:390-393, 2000.

[63] L. Ingebrigtsen and L. Brandl. Determination of the size distribution of liposomes by SEC fractionation and PCS analysis and enzymatic assay of lipid content. *AAPS. Pharm. Sci. Tech.* 3:1-7, 2002.

[64] J. Israelachvili. *Intermolecular and Surface Forces.* Academic Press, San Diego, 1992.

[65] C. Tanford. *The Hydrophobic Effect.* 2nd. edn. Wiley, New York, 1980.

[66] D. Boal. *Mechanics of the Cell.* Cambridge University Press, Cambridge, 2002.

[67] . M. Wortis and E. Evans. Membrane self assembly : Mechanical properties and vesicle shapes. *Physics in Canada* 5:281-288, 1997.

[68] D. Needham, T.J. McIntosh and E. Evans. Thermomechanical and transition properties of dimyristoylphosphatidylcholine/cholesterol bilayer. *Biochemistry* 27:4668-4673, 1988.

[69] H.P. Duwe, J. Kaes, and E. Sackmann. Bending elastic moduli of lipid bilayers : modulation of solutes. *J. Phys. Fr.* 51:945-962, 1990.

[70] P. Meleard, C. Gerbeaud, T. Pott, L. Fernandez-Puente, I. Bivas, M.D. Mitov, J. Dufourcq, J. Bothorel. Bending elasticities of model membranes : influence of temperature and sterol content. *Biophys. J.* 72:2616-2629, 1997.

[71] M.R. Vist and J.H. Davis. Phase equilibria of cholesterol/dipalmitoylphosphatidylcholine mixtures : ^{2}H nuclear magnetic resonance and differential scanning calorymetry. *Biochemistry* 29:451-464, 1990.

[72] F.M. Linseisen, J.L. Thewalt, M. Bloom and T. M. Bayerl. H-2-NMR and DSC study of SEPC-Cholesterol mixtures *Chem. Phys. Lipids* 65:141-149, 1993.

[73] J.L. Thewalt and M. Bloom. Phosphatidylcholine:cholesterol phase diagram. *Biophys. J.* 63:1176-1181, 1992.

[74] E. Endress, S. Bayerl, K. Prechtel, C. Maier, R. Merkel and T.M. Bayerl. The effect of cholesterol, lanosterol and ergosterol on lecithin bilayer mechanical properties at molecular and microscopic dimensions : A solid-state NMR and micropipet study. *Langmuir* 18:3293-3299, 2002.

[75] E. Endress, H. Heller, H. Casalta, M.F. Brown, and T.M. Bayerl. Anisotropic motion and molecular dynamics of cholesterol, lansoterol and ergosterol in lecithin bilayers studied by quasi-elastic neutron scattering. *Biochemistry* 41:13078-13086, 2002.

[76] G.V. Martinez, E.M. Dykstra, S. Lope-Piedrafita, and M.F. Brown. Lanosterol and cholesterol-induced variations in bilayer elasticity probed by ^{2}H NMR relaxation. *Langmuir* 20:1043-1046, 2004.

[77] J. Henriksen, A.C. Rowat and J.H. Ipsen. Vesicle fluctuation analysis on the effect of sterols on membrane bending rigidity. *Eur. Biophys. J.* 33:732-741, 2004.

[78] Ya-Wei Hsueh, K. Gilbert, C. Trandum, M. Zuckermann, and J. Thewalt. The effect of ergosterol on dipalmitoylphosphatidylcholine bilayers : A deuterium NMR and calorimetric study. *Biophys. J.* 88:1799-1808, 2005.

[79] K.J. Tierney, D.E. Block and M.L. Longo. Elasticity and phase behavior of DPPC membrane modulated by cholesterol, ergosterol and ethanol. *Biophys. J.* 89:2481-2493, 2005.

[80] J. Henriksen, A.C. Rowat, E. Brief, YW Hsueh, J.L. Thewalt, M.J. Zuckermann and J.H. Ipsen. Universal behavior of membranes with sterols. *Biophys. J.* 90:1639-1649, 2006.

[81] L.D. Landau and E. Lifshitz, *Fluid Mechanics* 2nd Ed., Pergamon Press, Oxford, 1987.

[82] H. Schindler and J. Seelig. Deuterium order parameters in relation to thermodynamic properties of phospholipid bilayers. A statitistical mechanical interpretation. *Biochemistry* 14:2283-2287, 1975.

[83] J.D. Litster. Stability of lipid bilayers and red blood cell membranes. *Phys. Lett.* 53A:193-194, 1975.

[84] R. Sleight and C. Kent. Regulation of phosphatidylcholine biosynthesis in mammalian cells. II. Effects of phospholipase C treatment on the activity and subcellular distribution of CTP:phosphocholine cytidylyltransferase in Chinese hamster ovary and LM cell lines. *J. Biol. Chem.* 258:831-835, 1983.

[85] H. Tronchere, M. Record, F. Terce, and H. Chap. Phosphatidylcholine cycle and regulation of phosphatidylcholine biosynthesis by enzyme translocation. *Biochim. Biophys. Acta.* 1212:137-151, 1994.

[86] H. Tronchere, V. Planat, M. Record, F. Terce, G. Ribbes, and H. Chap. Phosphatidylcholine turnover in activated human neutrophils-agonist-induced cytidylyltransferase translocation is subsequent to phospholipase-D activation. *J. Biol. Chem.* 270:13138-13146, 1995.

[87] Y. Wang, T.D. Sweitzer, P.A. Weinhold, and C. Kent. Nuclear localization of soluble CTP:Phosphocholine Cytidylyltransferase. *J. Biol. Chem.* 268:5899-5904, 1993.

[88] I.C. Northwood, A.H.Y. Tong, B. Crawford, A.E. Drobnies, and R.B. Cornell. Shuttling of CTP:Phosphocholine Cytidylyltransferase between the nucleus and endoplasmic reticulum accompanies the wave of phosphatidylcholine synthesis during the G_0 and G_1 transition. *J. Biol. Chem.* 274:26240-26248, 1999.

[89] Y. Wang, T.D. Sweitzer, P.A. Weinhold and C. Kent. Nuclear localization of soluble CTP:phosphocholine cytidylyltransferase. *J. Biol. Chem.* 268:5899-5904, 1993.

[90] C.H. weber, Y.S. Park, S. Sanker, K. Kent, and M. Ludwig. A prototypical cytidylyltransferase : CTP:glycerol-3-phosphate cytidylyltransferase from *Bacillus subtilis. Structure* 7:1113-1124, 1999.

[91] M. Xie, J.L. Smith, Z. Ding, D. Zhang and R.B. Cornell. Membrane binding modulates the quaternary structure of CTP:phosphocholine cytidylyltransferase. *J. Biol. Chem.* 279:28817-28825, 2004.

[92] J.E. Johnson and R.B. Cornell. Membrane binding amphipathic α helical peptide derived from CTP:phosphocholine cytidylyltransferase. *Biochemistry* 33:4327-4335, 1994.

[93] J.I.S. MacDonald and C. Kent. Identification of phosphorylation sites in rat liver CTP:phosphocholine cytidylyltransferase. *J. Biol. Chem.* 269:10529-10537, 1994.

[94] R.B. Cornell and D.E. Vance. Binding of CTP: phosphocholine cytidylyltransferase to large unilamellar vesicles. *Biochim. Biophys. Acta* 919:37-48, 1987.

[95] S.G. Taneva, P.J. Patty, B.J. Frisken and R.B. Cornell. CTP:Phosphocholine Cytidylyltransferase binds anionic Phospholipid vesicles in a cross-bridging mode. *Biochemistry* 44:9382-9393, 2005.

[96] J.A. Friesen, H.A. Campbell and C. Kent. Enzymatic and cellular characterization of a catalytic fragment of CTP:phosphocholine cytidylyltransferase α. *J. Biol. Chem.* 19:133849-13389, 1999.

[97] M.D. Houslay, K.K. Stanley. *Dynamics of Biological Membranes : Influence of Synthesis, Structure and Function.* Willey, New York, 1982.

[98] R.W. Evans, M.A. Williams, and J. Tinoco. Surface area of 1-palmitoyl phosphatidylcholines and their interactions with cholesterol. *Biochem. J* 245:455-462, 1987.

[99] T.H. Ha, D.K. Kim, M.-U. Choi, and K. Kim. Influence of poly(ethylenimine) on the monolayer of oleic acid at the air water interface. *J. Colloid Interface Sci.* 226:98-104, 2000.

[100] G.R. Barlett. Phosphorous assay in column chromatography. *J. Biol. Chem.* 234:466-468, 1959.

[101] M.B.A. ter Beest and D. Hoekstra. Interaction of myelin basic protein with artificial membranes. Parameters governing binding, aggregation and dissociation. *Eur. J. Biochem.* 211:689-696, 1993.

[102] O. Stachowiak, M. Dolder and T. Wallimann. Membrane-binding and lipid vesicle cross-linking kinetics of the mitocondrial creatin kinase octamer. *Biochemistry* 35:15522-15528, 1996.

[103] M.A. Kaetzel, Y.D. Mo, T.R. Mealy, B. Campos, W. Bergsma-Schutter, A. Brisson, J.R. Dedman, and B.A. Seaton. Phosphorylation mutants elucidate the mechanism of Annexin IV-mediated membrane aggregation. *Biochemistry* 40:4192-4199, 2001.

[104] O.A. Bizzozero, and T.A. Howard. Myelin proteolipid protein-induced aggregation of lipid vesicles : efficacy of the various molecular species. *Neurochem. Res.* 27:1269-1277, 2002.

[105] S. Bernad, S. Oellerich, T. Soulimane, S. Noinville, M.H. Baron, M. Paternostre, and S. Lecomte. Interaction of horse heart and thermus thermophilus type cytochromes with phospholipid vesicles and hydrophobic surfaces. *Biophys. J.* 86:3863-3872, 2004.

[106] C. D'Antuono, M. del Carmen-Fernandez Tome, N. Sterin-Speziale and D.L. Bernik. Lipid-protein interactions in rat renal subcellular membranes: A biophysical and biochemical study. *Arch. Biochem. Biophys.* 382:39-47, 2000.

[107] T. Neitcheva and D. Peeva. Phospholipid composition, phospholipase A2 and spingomyelinase activities in rat liver nuclear membrane and matrix. *Int. J. Biochem. Cell Biol.* 327:995-1001, 1995.

[108] H. Ohshima, in : H. Ohshima and K. Furusawa (Eds). *Electrical Phenomena at Interface,* 2nd ed., Marcel Dekker, New York, 1998.

[109] S. Ohki and H. Oshima. Interaction and aggregation of lipid vesicles (DLVO theory versus modified DLVO theory). *Colloids and Surfaces B.* 14:27-45, 1999.

[110] K. Ohsawa, H. Ohshima and S. Ohki. Surface-potential and surface-charge density of the cerebral-cortex synaptic vesicle and stability of vesicle suspension. *Biochim. Biophys. Acta* 648:206-214, 1981.

[111] M. Eisenberg, T. Gresalfi, T. Riccio and S. McLauchlin. Adsorption of mono-valent cations to bilayer membranes containing negative phospholipids. *Biochemistry* 18:5213-5223, 1979.

[112] J.S. Dunne, R.B. Cornell, J.E. Johnson, N.R. Glover, and A.S. Tracey. Structure of the membrane binding domain of CTP:Phosphocholine Cytidylyltransferase. *Biochemistry* 35:11975-11984, 1996.